Physics Department, Neuchâtel University

Time Projection Chambers and detection of neutrinos

Thesis by

Patrick Jeanneret

Physicist with a Diploma of Lausanne University

presented at
the Faculty of Sciences of Neuchâtel University
for the Degree of Doctor ès Sciences

the 28 September 2001, in presence of a jury composed by
Prof. Dr. J.-L. Vuilleumier, thesis advisor, Neuchâtel
Dr. J. Busto, Neuchâtel
PD Dr. D. Twerenbold, Neuchâtel
Prof. Dr. V. Zacek, Montréal
Prof. Dr. I. Giomataris, Paris

IMPRIMATUR POUR LA THESE

Time projection chambers and detection of neutrinos

de M. Patrick Jeanneret

UNIVERSITE DE NEUCHATEL

FACULTE DES SCIENCES

La Faculté des sciences de l'Université de Neuchâtel sur le rapport des membres du jury,

MM. J.-L. Vuilleumier (directeur de thèse),
J. Busto, D. Twerenbold, V. Zacek (Montréal) et
I. Giomataris (Paris)

autorise l'impression de la présente thèse.

Neuchâtel, le 1er février 2002

Le doyen:

F. Zwahlen

A ANABELA, A LOÏCK
ET
A MES PARENTS

Preface

I am very grateful to my chief Jean-Luc Vuilleumier, for his constant availability, for his advices, for his humanity, for his "competence" and his friendship. I am very grateful to José Busto, for his very important help during all my work, specifically for his help and advices for the installations and tests described in Chapter 3, for all his advices and his friendship. I am very grateful to Antoine Geiser, who worked with me for his licence and returned to work sometimes with me, whose help concerning installations and tests described in Chapter 3 was very important and with whom I have enjoyed a lot working. I am very grateful to Giovanni Gervasio, for his important help to start the work concerning installations and tests described in Chapter 3, for his advices in other domains and for his friendship, to Vérène Chazal for her positivity, for her constant help and advices, and for her friendship, to Jean-Michel Vuilleumier, for his constant help in various domains, his advices and his friendship, to Roland Luesher, for having worked with me to realize the acquisition program used for Gotthard experiment on $\beta\beta$ decay and "mini" TPC, see Chapter 3, for his advices and for his friendship, to Alan Païc, for his help and advices in the beginning of my work and for his friendship, to Jacques Farine, for his advices and his friendship, to Guy Jonkmans, for having suggested me to utilize μ for calibrations and helped me to start in that work, and for his friendship, to Gordana Grgic, for her friendship, to Leila Ounalli, for her friendship, to Zornitza Daraktchieva, for her friendship, to the rest of MUNU collaboration, for their help and friendship, to all "external" people who have contributed to the realization of this work, like Rui de Oliveira, at CERN, Ioannis Giomataris, at Saclay, Herbert Keppner, at Engineer School of Le Locle, to all people of the technical support of the Physics Department of Neuchâtel University, for their important help and their friendship and to many other people of the Physics Department of Neuchâtel University, for their help or friendship. I am very grateful to my wife Anabela and my son Loïck Willy for their affection, and also for their comprehension concerning my lack of availability. I am very grateful to my parents Marlyse and Willy Jeanneret, whom I consider to be the best parents that it is possible to have, for all they have done and given to me. My father is deceased; I am always thinking strongly of him and wish to dedicate this work particularly to him. I am also very grateful to the rest of my family and to all my Friends.

Neuchâtel, September 2001 Patrick Jeanneret

Contents

List of Figures

Abstract

In MUNU experiment the (anti)neutrino magnetic moment is measured via the study of $\bar{\nu}_e e^-$ scattering inside a Time Projection Chamber (TPC). The low scattering cross section of the reaction between antineutrinos and electrons, and the low energy of the latter imply strength constraints on the detector. We had then to face a lot of experimental problems to make the observation of antineutrinos possible. Detector features, like TPC tracking features, were very helpful to check the detector, identify or resolve its problems. Tracking is fundamental for background rejection. It is also "essential" to perform calibrations and "reconstructive" spectroscopy of "particles" emitted by a "source". Some "ways" of utilizing the TPC were discovered during experiment. "Preliminary" results concerning neutrinos magnetic moment will be shortly presented. The detector is still running, and more "interesting" results should be obtained. We are also expecting for the next reactor "OFF" period to measure "precisely" background. Future neutrinos experiments, like solar neutrinos detection, can require still larger TPCs. Large detection planes adapted for the detection of neutrinos are then required. One part of this work concerns MUNU experiment, and thus the detection of (anti)neutrinos with a TPC, and another part corresponds to "preliminary" tests or developments on TPCs' detection planes (concerning GEM, LEM, Micromegas "with grid" and Micromegas "with cloth") for future neutrinos experiment, and, eventually, for other applications.

Chapter 1

Introduction

The predictions concerning neutrino properties, like mass, depend of the model used to describe the latter, so it is very important to be able to determine these properties experimentally. In the standard model, we do not neet to give a mass to the neutrino, but it is necessary in "more unifying" models, like GUT or superstrings.
It seems that there is no reason to make the neutrino mass matrix diagonal in the base $\begin{pmatrix} \nu_e \\ \nu_\mu \\ \nu_\tau \end{pmatrix}$, so each flavor state must be a superposition of the different mass states. As the latter do not have the same energy, there must be an oscillation of neutrino's flavor. Vacuum and matter solutions are different. There are various possibilities for the matter solutions of solar neutrinos, such as small mixing angle (SMA), low mixing angle (LOW) and large mixing angle (LMA).
Observation of solar ν_e flux by different experiment like GALLEX [1], SAGE [2] or Super-Kamiokande [3] have shown the disappearance of a part of the expected flux, which is a very important information on the ν behaviour. The observation of the reduction of the ν_μ atmospheric flux is an evidence for flavor oscillation, and thus for a massive neutrino. Recent observations of solar ν by Super-Kamiokande have confirmed the low flux seen by GALLEX and SAGE. SNO [4, 5], looking at solar ^8B ν flux, has recently verified the reduction of solar ν flux. This experiment has also shown the presence of a non electronic component in the solar ν flux, which implies ν oscillations, because only ν_e are emitted by the sun, and has given upper and lower limits to the sum of the 3 flavour ν masses.
Oscillation is not the only way to explain the reduction of the expected flux. The helicity flip of the neutrino due to the interaction of the neutrino magnetic moment μ_ν with the solar magnetic field is another possible explanation. However, the "existence" of μ_ν is only possible in case of massive neutrinos. To be compatible with experimental data, the upper limit for μ_ν has to be of the order of μ_B^{-10} to μ_B^{-11}. These reasons have lead to the MUNU [6, 7, 8, 9, 10] experiment.

The goal of the MUNU experiment is the determination of μ_ν, with a sensitivity of a few μ_b^{-11}. MUNU is a low background detector constituting of a gas Time Projection Chamber (TPC), in which we observe $\bar{\nu}_e e^-$ scattering, surrounded by an active shielding (anti-Compton). The source of $\bar{\nu}_e$ is the nuclear reactor of Bugey, in France. The detector is situated at about 18 m of the reactor. The direction of the $\bar{\nu}$ beam is well defined and the energy spectra well-known [11, 12, 13]. The gas chosen to fill the TPC is CF4, which presents a high e^- density and contains no hydrogen, so $\bar{\nu}$ scattering with e^- is more probable than $\bar{\nu}$ scattering with protons. When a charged particle is crossing the gas of the TPC, it ionizes the latter. A track results then from this ionization. The latter is more intense at the end of the track, so track's end can be identified by a blob. With the TPC detection system, we can determine the trajectory of the charged particle in three dimensions, the scattering angle and the energy left by the e^- along its track. The latter is proportional to the number of ionizations and its integration corresponds to the total kinetic energy of the e^- if the latter is fully contained inside of the TPC. With anti-Compton and tracking it is possible to reject many events which cannot correspond to $\bar{\nu}_e e^-$ scattering.

1.1 $\bar{\nu}_e e^-$ tracking and μ_ν determination

The observed events are possible and "acceptable" $\bar{\nu}_e e^-$ events if they are fully contained in the gas of the TPC with a start and an end clearly identifiable and if there is no energy deposition inside of the anti-Compton during the possible time of event occurrence in the TPC. The two most important informations obtained for such events are (see figure 1.1):

- θ_e, scattering angle of the recoil electron
- T_e, initial kinetic energy of the recoil electron, i.e. $T_e = E_e$ - $m_e c^2$

From the conservation of the total energy momentum vector p^μ and the invariance of its norm, with $p^\mu p_\mu = (mc)^2$, we find, taking $m_\nu = 0$

$$\cos\theta_e = \left(1 + \frac{m_e}{E_{\bar{\nu}}}\right)\left(\frac{T_e}{T_e + 2m_e}\right)^{\frac{1}{2}} \tag{1.1}$$

The kinetic energy of the recoil electron T_e is maximum when the scattering angle θ_e is equal to zero. We have then

$$T_{e,\theta=0} = \frac{2E_{\bar{\nu}}^2}{2E_{\bar{\nu}} + m_e} \tag{1.2}$$

In first order, $\bar{\nu}_e e^-$ scattering is described by an interference between neutral current, i.e. coupling with Z boson (first term of figure 1.2) and charged currents, i.e coupling with W bosons (second term of figure 1.2). The neutrino is not charged, so the coupling with photons is only possible with virtual loops containing charged leptons or charged bosons (third term of figure 1.2).

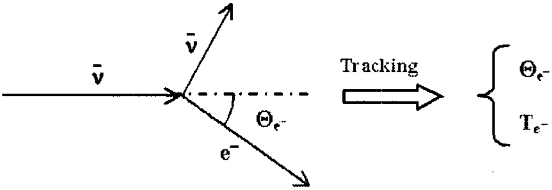

Figure 1.1: Tracking of the e^- for a $\bar{\nu}_e e^-$ event

The interference of all possible virtual loops (which contain always pairs of opposite charge) corresponds to a distribution of charge around the neutrino. This charge distribution can be described with form factors [11].

The scattering amplitude M can thus be expressed by the sum of a scattering amplitude "containing" coupling with pure weak currents (i.e. the sum of the two first Feynmann diagrams of figure 1.2, at the first order) with a scattering amplitude containing coupling with electromagnetic current. The latter, in a general case, can be represented by

$$\begin{aligned} &\langle \nu(p_f,\lambda_f)|J^{\gamma}_{\mu}(0)|\nu(p_i,\lambda_i)\rangle = \\ &\quad \bar{u}(p_f,\lambda_f)\left[\left(\mathrm{F}(q^2)+\gamma_5\mathrm{G}(q^2)\right)\gamma^{\nu}\left(q^2 g_{\nu\mu}-q_{\nu}q_{\mu}\right)+\left(\mathrm{M}(q^2)+i\mathrm{E}(q^2)\gamma_5\right)i\sigma_{\mu\nu}q^{\nu}\right]u(p_i,\lambda_i) \end{aligned} \tag{1.3}$$

This equation follows from Lorentz covariance and electromagnetic current conservation.

p_i and p_f represent the energy momentum of initial and final neutrinos, and $q \equiv p_f - p_i$. $\lambda = \pm 1$ stands for the eigenvalues of the helicity operator $\vec{\sigma}\frac{\vec{p}}{|\vec{p}|}$.

F, G, M, E are form factors.

F and G are related to the charge radius. M and E correspond to electric and magnetic dipole moments. $\sigma_{\mu\nu}q^{\nu}$ induces a flip of neutrino's helicity. When the mass of the neutrino is null, there is no coupling between left and right fields, so M and E are null in such a case. M and E depend of the mass of the neutrino and of its type. For Majorana

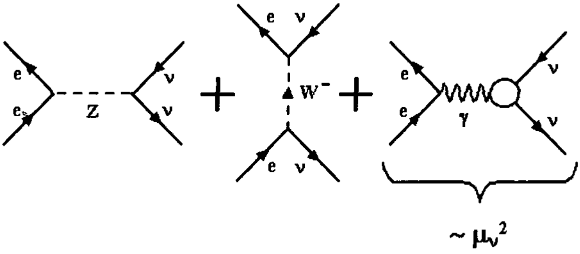

Figure 1.2: Scattering

neutrinos (i.e. massive neutrinos which are their own antiparticle), diagonal amplitude of M and E vanish, but this is not the case for massive Dirac neutrinos. Both Dirac and Majorana neutrinos can have off-diagonal amplitudes with nonvanishing M and E form factors. The term containing F and G gives a coherent contribution to the scattering amplitude obtained for coupling with pure weak currents, and the term containing M and E give a non-coherent contribution. The latter is related to the magnetic moment of the neutrino. From the amplitude of $\bar{\nu}_e e^-$ scattering and the conservation of total energy momentum p, we can obtain the following relation for the differential cross-section $\frac{d\sigma}{dT}$:

$$\begin{aligned}\frac{d\sigma}{dT} = & \\ & \frac{G_F^2 m_e}{2\pi}\left[(g_V + x + g_A)^2 + (g_V + x - g_A)^2\left(1 - \frac{T}{E_\nu}\right)^2 + (g_A^2 - (g_V + x)^2)\frac{m_e T}{E_\nu^2}\right] \\ & + \frac{\pi\alpha^2\mu_\nu^2}{m_e^2}\frac{1 - T/E_\nu}{T}\end{aligned} \tag{1.4}$$

G_F is the Fermi constant.
x is related to the square charge radius $< r^2 >$ of the neutrino:

$$x = \frac{2M_W^2}{3} < r^2 > sin^2\theta_W \text{ for } \nu_e,\ x \rightarrow -x \text{ for } \bar{\nu}_e. \tag{1.5}$$

M_W is the W mass and θ_W the Weinberg angle.
g_V and g_A are given by the following relations:

$$g_V = 2sin^2\theta_W + \frac{1}{2},\quad g_A = \left\{\begin{array}{rl} \frac{1}{2} & \text{for } \nu_e \\ -\frac{1}{2} & \text{for } \bar{\nu}_e \end{array}\right.$$

Equation 1.4 can be written as:

$$\frac{d\sigma}{dT} = \left(\frac{d\sigma}{dT}\right)_x + \left(\frac{d\sigma}{dT}\right)_{\mu_\nu} \tag{1.6}$$

We see that $\left(\frac{d\sigma}{dT}\right)_{\mu_\nu}$ is proportional to μ_ν^2.
When $T = T_{e,\theta=0}$ (see equation 1.2), i.e when the scattering angle θ_e is equal to zero, it is possible to show that $\left(\frac{d\sigma}{dT}\right)_x$ is given by:

$$\left(\frac{d\sigma}{dT}\right)_x = \frac{G_F^2 m_e}{2\pi}\left[(g_V - g_A) + (g_V + g_A)\frac{m_e}{2E_\nu + m_e}\right]^2 \tag{1.7}$$

If $\left(\frac{d\sigma}{dT}\right)_x = 0$, then

$$E_\nu = m_e \frac{g_A}{g_V - g_A} \tag{1.8}$$

We have then $E_\nu = 553$ keV, and from kinematics, we find $T_e = 350$ keV.

This implies that the sensitivity to the neutrino magnetic moment is maximal for small scattering angles, when the energy of the recoil electron is of about 350 keV.

With MUNU's TPC we can see recoil electrons between about 100 keV and 5 MeV. The reactor produces $\bar{\nu}$ from about 0 to 10 MeV. These $\bar{\nu}$ are mainly produced by β decays of fission products. The β decays resulting from the activation of ^{238}U by neutron ($^{238}U + n = ^{239}U$) are negligible. The reactor spectra $\frac{dN(E_\nu)}{dE_\nu}$ is well-known [12, 13], and we have access to data concerning its power variations in time. We can then integrate over E_ν to obtain the mean differential cross section for recoil electrons, in function of their kinetic energy [11]:

$$\left\langle \frac{d\sigma(T_e)}{dT_e} \right\rangle = \int \frac{dN(E_\nu)}{dE_\nu}\frac{d\sigma(E_\nu, T_e)}{dT_e} dE_\nu \tag{1.9}$$

$\left\langle \frac{d\sigma(T_e)}{dT_e} \right\rangle$ depends on the electromagnetic contribution to $\frac{d\sigma(E_\nu,T_e)}{dT_e}$, specifically on the non-coherent contribution related to μ_ν. In figure 1.3 we see the corresponding spectra obtained with $\mu_\nu = 0$ and the spectra describing the magnetic contribution with $\mu_\nu = 10^{-10}\ \mu_B$.

In MUNU we can measure the spectra of the recoil electrons and the scattering angle and determine the "type" of events. These features correspond to more information and more reliability than a simple "count above one given threshold". The latter can give wrong results in case of unexpected noise.

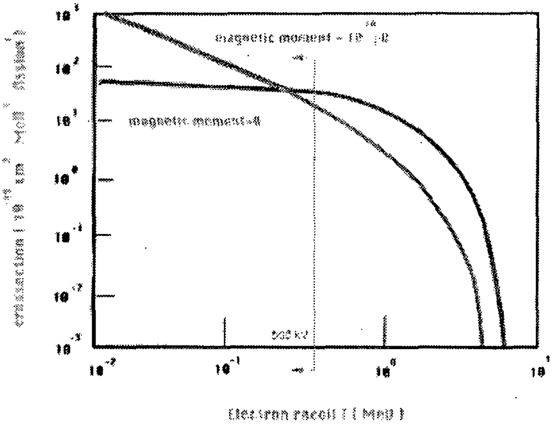

Figure 1.3: T_e distribution spectra of recoil e$^-$, with $\mu_\nu = 0$, and electromagnetic contribution, with $\mu_\nu = 10^{-10}$ μ_B, expected inside detector and obtained by integration over the spectra of $\bar{\nu}$ emitted by the reactor.

Some experimental limits on effective μ_ν are given below. From $\bar{\nu}_e e^-$ scattering observation in reactor experiments, the following limits were obtained:

- $\mu_\nu = $ (2-4) 10^{-10} μ_B was the value found by Vogel [11], after having analyzed the data of the first reactor experiment, realized at Savannah River by Reines et al. [14]. The other reactor experiments realized after that one have given only limits, but of lower value than this first result

- $\mu_\nu \leqq$ 2.4 10^{-10} μ_B at Kurchatov

- $\mu_\nu \leqq$ 1.8 10^{-10} μ_B at Rovno [15]

The accelerator experiment done at the LAMPF [16, 17] beam dump has given the following limit:

- $\mu_\nu \leqq$ 1.8 10^{-9} μ_B for ν_μ

The observation of solar neutrinos by super-Kamiokande [18] has given also an information on $\mu_\nu$value, because $\mu_\nu \neq 0$ implies a deformation of the spectra. Only a reduction of the flux has been observed, without deformation, corresponding to the following limit, assuming that the ν do not oscillate:

- $\mu_\nu^{sol} \leqq$ 1.5 10^{-10} μ_B

Some astrophysical considerations give lower limits but the latter are largely more model dependent:

- $\mu_\nu \leqq 2\ 10^{-11}\ \mu_B$ for Dirac ν, from the observation of Helium abundance [19]
- $\mu_\nu \leqq (1\text{-}20)\ 10^{-13}\ \mu_B$ for Dirac ν, from the ν burst of supernova SN1987A [20]
- $\mu_\nu \leqq (10^{-11} - 10^{-13})\ \mu_B$ from stellar cooling [21]

1.2 $\bar{\nu}_e$ detection in a TPC and goals

The interest of MUNU concerns not only the measurement of the neutrino magnetic moment, but also the realization and the utilization of a sub MeV particles detector, at a low counting rate.

"Low" energy (less than 2 MeV) and "Low" counting rate (about 8 $\bar{\nu}_e e^-$ events are expected each days) imply strong constraints on the detector realization and functioning (like active shielding and very low radioactive materials). A part of the knowledge is only acquired during and after building. The association of the TPC and of the active shielding give very important information concerning the detector (like the source of possible contaminations) and physical events (like the scattering angle for recoil electrons). Some types of information result of the detector conception, but others were discovered during the experiment.

The first part of this work describes some of the knowledge (on information given by the detector, and on its current utilization), that have been acquired when "running" the detector and some of the developments that have been realized. "Preliminary" physical results will also be shortly presented.

TPCs present very interesting features, and we can think about future experiments on neutrino detection, which would benefit from the knowledge acquired with the MUNU experiment [6, 7, 8, 9, 10] and also with the Gotthard Xenon experiment [22, 23, 24, 25]. More specifically, we are thinking of the spectroscopy of low energy solar neutrinos, extending down to the pp-neutrinos [26] (superMUNU) and of the search for double beta decay in ^{136}Xe [27, 28]. In both case, larger TPCs, of order 50 m^3, seem to be the right tool. Standard technologies based on charge multiplication around thin wires can hardly be used. We are therefore searching alternatives. I have then fixed myself two goals. The first was to find or develop an amplification system satisfying criteria for neutrino detection, in "superMUNU conditions", and the second was to get some comprehension about their functioning in various conditions.

I hope that some of the results presented in this work will be useful for future applications.

Chapter 2

MUNU experiment

2.1 Presentation of the experiment

The detector is situated in one of the 4 nuclear reactors of Bugey in France, at 18 meters of the reactor core, source of $\bar{\nu}_e$ (see figure 2.1).

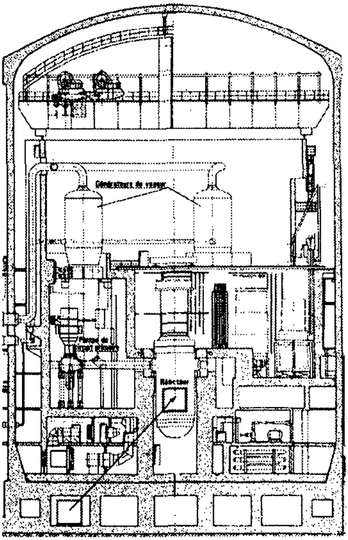

Figure 2.1: Detector position inside of the nuclear reactor. The arrow is oriented from the detector to the reactor core, source of $\bar{\nu}_e$, so the direction of the incident $\bar{\nu}_e$ inside of the TPC is opposite to the arrow. Concrete prevents β, γ and n coming out of the reactor from reaching the detector. The detector is at $8m$ underground, so it protected against an appreciable fraction of cosmic μ (the "residual" μ flux measured is of 32 $\mathrm{m}^{-2}\mathrm{s}^{-1}$).

The "heart" of the detector is an acrylic 1 m^3 TPC (figure 2.2 and 2.6) filled with CF_4, which serves as e$^-$ target and detector. Detection planes and cathode are inside it. To reduce activity, all material constituting the TPC are made with the following criteria:

- low activity materials (the activity is tested by γ spectroscopy in the germanium detector of Vue des Alpes, near Neuchâtel)
- as little matter as possible
- cleanest conditions possible (for realization, transport and installation)

From the digitalization and treatment of the electronic signals produced by detection planes we can do tracking and energy measurement.
The TPC is immersed in 10 m^3 of liquid scintillator, which is contained by a vessel (figure 2.2 and 2.6). The latter is equipped with 2×24 photomultipliers (figure 2.2 and 2.6), which detects the light produced by the scintillator liquid when energy is left inside the latter by a charged particle. The vessel surrounding the TPC acts thus as an active shielding for Compton and cosmic events. The "detector" corresponds to the association of the active shielding ("anti-Compton") with the TPC. A low activity passive shielding (figure 2.2 and 2.6) composed of 8 cm thick borated polyethylene (protection against neutrons) and of 15 cm thick lead (protection against activity coming from the room containing the detector) is surrounding the detector.

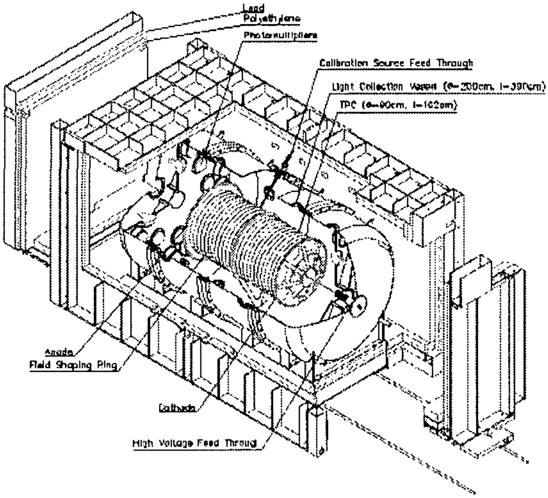

Figure 2.2: 3D view of MUNU detector, with the TPC contained inside of the anti-Compton, and of the passive shielding surrounding the latter

2.1.1 TPC

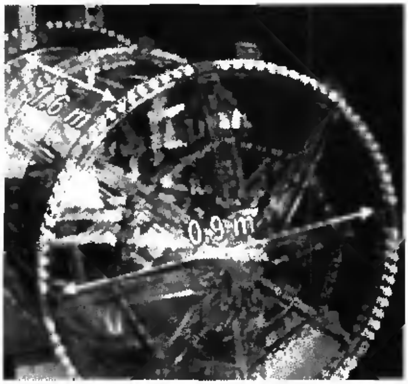

Figure 2.3: Acrylic body of the TPC

The body of the TPC is an acrylic cylinder with an inner diameter of 90 cm, an inner length of 162 cm and a thickness of 5 mm. Acrylic was chosen for its low activity. It is as thin as possible to:

- minimize the radioactivity
- minimize the inactive volume, in particular to avoid the absorbtion in the acrylic of γ coming from the gas, before they can be detected by the anti-Compton

The TPC is surrounded by field shaping rings connected with resistances. The field shaping rings and the resistances are situated at the exterior of the TPC, so that their activity can be detected by the anti-Compton.

CF_4 was selected to fill the TPC, principally for the following reasons:

- high e^- density $\Rightarrow$ appreciable total $\bar{\nu}_e e^-$ scattering cross section
- low Z $\Rightarrow$
  - reduce e^- multiple scattering
  - Only few γ of low energy loose all their energy in the gas, so most of them are detected by anti-Compton.
- no free protons $\Rightarrow$ no reaction $\bar{\nu}_e + p \rightarrow e^+ + n$.

A cathode made from a high purity electrolytic copper foil is mounted on one lid (see figure 2.5). Detection system is mounted on the other side. It consists, from inside to outside, of a grid, an anode plane, at 8.5 mm from grid, and an XY plane, at 3 mm from anode (see figure 2.4, 2.5 and 2.6). Grid wires diameter is of 100 μm . The distance between two grid wires is of 4.95 mm. Anode plane is made of 20 μm diameter anode wires, separated by 100 μm diameter potential wires. The distance between two anode wires (or two potential wires) is also 4.95 mm. X strips are situated on one side of a 125 μm PET foil, Y strips on the other side. There are 256 $\times$ 256 strips, spaced by 3.5 mm. With a TPC we can observe the energy left by an electron having ionized the gas, which is proportional to the number of ionizations, and the 3 dimensional track of that electron. The principle of observation is the same for all TPCs (see figure 2.5 and 2.6). A drift field due to a difference of potential between a cathode and a detection plane (constituted in our case by anode wires and XY plane) forces the electrons ionized along the track to drift to the detection plane. A very high field present near detection plane (in our case around anode wire) causes an electrical avalanche for each electron having drifted to the anode (the mean number of electrons produced after avalanche multiplication for one "initial" electron is called the gain). The electrical charge produced by this way is proportional to the initial number of electrons (i.e the number of ionizations) and induces an electrical signal on detection plane (whose integration is proportional to the electrical charge and thus to the initial kinetic energy T_e of the electron having ionized the gas). The signal induced on the XY plane (in our case the XY plane is situated after anode, i.e. amplification plane but there exists other type of detection planes where the XY plane and the amplification plane are not separated) gives a projection of the track, and with the time information corresponding to the order of arrival of the drifting electrons, we can reconstruct the third dimension (Z). TPC acts as its own trigger and acquisition threshold is fixed at 300 keV.

Figure 2.4: MUNU's detection plane, with grid, anode plane, XY plane, and, on left, the readout connectors crossing the acrylic lid

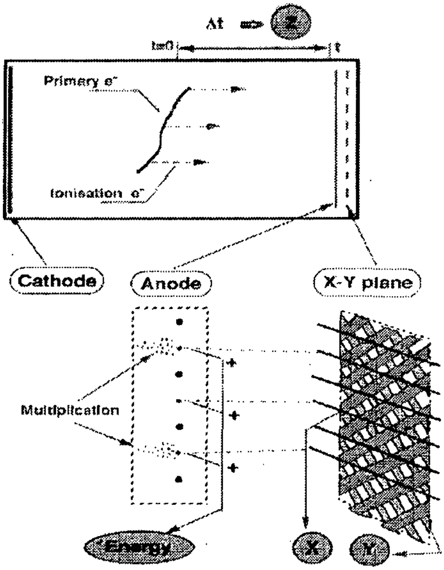

Figure 2.5: How the TPC works

The grid separates the drift gap from the amplification gap (where the avalanches take place), and focuses the drifting e^- on the anode. The field shaping rings are necessary to get an homogenous field configuration (they won't be necessary for infinite detection planes), to avoid tracks deformation and inhomogeneous gain. The potential wires impose a symmetrical field configuration around the anode wires, so that no force acts on them.

The value of pressure acts on various parameters related to $\bar{\nu}_e e^-$ observation. The main advantages and disadvantages of a "high" pressure (opposite to that of a "low" pressure) are the following:

- "high" pressure ⇔ "high" number of e^- in the TPC ⇔ "high" event rate (for the total detector activity predicted by simulation, a pressure of at least 2.5 bar is necessary to get a sufficient event rate)
- "high" pressure ⇔ "short" tracks ⇒
  - "high" number of tracks fully contained in the TPC (advantage)
  - "low" resolution on the 3d topology of the track (disadvantage)
- "high" pressure ⇔ "high" multiple scattering and "high" lateral drift diffusion ⇒ "low" resolution on the 3d topology of the track (thus low angular resolution)

Drift time and a drift velocity are optimized in order to get the best spatial resolution. We are now operating with a drift field of 73 $\mathrm{Vcm}^{-1}\mathrm{bar}^{-1}$. The attenuation length in CF_4 is of about 10 to 20 m at 3 bar, which is good in comparison with the TPC length. Reduced attachment coefficient $\frac{\eta}{N}(\frac{E}{N})$ (see section 2.3.1), with $E \equiv$ electrical field and $N \equiv$ number of CF_4 atoms per volume unit, is low during drift phase, but during the early phase of avalanche, the value of E is corresponding to a "high" value of $\frac{\eta}{N}(\frac{E}{N})$. In this stage, nearly 98 % of e^- are captured by CF_4 [29, 30], which implies a lost of resolution.
A simulation having taken into account statistical fluctuation $N_{ionization}{}^{\frac{1}{2}} \propto T^{\frac{1}{2}}$, reduced attachment coefficient $\frac{\eta}{N}(\frac{E}{N})$, and other parameters, has shown that resolution follows a $T_e^{0.7}$ rather than a $T_e^{\frac{1}{2}}$ law. This corresponds to a resolution of about 8 % at 640 keV, which is in good agreement with measurements (sections 2.3.1 and 2.3.2).
The gas has to be as clean as possible, for the following reasons:

- optimize drift and amplification ⇒ remove oxygen (and other impurities)
  (the presence of oxygen in CF_4, even in very small quantities, can make drift not possible; discharges threshold is also very sensitive to the presence of H_2O) ⇒
  circulation through a special filter
  (initially this filter was of type "OXYSORB", but it was discovered that it was outgassing radon, and we replace it with a filter of type "SAES", see figure 2.14)

- reduce natural activity ⇒ remove radon (and other impurities)
  (radon, i.e. ^{220}Rn, from ^{232}Th decay chain and ^{222}Rn, from ^{238}U decay chain, is one of the most important noise source in low activity experiments) ⇒
  circulation through a cold trap with active charcoal
  (radon liquefaction temperature, which is -62 °C at 1 bar, is above CF_4 liquefaction temperature, which is -130 °C at 1 bar, so we can liquefy radon and eliminate it of CF_4 by cooling the gas; the efficiency of trapping is increased by cooling through an active charcoal, which presents a very high surface for heat exchanges and radon fixation; the latter is possible without cooling)

The temperature of the cold trap is set to about -95 °C at 3 bar, near the liquefaction temperature of CF_4 at 3 bar, which is -110 °C. The active charcoal has to be regularly cleaned. This is done by pumping and heating. The cold trap can remove all CF_4 gaseous "contaminants" whose liquefaction temperature is above CF_4 liquefaction temperature, like H_2O. Unfortunately, ^{85}Kr, which emits β of 687 keV and is also a gas at ambient temperature, much more rare than ^{220}Rn and ^{222}Rn, but present in nuclear reactors, has a liquefaction temperature well below that of CF_4 (at 1 bar liquefaction temperature of ^{85}Kr is -152 °C). We don't know any filtering system that can eliminate ^{85}Kr (except distillation), so when we suspect a ^{85}Kr contamination, we change the gas. The circulation debit is of about 500 lh^{-1}. All gas system (and operations on it) can be controlled by a central system acting on electromechanical valves. Flux, pump temperature, (pump is cooled by liquid alcohol), gas temperature, gas pressure and difference of pressure between TPC and anti-Compton scintillator, which is controlled by pressurization of nitrogen on scintillator, are continuously checked by acquisition ("slow control").

2.1.2 Active shielding (anti-Compton)

The second component of the detector is the anti-Compton. It is designed to act as veto for Compton events and to detect cosmic particles, which could induce 'neutrino-like' events in TPC. Anti-Compton also turned out to have other very useful functions, such as events characterization or absolute Z determination, for different type of events.
The TPC is suspended in the anti-Compton and is immersed by its scintillator liquid (see figure 2.2, 2.6 and 2.7).

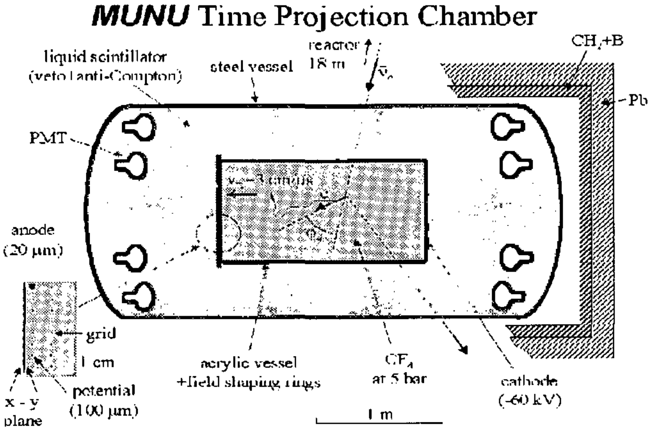

Figure 2.6: The TPC, with its detection planes, and the anti-Compton, with its PMTs

The main anti-Compton components are (see figure 2.2, 2.6, 2.7 and 2.8):

- a cylindrical low activity steel tank, painted with reflective TiO_2 to optimize scintillation light collection (see figure 2.8)
- 8 m^3 of NE235 mineral oil liquid scintillator (attenuation length of 8 m at 430 nm), filling all the space between the TPC and the steel tank
- 48 hemispherical low activity EMI 9351 photomultipliers of 20 cm diameter subdivided in 2 groups of 24, one on the anode side of the steel tank and the other on the cathode side
- an acrylic pipe crossing the anti-Compton at an axial distance of 26 cm from the center of the detector, on the anode side, in which radioactive sources can be introduced at a distance of 1 cm from TPC wall, to calibrate it and the anti-Compton

Figure 2.7: The space between the TPC and the steel tank, the acrylic tubes to sustain the TPC and the photomultipliers to detect the scintillation light

The various features of the anti-Compton are related with its ability to detect and measure in "real time" the quantity of light (which is measured in "photoelectrons"; a photon can eject, with an efficiency of about 25 % to 30 % for these PMTs, an electron at the photocathode; the latter will cause an avalanche in the dynode chain, corresponding to a signal whose amplitude is determined). The light is coming from 2 origins:

- scintillation light coming from the liquid scintillator
  $N_{photoelectrons} \propto$ energy left by the charged particle in the scintillator $\Rightarrow$
  possibility to get "energy class" information on anti-Compton events; in MUNU's acquisition there are 3 energy classes for anti-Compton events, corresponding to low anti-Compton threshold, high anti-Compton threshold and μ threshold (these thresholds are defined by a determined value of the amplitude of the sum of PMTs signal, ΣPM, which is proportional to the energy left in the scintillator, and also by a given number of PMTs "hit" in coincidence, $PM_{multiplicity}$), to avoid dark noise causing accidental starts:
    - low threshold "on" $\Leftrightarrow \Sigma PM \geq 100$ keV and $PM_{multiplicity} \geq 5$
      (simulation and measurements have shown that 100 keV left in the scintillator corresponds to about 15 to 30 photoelectrons) $\Rightarrow$

  - ∗ "veto" TPC's events, over a period of 80 μs, which is an upper estimation of the drift time corresponding to the length of the TPC ⇔ reject TPC's Compton events induced by the γ rays coming from the outside and from the inside of the TPC (this is the main function of the anti-Compton); the counting rate is 440 s^{-1} (except μ), corresponding to a dead time of 4%; the inefficiency to reject γ associated with TPC's Compton electron of more than 300 keV has been measured using the ^{54}Mn source:
    - · $3 \cdot 10^{-2}$ for γ coming from the gas (a γ is lost when it does not interact with the scintillator or is absorbed by solid TPC material)
    - · 10^{-6} for γ coming from the outside of the TPC (the probability for a γ to leave at least 100 keV in the scintillator is much higher than the probability to leave at least 300 keV in the gas)

- – high threshold "on" ⇔ $\Sigma PM \geq 300$ keV and $PM_{multiplicity} \geq 10 \Rightarrow$

  - ∗ select TPC Compton events, using a radioactive source emitting γ, to measure $\bar{\nu}_e e^-$ tracking ability
    (the kinematics for Compton scattering is the same as for $\bar{\nu}_e e^-$ scattering, because the photon mass is equal to zero and $\bar{\nu}$ mass can be considered as equal zero; γ are emitted from the radioactive source, so their spatial origin is well-defined; the difference between the times of anode event start and of scintillator event start, which corresponds to the occurrence time of the event, is equal to the time taken to drift by the tracks e^- which are nearest to anode; from this time we can get the Z absolute coordinates of the track, and thus its 3D absolute coordinates)
  - ∗ realise γ spectra in the liquid scintillator, using a radioactive source

- – μ threshold "on" ⇔ $\Sigma PM \geq 20$ MeV ⇒

  - ∗ "veto" TPC's events, on a period of 200 μs, which is greater than the drift time corresponding to the length of detector ⇒
    reject μ events and also possible indirectly correlated events; the counting rate is 270 s^{-1} for μ, corresponding to a dead time of 6%

  - ∗ selection of μ to calibrate the detector
    (it is possible to select minimum ionizing μ, whose linear ionization energy density is constant, and thus to use them for gain estimation; the estimation of gain from μ can be global and also local, see section 2.3, because the scintillator's information on μ gives, as for Compton electrons, absolute Z position, and thus absolute 3D track)

- scintillation light coming from the CF_4 contained in the TPC
  before "running" the detector, it wasn't clear wether CF_4 scintillation light would be detected by the anti-Compton, i.e "accepted" following low anti-Compton threshold criteria; the experiment has shown that the scintillation light of avalanche and the primary scintillation light of α can be detected but that e^- and minimum ionizing μ primary scintillation light is too weak (CF_4 scintillation light has a maximum of intensity at 300 nm, but acrylic transparency at this value is not very high, and almost only scintillation light's photons of more than 400 nm that can be detected, so only "intense" scintillations can be detected) $\Rightarrow$
  - avalanche detection by anti-Compton could be considered, at first sight, as a grave defect, for we could think that events will be their own veto, but this is not the case, because real veto (corresponding to detection of a γ in scintillator) is always "initiated" at the occurrence time of the event, but avalanche (and thus its "electrical observation" by anode and "optical observation" by anti-Compton) occurs only after drift time, thus if we require that anti-Compton "events" detection acts as veto only when it occurs before anode events detection, events won't be their own vetos; this is however a problem for Compton events occurring very close to the anode, and the frequency of such events has to be estimated; despite this, detection using avalanche scintillation light presents interesting features:
    - * distinguish electrical noise from physical events
    - * integration of ΣPM is proportional to the energy, as the integration of the anode signal, and energy resolution is even better with anti-Compton than with anode (PMTs are less sensible to the electromagnetical noise than anode), so now we determine the energy from anti-Compton
    - * when an event is crossing the anode, like an event corresponding to XY plane activity or going out of the TPC through the anode side, avalanche will be initiated by e^- present on both sides of the anode, moreover the drift velocity will be higher there than than in the custom drift zone (because of the high electrical field near anode wires), so the part of the track crossing the anode will appear "stronger" (and shorter) than the rest of the track (confusion between tracks ends or special projections can be avoid); this effect can be seen on the XY plane and on the anode but it is more obvious on the anti-Compton; from the anti-Compton information (i.e. with scirise, which is the value of the derivation of the initial part of ΣPM corresponding to avalanche scintillation light), adding eventually anode and XY plane information, we can reject most of these events
    - * the determination of tracks' ends, where the energy deposition is high, is better with the anti-Compton than with the anode

- α primary scintillation light in CF_4 can be seen by the anti-Compton
  (α of a few MeV, like ^{210}Po α of 5.31 MeV, and ^{214}Po α of 7.68 MeV, can only move a few millimeters in gas so the distance between ions and e^- resulting from ionization is low and the density of charge high, so that there is an important electric field between drifting ions cloud and e^- cloud, which will induce a non negligible recombination, corresponding to an important light emission) the anti-Compton gives thus the absolute Z position of the α decays in the gas, which make possible XY gain mapping with α
  (gain is strongly Z dependent for α, because the high e^- density will cause a screening effect which attenuates multiplication and thus gain; drift diffusion reduces electronic density, so that the screening effect is less important for α near of the anode than for α far from it, and thus the gain is proportional to the distance from anode for α; it is however difficult to evaluate the initial recombination and the diffusion screening effect, which depends of various parameters, but we can use the monoenergetic ^{210}Bi α coming from the cathode, see section 2.3., which have all the same Z position, to evaluate the relative XY gain)

The total number of photoelectrons is not only dependent of the initial number of photons (in the scintillator liquid or in the gas), but also of the position of that emission, because the solid angle on which PMTs will collect scintillation light photons and the attenuation of the latter when going through scintillator or by reflections in the detector are both varying with the position. The axial symmetry of the detector imply a high sensitivity to Z position, so it is useful to define the asymmetry:

$$Asymmetry \equiv \frac{\sum PM_{anode} - \sum PM_{cathode}}{\sum PM_{anode} + \sum PM_{cathode}} \tag{2.1}$$

Asymmetry is useful in the following cases:

- scintillation light coming from liquid scintillator
  asymmetry must be determined for each γ event occurring in the anti-Compton to correct energy calibration of the latter; anti-Compton calibration is done using ^{54}Mn, emitting γ of 835 keV and ^{137}Cs, emitting γ of 662 keV

- avalanche scintillation light coming from CF_4
  from "hard" $\sum PM_{anode}$ and "hard" $\sum PM_{cathode}$, we find that asymmetry is equal to 0.16 for e^-, 0.18 for μ and 0.06 for α
  (anode it situated "at one side" of the TPC, so the asymmetry should be ~ 0.5, but this is not the case because the avalanches produce a very strong scintillation light which can cause the saturation of $\sum PM_{anode}$)
  corresponding asymmetry distributions are too width to discriminate directly e^- from α, but can be used after other cuts to verify that the latter have been eliminated

2.1.3 Passive shielding

They are three principal passive shieldings:

- reactor building concrete + earth (see figure 2.1)
  reactor building is principally made of concrete and its ground is at -8m; this constitutes a protection against μ equivalent to about 20 m H_2O, which corresponds to a reduction by a factor 4 of μ terrestrial flux

- reactor building concrete between combustible and detector
  the distance between combustible and detector is 18 m, and corresponds to about 10 m of concrete (see figure 2.1); the latter prevents from reaching the detector α and β, and also almost all γ and neutrons (flux negligible in comparison of other flux of γ and neutrons, see below) generated by the combustible; the latter can thus be considered as a pure $\bar{\nu}_e$ source (flux of $\bar{\nu}_e$ of about $10^{13}\mathrm{cm}^{-2}\mathrm{s}^{-1}$ in the laboratory)

- passive shielding built around detector (see figure 2.8)
  different type of activity implies different type of protection:

  - γ whose most important source is the activity coming from the local of experiment (cleaning and cleanliness rules, like changing clothes, are necessary to prevent from bringing contaminants from "hot" or "dirty" parts of reactor); there are about 10^{10} γ in local each days, and we have different probabilities P that they move toward TPC and create Compton events of more than 300 keV non detected by the anti-Compton:

    $$lead \Leftarrow \begin{cases} * \quad \gamma \text{ is moving toward TPC} \Rightarrow \mathrm{P} \sim 0.2 \\ * \quad \gamma \text{ interacts in gas without anti-Compton detection} \Rightarrow \mathrm{P} \sim 10^{-6} \end{cases}$$

    ($\mathrm{P} \sim 10^{-6} \Leftrightarrow \mathrm{P} < 10^{-2}$ for a γ to cross anti-Compton without being detected $\cap$ $\mathrm{P} < 10^{-2}\mathrm{bar}^{-1}$ for a γ to create a Compton event of energy > 300 keV in the gas $\cap$ $\mathrm{P} \cong 3{\cdot}10^{-2}$ for a γ to be absorbed before crossing the anti-Compton or to cross the anti-Compton without being detected)
    we expect $\sim$ 10 $\bar{\nu}_e e^-$ scattering each day, so a lead protection is necessary; in this experiment the latter is 15 cm thick (figure 2.8) and corresponds to a reduction of $\sim 10^3$ of the γ flux so we finally expect a "noise" of 2 Compton events due to this γ flux for a 500 keV threshold, at 3 bar

  - neutrons are principally generated by the interaction of μ in lead
    (μ flux of about 30 $cm^{-2}s^{-1}$ $\Rightarrow$ 5 10^6 neutrons each day)
    γ and β uncorrelated with μ can result from thermalization and capture of neutrons, so protections are necessary; polyethylene (CH_2) is used to thermalize neutrons, and this polyethylene is "inserted" in a Bore shielding (figure 2.8); the latter capture neutrons and an α emission results from this capture; α are then absorbed by polyethylene, and a desexcitation γ of 482 keV is emitted; the total contribution of all γ events from cosmic origin is estimated to about 2 events each day, for a 500 keV threshold, at 3 bar

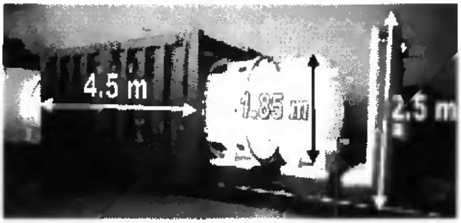

Figure 2.8: The passive shielding is composed of an outer part of lead and of an inner part of borated polyethylene (white). The vessel inside it (white) is the active shielding.

We can thus expect a noise of 4 Compton events with external origin, at 3 bar, for a 500 keV threshold (2 for γ flux and 2 for γ induce by cosmic events). The noise due to charged current $\bar{\nu}_e p \rightarrow e^+ n$ in acrylic and liquid scintillator is negligible. A noise of 2 Compton events with internal origine is related to the detector material concentration (measured) in elements U, Th, Cs, Co, K (U = 10^{-12} gg^{-1}, Th = 10^{-12} gg^{-1}, K = 10^{-7} gg^{-1} in acrylic) considering their position in detector, and the γ non-detection probabilities 10^{-2}bar^{-1} and 10^{-2} associated respectively to gas and scintillator, see above. The total of Compton noise expected each day is thus of about 6 events, for a 500 keV threshold, at 3 bar.

2.1.4 Acquisition

The electronic information coming from detector corresponds to:

$$TPC \Leftrightarrow \begin{cases} \bullet & \text{signals of } 2 \times 256 \text{ strips of XY plane} \\ \bullet & \text{signal of anode} \end{cases}$$

$$anti - Compton \Leftrightarrow \quad \bullet \quad \text{signals of } 2 \times 24 \text{ PMTs}$$

XY strips are grounded via charge pre-amplifiers (TRA1000). Connection between XY strips and preamplifiers is realized with PET flat cables and acrylic connectors.
A capacitance is used to "cut" SHV anode signal, and the latter is sent into a charge pre-amplifier (TRA1000).
Preamplifiers are situated as close as possible of detection planes, to avoid electromagnetical noise collection, but on the outer part of the passive shielding, because the electronic components are often source of activity.
The "preamplified" anode signals and the PMTs signals are sent into:

- "recording system" ⇒
  record events and send it to other computers for storage, analysis and visualization (it is under control of "triggers" and "soft"; the both will "say" which "events" to record and how to do it; control "at distance" possible)

- "triggering system" ⇒ generate triggers for recording system

The "preamplified" XY signals are only sent into the "recording system".

The main part of the "recording" system are flash ADC memories (FADC STRUCK). Each signal is sent into a 1024 word memory, a word corresponding to 8 bit ($2^8 = 256 \Rightarrow$ recorded amplitude have integer value from 0 to 255) continuously recording "samples" of signal into words, in a "circular way" (the "circle" is constituted of the succession of words) unless it receives a "trigger". The sampling frequency $\nu_{sampling}$ is 12.5 MHz, so each word corresponds to a period T equal to 80 ns, which give a total recording time of 80 μs for the 1024 words. This total recording time is sufficient to record "horizontal" events (i.e. crossing TPC on its whole length), with a fraction of time reserved to events occurring before (the mean drift velocity v_{drift} is about 2.70 cmμs^{-1}, so the time require to drift for a distance equal to the 1.60 m of TPC length is about 60 μs^{-1}, which is less than 80 μs). The Z resolution (related to $\nu_{sampling}$ and v_{drift}) is about 2 mm, which is the same than X and Y resolution (the latter corresponds to the distance between X and Y "square pitches" presents on X and Y strips)
When a trigger occurs it has 2 effects:

- "value 0" is given to the address of the word is situated "before" the word which was recording when the trigger occured
  (the number of words between these two words corresponds to pretrigger size, which is defined by "soft")
  "pretrigger" has two utilities:
  - the trigger can occur after event which have initiated the latter
  - we want to see what happened some time before event
- the FADC stops recording after having reached the word situated just before the word with address "0"

The principal function of "triggering system" is to generate $\bar{\nu}_e e^-$trigger. A $\bar{\nu}_e e^-$trigger will be generated when the following conditions are simultaneously realized:

- the integration of filtered anode signal has a value $\geq$ 300 keV
- the "avalanche" signal on anti-Compton is occurring at the same time ("prompt") than anode signal (see section 2.1.2)
- there is no veto coming from the anti-Compton (see section 2.1.2)

The FADCs send their data on a VME bus and are controlled by it. The latter is under control of a LECROY Universal Logic Module into which the different triggers and vetos coming from "fast electronic" are sent. The "slow control" data are also transferred into a VME bus. Counting rate information coming from "fast electronic" are sent to a CAMAC bus and then to a Macintosh, which is controlling the latter. The CAMAC bus controls also PMTs high voltage. Bus VME and Macintosh can send their data to DEC stations (Bugey laboratory), and terminals of Padoue, Zurich and Neuchâtel, and are under their control, by mean of the program CASCADE, written at CERN.

2.2 Tracking

One of the most spectacular and interesting feature of a TPC is its ability to give a 3D "photography" of ionization tracks in gas.
3D track topology is obtained in the following way (see section 2.1.1):

- XY projection of track is due to the charge induction on perpendicular X and Y strips that takes place after "multiplication" by the anode of the track's e^- having drifted perpendicularly to the detection planes (the electronic avalanche occurs quickly around anode wires, and the e^- enters into the latter leaving a positive ions cloud that drift slowly towards cathode; avalanche cannot be observed because its period is shorter than anode and X and Y strips preamplifiers rise time but the slowly drifting ions clouds induce a positive signal on X and Y strips, and a negative signal on anode, because they "retain" the e^- that have entered into it)
- Z "relative" coordinates and energy deposition along Z can be reconstructed by the time information on X and Y signals and on anode signals
  (we can consider that ionization occurs "instantly", so the tracks e^- that are close to anode arrive before e^- that are far from it; the time information gives thus relative Z information on track, but not absolute, i.e. we don't know where the track has occurred between anode and cathode)

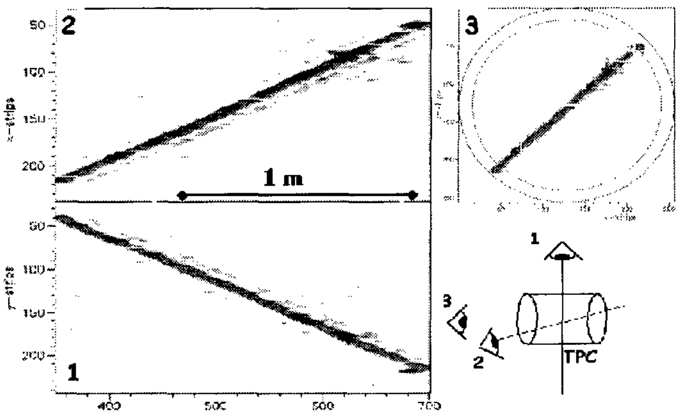

Figure 2.9: μ having crossed the TPC "diagonally". The XZ and YZ projections (on left) give already the whole 3D information. We can also see the XY projection (on right).

Pictures like figure 2.9 or 2.10 have been realized with program DISP, which "unpacks" acquisition files generated by program CASCADE by mean of ZEBRA routines and can generate n-tuples by mean of HBOOK routines. DISP has then two roles:

- **full TPC**

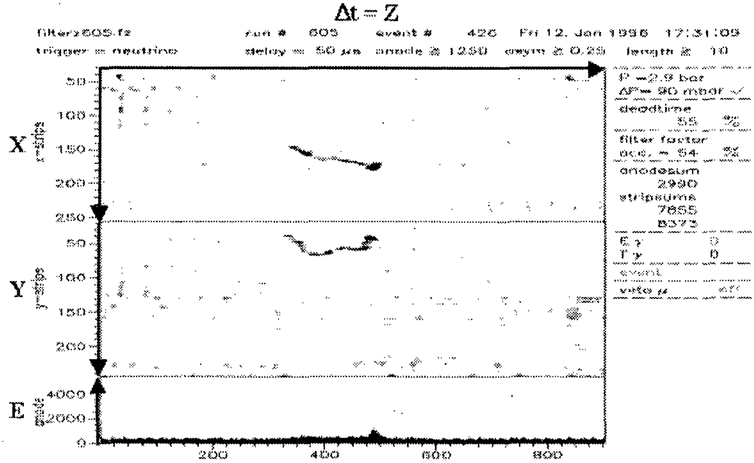

Figure 2.10: XZ and YZ projections of a "single" e^- fully contained in the TPC, with its start (we see that the scattering angle is clearly identifiable) and its end. The latter is identifiable by a "blob". The anode signal is proportional (after having subtracted the pedestal) to the energy E left by the e^- along Z and its integration along the track is proportional to the initial kinetic energy of the e^-

- visualization of the information given by:
  - TPC
    there are many possibilities to represent TPC events or related information (in figure 2.10 we can see the XZ and YZ projections of a fully contained e^-; there are also many other features, like visualizing the XY projection, in which we can easily see if an event is going out of the TPC, "zooming" on events or representing single strip signal and "additional" information, such as the type of trigger or the pressure of the gas)
  - anti-Compton
    it is possible to visualize information coming from PMTs
    (we can see a single PM signal and ΣPM signal, which can be used to the identification of anti-Compton events like γe^- scattering, i.e. Compton events, clearly identifiable by a narrow peak, and of events crossing the anode by the derivate of ΣPM, i.e. scirise, or serves to visualize the avalanche scintillation light, see figure 2.16, which is proportional to the energy)

- scanning, i.e "manual" determination (using DISP features) of some event's characteristics and filling an n-tuple (matrix) with the "whole" information concerning events
  (one line of the n-tuple corresponds to one event; n-tuple filling occurs after "clicking" on the "class" of the latter)
  "whole" information means:
  - information that have been determined during scanning
    - events "class", i.e.:
      - its type like "single" e^-, e^- with trigger γ that have passed low anti-Compton threshold, α, μ, $\beta\alpha$ decay, discharges, etc. (see section 2.2.1) (an important part of the "undesired" events has already been eliminated by "hard" veto and "soft" filtration of the acquisition files, however a finer analysis with DISP is necessary)
      - "in" or "out" event, which is deduced from "tracking" ($\Leftrightarrow$ classes e-in or e-out for e^-) (we have defined a fiducial radius, whose radius of 42 cm is a little shorter than internal TPC's radius, to determine if an e^- is "in" or "out"; this fiducial radius is also used for Monte-Carlo simulations; the determination of the initial kinetic energy of the e^- is only possible for "in" events)
    - "tracking" information concerning e^- in (and eventually e^- out) such as:
      - scattering angles
        (to determine scattering angles we have to differentiate the start from the end, which corresponds to a blob, and to put on tracks (using DISP features) a vector "tangent" to the initial "trajectory" of the "scattered" electron, see section 2.2.2; e^- can only scatter "forward" in $\bar{\nu}_e e^-$ events, i.e. from "combustible" to detector, the scattering probability growing when the opening of the "scattering cone angle" is becoming shorter, so the information on scattering angle is essential, see section 1.2 and 2.2.2)
      - length
        (length is proportional to energy and less sensible to gain variation, see section 2.2.2; energy is not a tracking information, because it is calculated by DISP, which integrates anode signal and substrates pedestal after having determined the latter)
  - DISP information, such as:
    - calculated information, like energy, pedestals, etc.
    - information already contained in acquisition files like no of event, 1024 length anode, strips and PMTs vectors, etc.

The N-tuples analysis is done with the program FILL.

Capacities of XY planes and anode are important, and these detection planes can be considered as antennas very sensitive to electromagnetic noise coming from inside (it can come from electronic of PMTs, detection planes itself, etc.) and outside of the detector (noise can come from acquisition cables, crates power supply, mass currents, etc.). The anti-Compton, the passive shielding and the TPC itself with its fields shaping rings correspond to a good Faraday cage, however the amplification system is situated outside of the detector, and, despite the building of an external Faraday cage to isolate from electromagnetical noise the strips flat cables and the anode cable, both leading unamplified signals to preamplifiers, noise can still be collected. The preamplifiers output is differential, to substrate noise that can be acquired after amplification, nevertheless noise collection is still possible at this level. The initial electromagnetical noise was too high, and we have done many efforts such as to determine and to isolate the different sources of noise, to avoid mass current by putting the detector, the mass shieldings of the differential cables and of the electronic at the same ground, etc. A significant reduction of noise giving clearly identifiable tracks has been obtained, but a higher reduction was still needed to separate clearly signal from noise on the whole track length, especially to measure scattering angles and identify "in" e^- from "out" e^-, but also to make possible eventual automatic events filtration or scanning. A soft treatment of the electromagnetic noise was then added to DISP. It is realized in the following way:

- make a spectral decomposition of the signal with a Fourier transformation
- cut frequencies values that contribute much to noise but not much to track information $\Rightarrow$
    - cut frequencies $\geq$ 600 kHz
      (smallest spatial physical signals extensions $\Leftrightarrow$ tracks width $\Leftrightarrow$ 2 μs in drift time $\Leftrightarrow$ frequencies $\leq$ 500 kHz)
    - cut frequencies $\leq$ 20 kHz
      (these frequencies corresponds essentially to pedestal fluctuations)
    - cut the 3 frequencies having the highest spectral densities
      (noise contribute more than signal to the density of these frequencies)

The most important components of noise were eliminated, with an acceptable loss of resolution. Tracks' components of the order of characteristics tracks lengths can't be eliminated. However the quality of tracks is now "good", and it is possible to see 3D contained e^- of energy as low as 100 keV (see figure 2.11) up to a few MeV and to distinguish start from end, to measure scattering angle and length.

2.2.1 Event identification

Some examples of the tracks realized with MUNU detector, and different uses (some were discovered during experiment) of the 3D tracks visualization features are presented in this section.

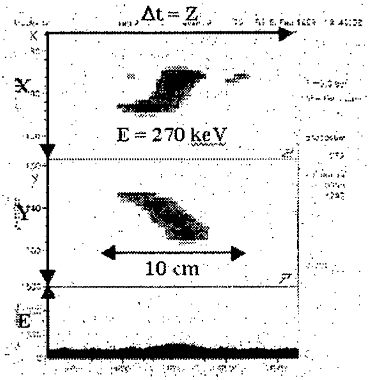

Figure 2.11: e^- contained in the TPC filled with 3 bar of CF_4, whose initial kinetic energy is about 100 keV, i.e. situated below the TPC's detection threshold that has been chosen for the experiment (TPC's detection threshold is equal to 300 keV while anti-Compton veto is equal to 100 keV, see section 2.1.2), corresponding to a total length of about 10 cm only (total drift length of 162 cm). We see that even for so small tracks, it is possible to distinguish the start from the end (wider than the start) and to measure the scattering angle.

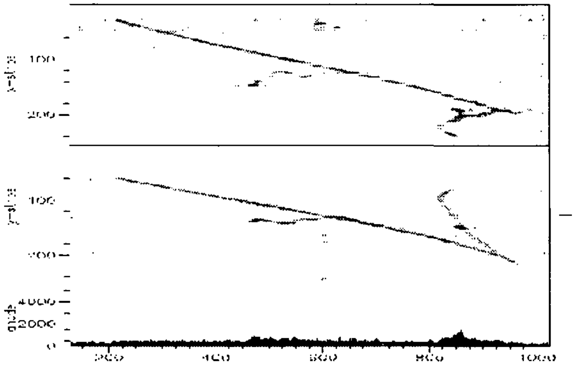

Figure 2.12: Cosmic μ producing 2 high energy δ e^- (by scattering with e^- of CF_4). The e^- near the center, whose energy is about 1 MeV is contained inside of the TPC, and the increased charge density (blob) at its end is clearly visible. μ should correspond to straight lines (or to lines with "kicks" corresponding to single scattering with the nucleons of the gas); this is almost the case, but not completely, which indicates that the potentials of the field shaping rings have to be adjusted, see section 2.3.4.

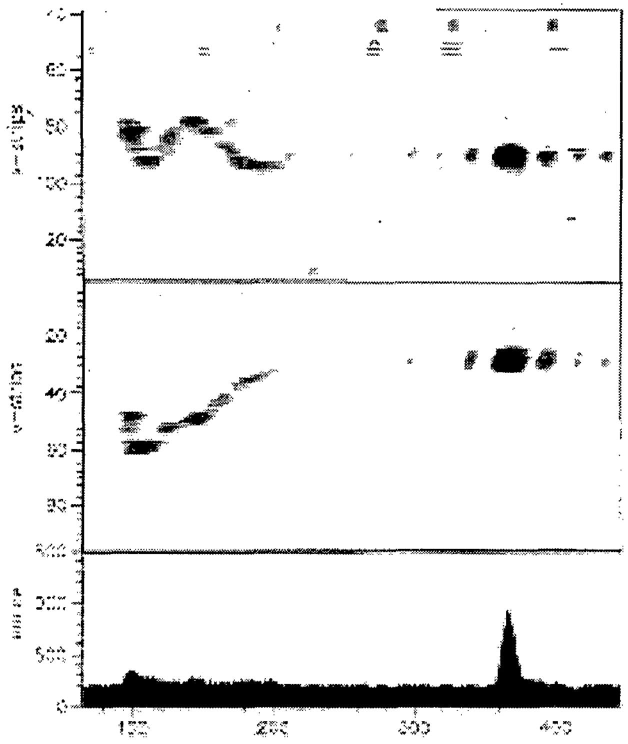

Figure 2.13: Radon, whose isotopes belongs to "natural" decay chains, is the most probable source of α that can be observed in the TPC, because it is gaseous at "ambient" temperature, and can therefore go out from the solid detector's material and enter into CF_4. ^{222}Rn belongs to ^{238}U decay chain. It decays until stable ^{206}Pb through α and β decays. The β decay from ^{214}Bi to ^{214}Po is followed by an α decay from the latter to ^{210}Pb. The half life of ^{214}Po is equal to 162 μs. An appreciable fraction of these $\beta\alpha$ decay events can thus be observed in the 80 μs acquisition time. We see here a $\beta\alpha$ event corresponding to such a transition and thus indicating the presence of ^{222}Rn. β and α are emitted from the same nucleus, and difference between Z coordinates of α and β emission position observed after acquisition corresponds to the difference between α and β emission time. ^{220}Rn belongs to ^{232}Th decay chain. It decays until stable ^{208}Pb through α and β decays. There is also a $\beta\alpha$ decay in this chain, corresponding to a β decay from ^{212}Bi to ^{212}Po followed by an α decay from the latter to ^{208}Pb, but the half time of ^{212}Po is only 0.3 μs, and such $\beta\alpha$ events seem to be in spatial and temporal coincidence.

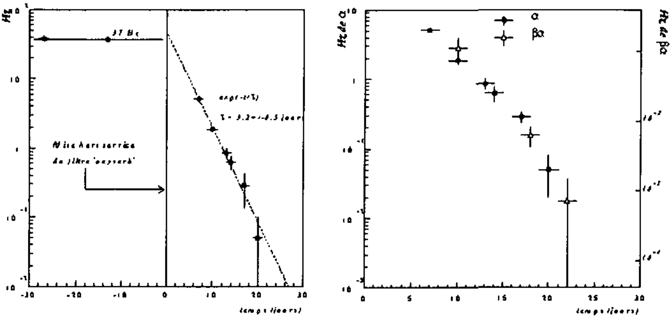

Figure 2.14: α events at a rate of 35 s^{-1}, indicating the possible presence of radon, and also $\beta\alpha$ events, "signature" of the presence of ^{222}Rn (see figure 2.13), were observed in the initial phase of the experiment, when it became possible to visualize tracks. One possible source of radon was the OXYSORB filter used then to clean CF_4. OXYSORB was removed and an analysis of its 300 g zeolite content showed a constant rate of 32.7 s^{-1} corresponding to the presence of ^{238}U with a secular equilibrium of its decay chain daughters. Zeolite of other OXYSORB filters had already been tested before and were not showing such a ^{238}U contamination. The OXYSORB filter used in MUNU experiment had not been tested, because the test is destructive, and unfortunately it was this one which was contaminated (the contamination has probably occurred during its fabrication). Measurements of the decay rate were done after removing OXYSORB. In the figure on left, we can observe the constant α rate before removing OXYSORB and a decreasing rate after removing OXYSORB. The decreasing rate has a period of 3.2 day corresponding to ^{222}Rn decay period but not compatible with the shorter one of ^{220}Rn, which confirms the contamination with ^{222}Rn. The figure on right shows the good correlation between $\beta\alpha$ events and α rate. The gas was then changed and a SAES filter was installed. The ^{222}Rn level of the latter was measured at a rate of 0.011 s^{-1}, which is acceptable if the active charcoal trap is used. However the TPC had been exposed to ^{222}Rn and its daughters during a few months. The α decays produce electrically charged atoms, which can thus fixe themselves inside TPC, principally on cathode and XY plane. The first "long life" daughter of ^{222}Rn is ^{210}Pb, with an half-life of 22 years and can thus contaminate cathode and XY plane. ^{210}Pb decays to ^{210}Bi and from the latter to ^{210}Po through β decays, and decays finally to ^{206}Pb through an α decay of 5.31 MeV. These α were observed on cathode, at an energy of 940 keV e^- equivalent (gain is less for α than for e^-; α can be localized with their scintillation light, see section 2.1.2), with an activity of 17 μBqcm^{-2}. This was still too high for the experiment, and cathode was replaced by a new one (which is a very delicate operation). The α rate was then divided by about a factor 10. It is not possible to observe α (and then to measure ^{210}Pb contamination) on the XY plane, and thus the corresponding β decays could be an important problem. However, a way to recognize β coming from the XY plane was found, see figure 2.15.

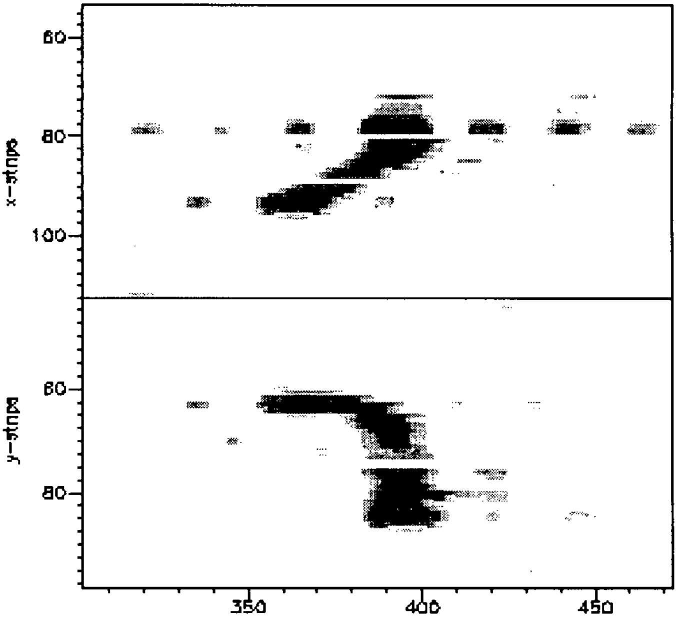

Figure 2.15: When a part of an e^- track is contained in the amplification zone, i.e. between the grid and the anode, (like for e^- corresponding to XY plane activity, for example ^{210}Po β decay, e^- resulting from Compton scattering inside amplification zone or e^- "entering" into detection planes) the corresponding avalanche will be more "intense" and the part of the track contained in the amplification zone will appear "stronger" than the rest of the track (see section 2.1.2), except for its end or special projections. The events having their origin inside of the amplification zone or on the XY plane, and ending inside of the TPC's drift zone, will then appear with one blob on each extremity, (with every time a clear "extremity" of the track on the anode side). Such "biblobs" events don't correspond to $\bar{\nu}_e e^-$ scattering events in the gas and have to be rejected. However the scintillation light coming from the avalanche is more efficient to reject such events, with the "scirise" criteria, see figure 2.16.

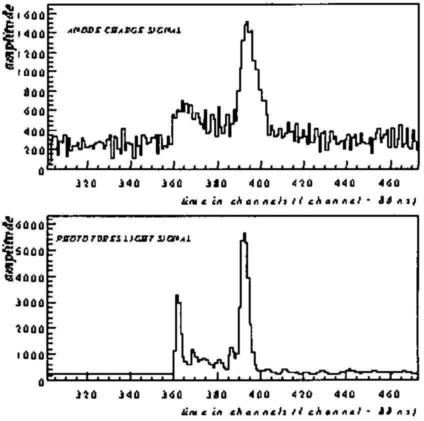

Figure 2.16: When a part of an e^- track is contained inside of the amplification zone, the corresponding avalanche is more intense than in the rest of track and therefore the scintillation light is also more intense. Moreover the "primary" e^- entering in that zone of intense electric field is producing more scintillation light than on the rest of its track. In the first figure we see the anode signal corresponding to the avalanche of the "biblob" event of figure 2.15, and in the second figure its anti-Compton signal, with a clearer "biblob" effect than in the first figure. It has been shown that for biblobs signals the time derivative (called "scirise") of the part of the anti-Compton signal corresponding the blob situated on the anode side (were the e^- was supposed to enter in amplification zone) was greater than 1500 mv / 100 ns, and smaller than this values for "blobs" corresponding to custom tracks ends. This condition can thus be used as a cut to rejects "biblobs" events, but also events entering into the detection planes. The Compton events occurring very close to the detection planes but not inside of the amplification zone, whose corresponding "strong" γ anti-Compton signal could be confused with the initial avalanche scintillation light, are also rejected by cut "scirise". Tests with Compton events generated by a source (with the condition that associated scattered γ ray signals are well separated from the avalanche signal, so that these Compton events occur far from anode) have shown that only 1.5% of the e^- will be wrongly identified as originating or going through anode. The analysis of the angular distribution of the events rejected by scirise has shown that most of them were "oriented" from anode to cathode. The rate of these events is 0.11 s^{-1}, for a 300keV threshold. The high rate and the orientation can be explained if we consider that the events correspond mostly to a contamination of the XY plane by ^{210}Po. The α rate observed close to the anode is lower (0.06 Hz) than it should be for such a contamination, but this can be related to the short spatial extension of α and to to the corresponding value of the gain, which is about 4 times lower for α generated on the anode side than on the cathode side (see section 2.1.2), so that the detection of α close to the anode is much more difficult than the detection of β. The level of ^{210}Po on the XY plane was estimated at 6.22 cm^{-2}s^{-1}.

2.2.2 Angles and length

The strong utility of scattering angles measurement is related to the following features:

- In a $\bar{\nu}_e e^-$ event, the e^- is always scattered forward (see section 1.1), i.e. with $0 \geqslant \theta_{z,rea} \leqslant \frac{\Pi}{2}$, where $\theta_{z,rea} \equiv$ scattering angle in relation to axis reactor → detector ("reactor" meaning here "combustible")$\Rightarrow$
  - online background rejection possible by subtracting the backward events (i.e. $\bar{\nu}_e e^-$ "like" events going from detector to reactor) count rate from the forward events (i.e. $\bar{\nu}_e e^-$"like" events going from reactor to detector) count rate, giving thus a spectra in function of the initial kinetic energy of the recoil e^-; this spectra corresponds to the $\bar{\nu}_e e^-$scattering spectra only if the spatial distribution of the background is homogeneous around TPC Z axis, which can be checked during reactor OFF "interval"; if it is not the case the background asymmetry observed in function of the initial e^- kinetic energy has to be taken into account
  - background asymmetry measurement by subtracting the forward $\bar{\nu}_e e^-$ "like" events count rate from the forward $\bar{\nu}_e e^-$"like" events count rate, both measured for the OFF "interval", giving thus an "asymmetry" spectra in function of the initial kinetic energy of the recoil e^-; this asymmetry spectra corresponds to the background asymmetry spectra only if we consider that the reactor contribution to the forward background is negligible (this should be the case, see section 2.1.3), and that no new detector contamination has occurred after the OFF "interval"

- suppress an "hot" source by a cut on angle (for example a "cut" was "applied" to the events "acquired" before changing cathode and coming from the latter, like β events corresponding to ^{210}Po β decay; it was realized by rejecting all events whose initial track angles corresponded to unit vectors belonging to a half sphere oriented from cathode to anode; it has reduced the expected "signal" by a factor 2 but noise by a factor 3 and was thus "interesting"; it seems however that the β activity on the "old" cathode is "rather" symmetrical around the TPC's Z axis, because it should have the same spatial distribution than α activity, which seems homogeneous, and therefore, in an online noise suppression, it will "only" contributes to the uncertainty of the spectra)

- measure the count rate in the region where the sensitivity to the magnetic moment is maximal, i.e. for events with scattering angle close to 0° and initial kinetic energy of about 350 keV; unfortunately this test is not realistic in our case, because of the important background level at this low energy value

The measurement of the length can also be useful. It is possible to compute the energy left by an electron in function of the length of its track, for a given gas density. The length is sensible to the drift velocity (which can be precisely determined), but is less sensible to the variations of the gain that the energy measured from anti-Compton or anode signals.

I have realized some Fortran routines (display and calculation) integrated in DISP to determine "manually" tracks scattering angles (in spherical coordinates) and tracks lengths, and I have added a routine realized by Jean-Luc Vuilleumier to compute initial e^- kinetic energy from its tracks length, in function of the density of CF_4.
Some modifications were done by Almut Tadsen for zooming compatibility and a routine for a "semi-automatic" determination of the scattering angles has also been realized.

The determination of angles and length requires two "human" operations:

- find the 3D vertex position (the vertex is the initial part of the tracks, where scattering occurs; there is in general no confusion possible between the vertex and the end of the track, the latter corresponding to blobs visible in each projection)
- fit the 3D tracks from the start (vertex) to the end with connected line segments

The "manual" tracking mode is used if we want to determine the angles of scattering and the length of the track. It requires clicking successively on XZ and YZ tracks projections (when clicking on a frame to determine the 3D projection of the vertex or of a point connecting two line segments, the Z coordinate of the corresponding projection of the same point in other frame is already determined, and a narrow rectangle crossing the track appears in that frame to restrain the clicking area).
The semi-automatic tracking mode is used if we want only tó determine scattering angles and requires manual vertex determination. A segment tangent (vector) to the track in XZ and YZ projections is then found by the program (a 3D longitudinal box is turning around vertex position and stops when the number of point higher than a given threshold is maximal, which means that the box has "catched" the track).
The scattering angles (i.e. θ and ϕ, in spherical coordinates) are calculated from the first 3D vector $\equiv$ scattering vector (in manual tracking it is defined by the 2 projections of the vertex and the 2 projections of the first point connecting 2 line segments), which has to be tangent to the track. The length is defined as the sum of the lengths of all line segments.

Scattering angles are calculated for 2 referentials:

- the detector referential:
    - Z_{det} axis is oriented from anode to cathode
    - X_{det} axis is oriented vertically, from the bottom to the top of the reactor, perpendicularly to X strips (each X strip corresponding to a defined X_{det} coordinate)
    - Y_{det} axis is oriented horizontally, from the interior to the exterior of the reactor, perpendicularly to Y strips (each Y strip corresponding to a defined Y_{det} coordinate), i.e. Y_{det} axis $\equiv Z_{det} \wedge X_{det}$

  the detector referential is useful for example to examine cathode contamination

- the "reactor" referential:
    - Z_{rea} axis is parallel to ν flux, i.e. oriented from the center of the combustible to the center of the detector (i.e opposite to the direction of arrow of figure 2.1), making an angle of 46.5 ° with an horizontal plane
    - X_{rea} axis $\equiv Z_{det}$
    - Y_{rea} axis $\equiv Z_{rea} \wedge X_{rea}$

  the reactor referential is the "natural" one for $\bar{\nu}_e e^-$ scattering observation

DISP is using integer coordinates to describe the referential "XYZ", which is oriented following detector referential. X and Y coordinates can take values from 0 to 255 corresponding to 256 strips X and 256 strips Y. Z axis can take value from 0 to 1023 corresponding to the 1024 acquisition words for X, Y, anode and PMTs signals. This referential has to be set on the "physical" scale for angles and length calculation. The DISP scale distance between two successive "bins" X, Y or Z, is 1 and, at the "physical" scale, it corresponds to

- 3.5 mm for X or Y coordinates
- about 2 mm for Z coordinates, which corresponds to $T_{sampling} v_{drift}$, i.e. e^- drift distance during 1 acquisition sample, see section 2.3.1
  (with $T_{sampling} = 80$ ns $= \nu_{sampling}^{-1} = (12.5 MHz)^{-1}$ and $v_{drift} = 2$ to 3 cmμs^{-1})

Spherical coordinates are used to describe scattering angles in detector and reactor referentials using the usual conventions:

- θ ($\theta_{z,rea}$ and $\theta_{z,det}$) defines the angle relative to Z axis, with value 0° when the scattering vector and the Z axis orientations are identical (for example when the direction of the scattered e^- corresponds to the direction of the incident $\bar{\nu}_e$, in the reactor referential)
- ϕ ($\phi_{z,rea}$ and $\phi_{z,det}$) defines the angle of scattering vector projection in XY plane, relative to X axis, and the positive angle sense is given by Z axis orientation

The calculation of scattering angles is done using the scalar product formula, i.e. $\vec{a}\,\vec{b} = \|\vec{a}\|\|\vec{b}\|\cos\alpha$ between Z axis (unit vector) and scattering vector to find θ angle and between X axis (unit vector) and scattering vector projection in XY plane (from θ angle) to find ϕ angle. The reactor axis (unit vector) is expressed in the detector referential for angles calculation in the reactor referential. The angular resolution has been measured by reconstructing the energy of incident 835 keV γ of a ^{54}Mn source in Compton scattering (by measuring the energy left by the incident γ and its emission time in the scintillator, the energy and scattering angles of the e^- in the gas and the difference between the time of observation of the e^- and the γ emission time, this difference corresponding to the drift time and determining the 3D absolute vertex position, see section 2.1.2).

The energy resolution obtained for the reconstructed 835 keV photopeak was $\sigma_E = 225$ keV, corresponding to an angular resolution $\sigma = 39.7\,^\circ \pm 2.2^\circ$ averaged over the Compton recoil spectrum above 300 keV. It seems that it is the first time that a photopeak of about 1 MeV is reconstructed by measuring the Compton scattering in a gaseous detector. The incertitude on angular resolution is related to various factors, such as:

- e^- multiple scattering (which is one of the main limit to angular resolution)
- incertitude on vertex determination (due for example to electronic noise)
- limits on track resolution (coming for example from the "granularity" of the detector, which corresponds to 3.5 mm for X and Y coordinates, and 2 mm for Z coordinates, see above, or from the diffusion during drift, which is of about 2 mm on the whole drift length, i.e. "not larger" than granularity)
- bad configuration of the drift field, which causes tracks deformations (section 2.3.4)
- combustible (width = 1.5 m, height = 2 m) is not a punctual $\bar{\nu}_e$ source and $\bar{\nu}_e$ detector (width = 1.6 m, height = 0.9 m) is also not punctual (these dimensions have to be compared with the distance of 18 m between combustible and detector)

The "manual" measure of length is possible and give good results, except in case of "complicated" trajectories or "important" δ e^-. Measurements with the ^{54}Mn source has shown that the energy resolution obtained from length measurement is comparable to that obtained from anti-Compton or anode signals (section 2.1.1). However energy measurement has been done mainly from the integration of anti-Compton or anode signals.

2.2.3 "in" and "out" events

The 3D coordinates of the event determine also the "containment" of the latter (3D coordinates of a track "point" are obtained by clicking on the 2 projections of the latter; the "radius" corresponding to the distance between this point and the Z axis of the cylindrical TPC is then calculated, if it is greater than the fiducial radius, i.e 42 cm, for one part of the track, the event is considered as "out")
The e^- "containment" in the fiducial volume must be determined, for two reasons:

- determine the total initial kinetic energy of e^-
  (non-contained events don't loose all their energy in the gas, so their total initial kinetic energy cannot be measured)
- reject all e^- coming from the exterior of the fiducial volume
  (e^- not rejected by an anti-Compton veto and coming from the exterior of the fiducial volume will mainly correspond to β decays coming from TPC walls)

The main part of out events are now rejected automatically. Some events can be kept by the filtering program and have to be rejected after "manually", but no "in" events will be considered as out.

2.3 TPC calibrations with μ

This section corresponds to the presentation of the "principles" and results of a program (integrated in FILL) that I have realized to do calibrations (i.e. measurements of the relative variations of the "global" gain in time and of the drift velocity) and mapping (i.e measurement of the relative variations of the "local" gain in space and in time, corresponding to XY mapping and Z attenuation) with muons (I have presented these "principles" and results at an internal meeting at Padova; the first intention was writing a program for automatic scanning). Jacob Lamblin have realized then a program simpler and faster, based on the same "principles"; daily calibrations (concerning "global" gain and drift velocity) are now realized with that program.

We have decided to look if it was possible to use μ for TPC calibrations for the following reasons:

- μ ionizes gas in the "same way" as e^-, which is not the case for α, see section 2.1.2
- the flux of μ crossing the TPC is "important", of about 65 s^{-1}
- the spatial distribution of μ in the detector is homogeneous
- μ have a clear detection "signature"

$\Rightarrow$ "Global" and "local" calibrations in correspondence with e^- observation and initial kinetic energy measurement seem possible and realizable in a "continuous" and automatic way.

μ can loose their energy in matter by ionization ("normal" ionization along μ track and δ e^-) and radiative (principally bremsstrahlung and e^+e^- creation) processes. We can distinguish 3 energy classes and look at the corresponding value of energy loss in matter $dT_\mu dx^{-1}\rho^{-1}$, with $dT_\mu \equiv$ kinetic energy left by the μ, $dx \equiv$ distance covered by the μ and $\rho \equiv$ material density, which depends only of the material type and of T_μ:

- "high" energy μ, which loose energy by ionization and radiative processes
  $\Leftrightarrow$ "high" $dT_\mu dx^{-1}\rho^{-1}$
- minimum ionizing μ, whose energy is situated "between" "high" energy μ and "low" energy μ, which loose energy only by ionization processes, and whose corresponding energy losses in matter are minimal
  $\Leftrightarrow$ "low" $dT_\mu dx^{-1}\rho^{-1}$
  (in CF_4 $dT_\mu dx^{-1}\rho^{-1} \sim 3$ MeVcm^{2}g^{-1} $\Leftrightarrow$ $dT_\mu dx^{-1}$ at 3 bar $CF_4 \sim 30$ keVcm^{-1})
- "low" energy μ, which loose energy only by ionization processes, but more than minimum ionizing energy μ for the same covered distance, because they "spend more time" near atoms and are thus interacting more with the latter
  $\Leftrightarrow$ "high" $dT_\mu dx^{-1}\rho^{-1}$

The TPC is situated at a level of about 20 m H_2O equivalent, see section 2.1.3. At this level we can expect more minimum ionizing μ than "high" and "low" energetic μ ("high" energetic μ loose "quickly" their kinetic energy in matter, and a lot of them become minimum ionizing μ; minimum ionizing μ loose "slowly" their kinetic energy in matter and don't become easily "low" energetic μ; "low" energetic μ loose "quickly" their kinetic energy in matter and a lot of them will be stopped before reaching TPC). Minimum ionizing μ correspond to straight tracks in CF_4 and to a narrow $dT_\mu dx^{-1}$ distribution.
For these reasons ("simple" tracks, abundance, narrow energy loss $dT_\mu dx^{-1}$ distribution) minimum ionizing μ are selected to do global and local calibrations.
With the help of some figures, I will explain how μ can be used to do TPC calibrations. The main steps are:

- get the 3D absolute track coordinates of μ
(by determining the time of occurrence of μ event, see figure 2.17 and 2.18, and by fitting the μ track, see figure 2.22 and 2.23)

- determine the global gain by the selection of minimum ionizing μ
(by computing $\Delta T_\mu \Delta x^{-1}$ for an "important" number of μ, where Δx $\equiv$ μ track length inside of the TPC, and by fitting the distribution spectra obtained with a Gaussian curve to select minimum ionizing μ)

- compute the "local" gain for XY mapping and Z attenuation
(by computing, on a large number of μ, the mean $< dT_\mu dx^{-1} >$ of the integration of the anode signal corresponding to a μ whose absolute Z coordinates have been determined, divided by the value, for that μ, of the length contained in the zone defined, see section 2.3.1)

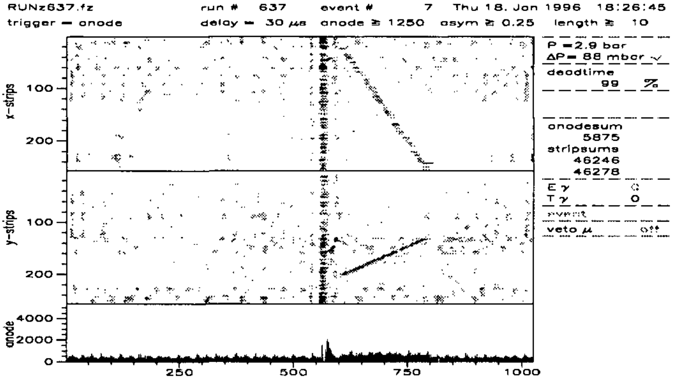

Figure 2.17: μ track and μ induction signal.

The 2 "oblique" straight lines of figure 2.17 (upper and lower frames) correspond to the projections XZ and YZ of a μ crossing the TPC. The 2 vertical lines of the same figure corresponds to a signal induced on XY plane by the electronic noise emitted by PMTs when the latter detects the very strong scintillator light produced by a μ crossing the anti-Compton. This induction occurs also on anode plane, see figure 2.17. Almost in the beginning of anode induction signal, corresponding to the time of occurrence of the μ event (μ "start" time), the value of some bins is equal to zero. A number of bins with null value greater than 1 is a clear indication of a μ induction signal; this condition is used in automatic TPC calibrations to select μ and to determine μ start time.

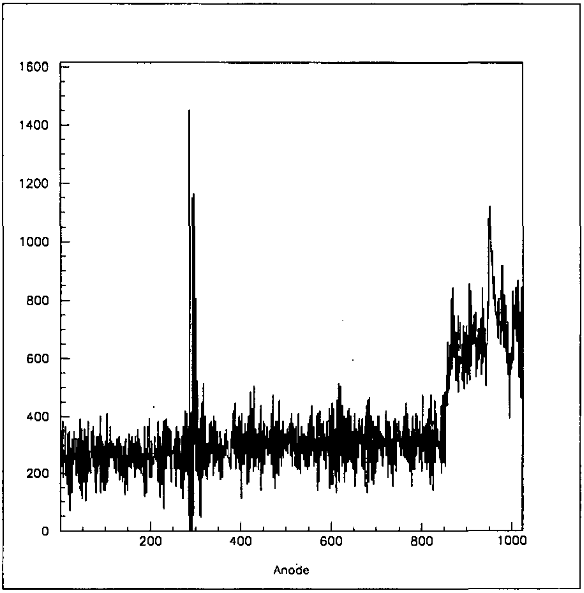

Figure 2.18: Anode signal with induction signal corresponding to μ start time, on left, and μ avalanche signal, on right. The time difference between the start of μ avalanche (signature = "fixed" number of bins higher than a "fixed" threshold) and μ start time (signature = more than 1 bin with null value) is equal to the absolute Z coordinate of the μ track point situated closest to the anode (because this difference corresponds to the time taken to drift until anode by an e^- of the track situated nearest anode when μ event occurred). The latter is used to "attach" the relative (translation of track possible along Z) track coordinates obtained by fitting (see figure 2.22), i.e. to get the absolute 3D coordinates of the whole track (see figure 2.23)

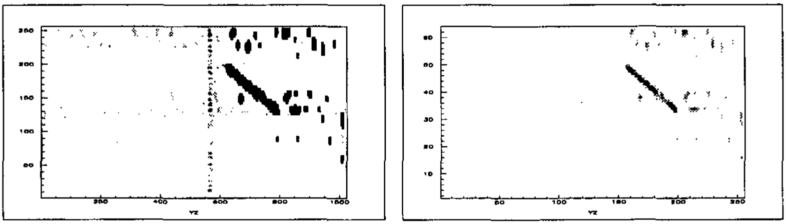

Figure 2.19: Projections XZ and YZ are "scanned" with "squares" of 4 × 4 "bins". When the mean of the value of the bins of a square is higher than a "fixed" threshold and also when the value of 1 bin of this square is higher than another "fixed" threshold with higher value, the square is "kept". Some routines were initially realized with the intention of doing an automatic "topological" analyze (i.e. to get information like "starts", "ends" and "embranchments" position, length and scattering angles value, "in" or "out", local energy deposition, etc.) on all type of events (i.e. not only μ, but also single e^-, e^+e^-, etc.) to perform scanning (see section 2.2) in an automatic way (by putting topological information together with other ones, like scirise, type of trigger, etc.). Steps described by figures 2.19 to 2.21 correspond to these routines and are not necessary for μ analysis.

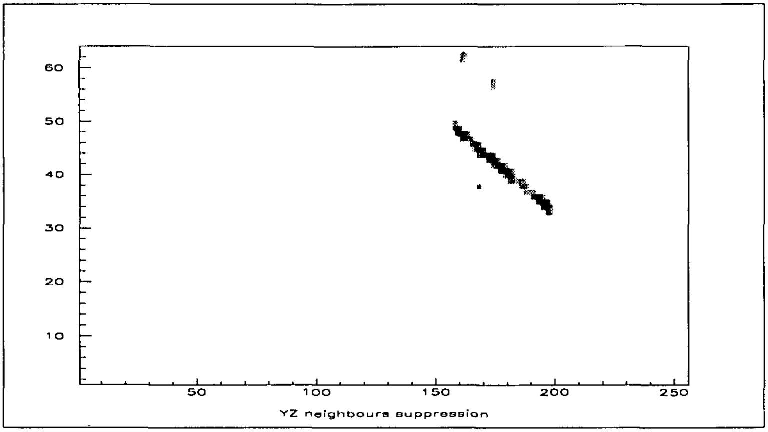

Figure 2.20: A fraction of the remaining noise is eliminated, requiring for each square a minimal number of neighbor squares "aligned" and in connection with the latter, in various directions" (works also for e^-, α, etc.).

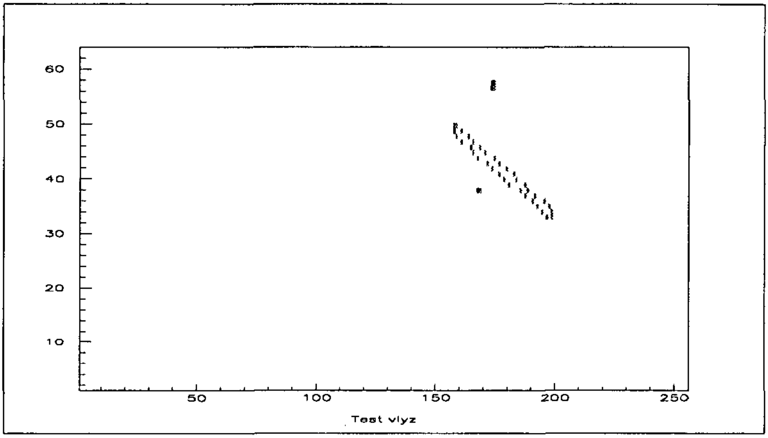

Figure 2.21: The contour of the track (squares with "neighbors" whose value is equal zero and with "neighbors" whose value is different of zero) is determined on each projection. Then the program turns around the track, from contour square to next "neighbor" contour square (the dark square mean that a complete turn has been achieved), computing rotation angles between each square and contour length during its rotation. With the information get in that way on both projections, "fractional" fits (simple fits in case of μ), and energy deposition along Z with anode or PMTs signals, we obtain the 3D topological information for the track (scattering angles, start, blobs, etc.). However this part of the program is not achieved and the latter has been "oriented" for TPC calibrations with μ. A program for automatic scanning has been realized at Grenoble, and is now working. Its principle corresponds to "catch" the whole track with a succession of 3D rotating longitudinal box (when one box has catch the track, a "new" box begin to rotate from the end point of the "old" one). The semi-automatic determination of scattering angle was also realized in that way, see section 2.2.2.

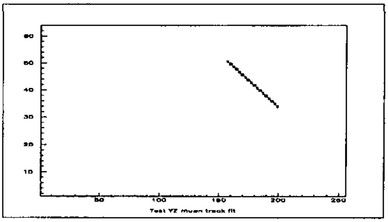

Figure 2.22: A linear fit of the μ track is realized on both projections. Only μ track with "good" fits, i.e. with "little" χ^2 fit value are used for calibrations (for example "curved" μ or μ with "important" δe^- correspond to "high" χ^2 fit values and are not kept for analysis). The "scaled" 3D fit coordinates are then computed, see section 2.2.2. The points of the 3D fit whose Z coordinates correspond to an avalanche signal on anode (and thus to μ track) are kept, the other are set to zero value. The μ induction signal is used to get absolute Z information, see figures 2.17 and 2.18. We obtain in that way the 3D absolute coordinates of μ tracks, i.e. their "trajectories" across TPC.

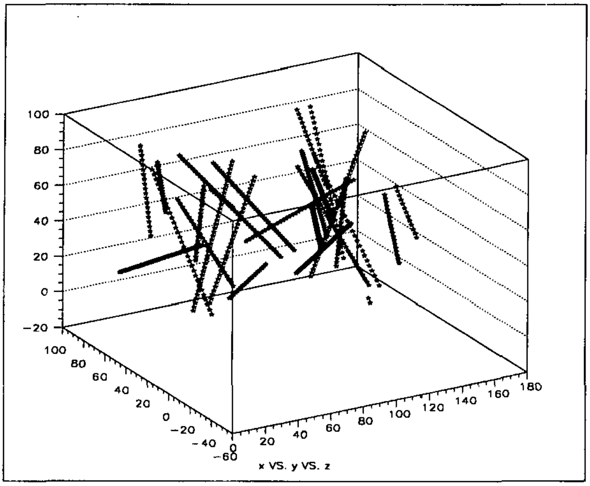

Figure 2.23: Some 3D μ "trajectories" are represented here. We can see that they are distributed in a 3D cylinder corresponding to TPC. The "small" inhomogeneities in μ distribution are only due to statistical fluctuations.

2.3.1 "Global" calibration with μ

When a e$^-$ ionizes the gas, it loses at each ionization a constant energy quantity $w_{ionisation}$. The initial kinetic energy T_e of the e$^-$ is thus proportional to the initial (i.e. before drifting) number $n_{initial}$ of e$^-$ of the ionization track. The total number n_{final} of e$^-$ collected after avalanche is proportional to the initial number $n_{initial}$ of e^- and the proportionality factor is called the gain, i.e. $n_{final} = Gain \times n_{initial}$ (section 2.1.1). Gain depends of various "physical" factors that can vary during time, see below. The initial kinetic energy measurement is done by integrating the anode signal. The calibration factor is defined as the proportionality between T_e and the integration of the anode signal. The latter is proportional to the total number n_{final} of collected e$^-$, but the corresponding proportionality factor depends only of analogical and digital signal processing, and can then be considered as constant along time. Calibration factor ("global") is thus proportional to gain ("global"), i.e $Calibration(t) \propto Gain(t)$. "Local" calibration factor is also proportional to "local" gain, i.e. $Calibration(\overrightarrow{x},t) \propto Gain(\overrightarrow{x},t)$.

To compute the gain, we must integrate the amplification and attachment processes (see section 2.1.1) along drift path, i.e determine how much n_{final} e^- will be produced by $n_{initial}$ e^-. We have:

$$dn = [\alpha(x) - \eta(x)]n(x)dx \tag{2.2}$$

$\alpha(x) \equiv$ ionization probability per unit length
$\eta(x) \equiv$ attachment probability per unit length

We obtain then, with $Gain \equiv \frac{n_{final}}{n_{initial}}$:

$$Gain = \exp\left(\int_{x_{initial}}^{x_{final}} [\alpha(x) - \eta(x)]dx\right) \tag{2.3}$$

From equation 2.3 we can deduce that ionization and attachment probabilities per unit length are equal to the inverse of the mean free path λ relative respectively to ionization and attachment processes, i.e:

$$\alpha(x) = [\lambda_{ionization}(x)]^{-1} \tag{2.4}$$

$$\eta(x) = [\lambda_{attachment}(x)]^{-1} \tag{2.5}$$

Thus:

$$\alpha(x) = N\sigma_{ionization}(x) \tag{2.6}$$

$$\eta(x) = N\sigma_{attachment}(x) \tag{2.7}$$

$N \equiv$ number of CF_4 atoms per volume unit
$\sigma \equiv$ cross section (relative to ionization and attachment processes)

We can "admit" that ionization cross section is proportional to the energy $\epsilon(x)$ of the incident e^-, i.e.:

$$\sigma_{ionization}(x) = k\epsilon(x) \tag{2.8}$$

Attachment cross section is a more complicated function of $\epsilon(x)$, because it is "small" for "small" $\epsilon(x)$ (this is the case in drift zone), becomes more important for a little higher $\epsilon(x)$ (attachment zone, "between" drift zone and amplification zone), and becomes smaller again for still higher $\epsilon(x)$ (amplification zone). We treat only the case of the ionization coefficient and "admit" that attachment coefficient depends on the same variables, in the "same way" (see below).

During one mean free path $\lambda_{ionization}(x)$ the incident e^- will get the mean energy $\epsilon(x)$ (we suppose the variation of electrical field $E(x)$ during one mean free path to be "slow"):

$$\epsilon(x) = E(x)\lambda_{ionization}(x) \tag{2.9}$$

Putting equation 2.4 into equation 2.9, we obtain:

$$\epsilon(x) = E(x)[\alpha_(x)]^{-1} \tag{2.10}$$

Putting equation 2.8 into equation 2.6, we obtain:

$$\alpha(x) = kN\epsilon(x) \tag{2.11}$$

Finally, putting equation 2.10 into equation 2.11, we get:

$$\alpha(x) = [kNE(x)]^{\frac{1}{2}} \tag{2.12}$$

We see that the reduced ionization coefficient $\frac{\alpha(x)}{N}$ is function of $\frac{E(x)}{N}$, i.e. $\frac{\alpha(x)}{N} = \frac{\alpha}{N}(\frac{E}{N})$. We "admit" that it is the same for the reduced attachment coefficient $\frac{\eta(x)}{N}$ i.e. $\frac{\eta(x)}{N} = \frac{\eta}{N}(\frac{E}{N})$.

From gain expression (equation 2.3) and results obtained for α and η, we see that the value of gain ("global" or "local") is related principally to the following factors:

- "integration path"
  (correspondence with gain variations in space: for example gain is a little lower for e^- events far from anode that for e^- events close to the latter, due to the recombination during drift path)
- "type" of the gas, presence of gaseous contaminants
  (possible correspondence with gain variations along time: a strong increasing of the gain had been observed in correlation to a leak of scintillator oil and was probably due to gaseous pseudocumene emitted by the latter and "contaminating" CF_4)
- electrical field E(x), i.e. geometry and intensity of the latter
  (possible correspondence with the gain variations in time: a diminution of gain had been observed just after having replaced the anode and can be explained by the modification of the electrical field around anode wires due to "aging" of the latter, i.e. oxidation by CF_4; correspondence with the variations of the "local" gain in space: in our case a small spatial gain variation has been observed on XY plane and can be explained by a spatial variation of the electrical field due to a slight inclination of the anode plane)

- number of atoms per volume unit N
  (possible correspondence with the gain variations in time: "seasonal" variation of gain are observed and can be explained by variations of N due to temperature variations while TPC CF_4 pressure is always maintained at the same value)

We see that many factors can cause gain variations. A "continuous" gain monitoring is thus required. A "precise" calibration is realized each week with a γ source introduced close to the TPC trough the anti-Compton, see section 2.1.2.

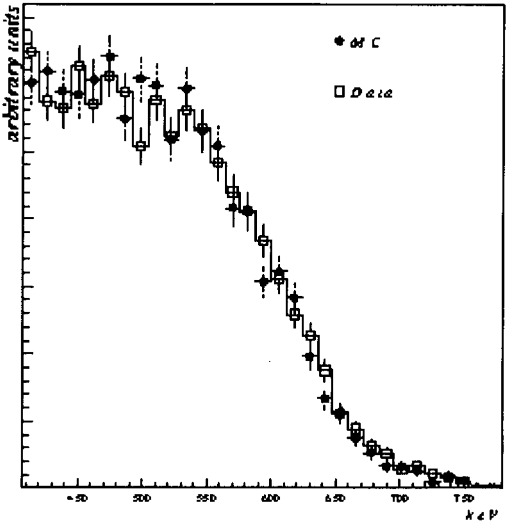

Figure 2.24: Calibration of the TPC with ^{54}Mn source emitting 835 keV γ, measuring the kinetic energy of the e^- resulting from Compton scattering (the activity of the source is 3 kBq, so about 99 % of the observed events corresponds to Compton scattering with emitted γ). The maximal kinetic energy of the recoil e^- is equal to $\frac{2E_e^2}{2E_e+m_e}$ (forward scattering), i.e. 640 keV. The corresponding Compton front is "vertical" for a total resolution equal to 0 and become "inclined" with the "decreasing" of resolution. A good fit of the experimental spectra (black circles; energy measurements are done here from the integration of the anode signal, but an almost identical spectra is obtained from the integration of the avalanche scintillation light measured with PMTs) is realized with simulation data for an "entered" value of 8 % for the total resolution (white squares). The latter depends on various factors, see 2.3.2.

γ sources are thus well adapted for TPC calibration, but useful "complementary" calibrations can be realized with μ:

- measurement of the drift velocity
  (it is necessary to "scale" the TPC along Z axis; measurement of the drift velocity can also be realized with α or Compton e^-)
- "supplementary" ("global") calibrations, "between" calibrations with sources
  (μ calibrations can be realized "continuously", and can be controlled "from far")
- local calibration of the energy, in function of XY
  (i.e. "mapping" determination; mapping is useful to correct energy measurement in function of the localization of the XY projection of the event)
- local calibration of the energy, in function of Z
  (i.e. "attenuation" measurement; it is useful to determine the uncertainty due to the attenuation and to see the possible fluctuations of the latter)

The first step of μ calibrations, i.e. get the 3D absolute μ track coordinates (which is done with a fit of μ track), is explained in section 2.3. μ tracks coordinates have to be expressed in a "physical" scale. "Scaling" is described in section 2.2.2. It needs the determination of v_{drift} value. The latter can vary, so it has to be determined just before doing μ calibrations. It is possible to determine v_{drift} with α, Compton e^- or μ. The method used here to determine v_{drift} from μ is described in figure 2.25. The results obtained with other methods are identical.

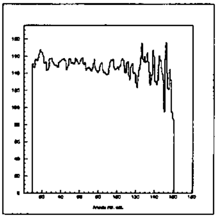

Figure 2.25: A large number of μ of any "inclination" (i.e. "horizontal", "vertical", etc.) are fitted (only μ with "good" fits are kept, see figure 2.22). With a "large" number of μ it is "certain" that every (absolute) detector Z coordinate was "occupied" at least once by a μ track. This figure corresponds to such a case. The horizontal axis corresponds to "bins" of anode signal with a definite drift time, i.e. to Z axis. Each "bin" a value different from zero was "occupied" at least once by a μ, so the extension of the corresponding zone is equal to the extension of detector drift zone along Z, i.e. 162 cm (in this figure the value of each bin is equal to the mean of the different values of μ anode signal divided by the length "contained" in that bin; the values of bins are calculated in such a way for the determination of the attenuation, see figure 2.28). Each bin with a value different from zero represents thus a "physical" extension equal to $T_{sampling}v_{drift}$. $N_{bin\neq 0} \equiv$ number of bins with value $\neq 0 \Rightarrow v_{drift} = 162(N_{bin\neq 0}T_{sampling})^{-1}$.

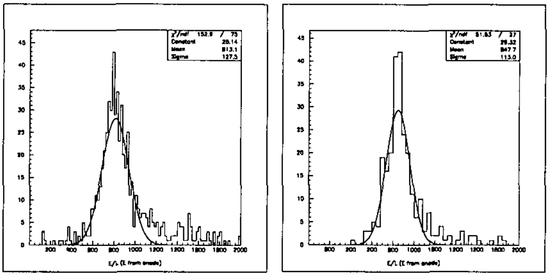

Figure 2.26: Distribution spectra of the mean μ energy loss (in "anode units") per length unit. μ tracks length Δx, μ energy loss along tracks ΔT_μ in "anode units", i.e. with a calibration factor equal to 1, obtained by the integration of anode signal corresponding to that length, and the value $\Delta T_\mu \Delta x^{-1}$ (i.e the mean μ energy loss in "anode units" per length unit) are computed for every μ whose fit is "good" from the 3D absolute μ track coordinates of μ in a "scaled" referential (v_{drift} is used for the scaling of Z). We see the high number of μ with a low loss of energy per length unit, corresponding to "minimum" ionizing μ (there are more minimum ionizing μ than other μ crossing the TPC, see section 2.3 and "good" fit criteria will also select preferentially the latter). The distribution spectra is fitted with a Gaussian curve to determine the mean energy loss in "anode units" per length unit of minimum ionizing μ ($\Delta T_\mu \Delta x^{-1}$ at the maximum of the Gaussian). The two spectra were realized at different periods, with a few thousands of μ, and the values obtained for the mean energy loss in "anode unit" per length unit of minimum ionizing μ are different. The variation should be strongly correlated to the fluctuations of the gain. "Local" calibrations are realized by selecting μ whose value of $\Delta T_\mu \Delta x^{-1}$ vary of σ around $\Delta T_\mu \Delta x^{-1}$ of minimum ionizing μ.

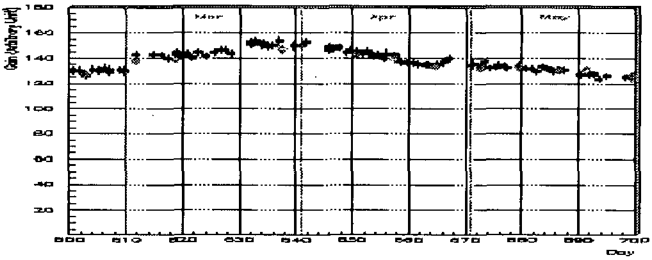

Figure 2.27: Weekly calibration with ^{54}Mn (light marks) and daily calibration with μ (dark marks) from J. Lamblin program, on a period of 3 months. The good correlation between measurements with ^{54}Mn and μ shows that the latter can be used for daily calibrations.

2.3.2 "Local" calibration with μ

The TPC is working in a proportional domain (the electric field configuration around the multiplication wires, i.e. anode wires, defined by the potential settings on cathode, anode wires, etc., is chosen in function of the pressure of CF_4 following various criteria, including proportionality), which means that the gain (and thus the calibration factor between the integration of anode signal and energy) is not dependant of the energy left by the e^- along its track. However the gain can depend (this should not be the case in an "ideal" TPC) on the spatial position of the initial e^-, i.e. the position of the track before drifting (which means that the "global" gain observed for a track corresponds to the integration of the "local" gain along this track, i.e. $gain = \int_{track} gain(\vec{r})dr$). The energy resolution is affected by the spatial dependance of the gain when the latter is not included into energy computation (energy resolution is measured from a large number of events, and the "apparent" energy vary with the spatial position of the event when the spatial dependance of the gain is not taken into account).
The resolution R is defined in the "usual" way:

$$R \equiv \frac{\Delta(E)}{E} \tag{2.13}$$

With:

$$\Delta \equiv FWHM;\ \sigma(x) \equiv (\Sigma(x_i - \bar{x})^2)^{\frac{1}{2}} \Rightarrow \Delta = 2.35\sigma \tag{2.14}$$

When we can separate measure in different processes, each affecting the latter in an independent way, we have:

$$\sigma^2 = \Sigma\sigma_i^2 \Rightarrow \Delta^2 = \Sigma\Delta_i^2 \tag{2.15}$$

In the TPC we may distinguish different "contributions" of the resolution:

$$(\Delta(E))^2 = (\Delta_{ionization}(E))^2 + (\Delta_{gain}(E))^2 + (\Delta_{parallel\ currents}(E))^2 + (\Delta_{electromagnetic}(E))^2 \tag{2.16}$$

The "ionization" term of equation 2.16 corresponds to the fluctuation on the number N of e^- belonging to the track (coming from CF_4 ionization by the initial e^-). The initial e^- loses the quantity of energy $w_{ionization}$ at each ionization, so we have approximatively:

$$N = \frac{E}{w_{ionization}} \tag{2.17}$$

We can show that:

$$(\sigma_{ionization}(N))^2 = FN \tag{2.18}$$

in our case $0 < F < 1$ ($F = 1$ in the case of a perfect Gaussian distribution)
As the TPC is working in the proportional mode, we have:

$$\frac{\sigma_{ionization}(E)}{E} = \frac{\sigma(N)}{N} \tag{2.19}$$

From equations 2.14, 2.17, 2.18 and 2.19, we find:

$$\Delta_{ionization}(E) = 2.35(w_{ionization}FE)^{\frac{1}{2}} \tag{2.20}$$

The "gain" term of equation 2.16 may be decomposed in the following way:

$$(\Delta_{gain}(E))^2 = (\Delta_{multiplication}(E))^2 + (\Delta_{spatial}(E))^2 \qquad (2.21)$$

Both right terms of equation 2.21 can be decomposed in their turn. The "multiplication" term of equation 2.21 can be decomposed in the following way:

$$(\Delta_{multiplication}(E))^2 = (\Delta_{attachment}(E))^2 + (\Delta_{amplification}(E))^2 \qquad (2.22)$$

$\Delta_{ionization}(E)$ follows a $E^{0.7}$ law, rather than the $E^{\frac{1}{2}}$ law of equation 2.20 when we take into account multiplication processes (i.e. attachment, which occurs "just before" amplification and where almost 98% of the drifting e$^-$ are lost, and amplification, whose "contribution" to the energy resolution is less important than attachment "contribution") in simulations. This result has been verified experimentally.

The "spatial" term of equation 2.21 corresponds to the spatial dependance of the gain. It can be decomposed in the following way:

$$(\Delta_{spatial}(E))^2 = (\Delta_{XY}(E))^2 + (\Delta_Z(E))^2 \qquad (2.23)$$

The "XY" term of equation 2.23 corresponds to the spatial dependance of the gain in relation with the projection of the track on the XY plane (drift is perpendicular to detection planes), see figures 2.30 to 2.34. This dependance can be due for example to a non perfect parallelism between anode and XY plane or grid, causing an inhomogeneous electric field configuration around anode wires. An XY dependance of gain has been observed. At 640 keV, the total energy resolution is about 8 %, and the energy resolution "part" corresponding to XY gain variation is estimated to be of about 1.5 % (when a "global" gain is used for energy computation). However an XY "mapping" has been realized (XY mapping can be realized with α or μ), and XY gain variations are taken into account for energy computation from integration of anode signal (relative to avalanche electronic induction) or PMTs signal (relative to avalanche scintillation light). The "Z" term of equation 2.23 corresponds to the spatial dependance of the gain in relation with the Z position of the e^- track before drifting, see figures 2.28 and 2.29. The Z dependance of the gain is due to the recombination of the drifting e^- occurring during the drift. The gain is thus smaller for an initial e^- track far from anode than for an initial e^- track near of the latter (this is different for α, see section 2.1.2). The energy resolution "part" corresponding to Z gain variations is of the same order than the XY part. A correction is not possible for the e^- events relative to $\bar{\nu}_e e^-$ scattering or β decay, because for such events we don't have the information on the time of occurrence, i.e. on the Z absolute position. However the Z dependance of the gain is an important information concerning the quality of the gas. An "attenuation" length can be related to the Z dependance of the gain. With $\bar{z} \equiv$ distance measured from cathode, and $\lambda \equiv$ attenuation length, we obtain:

$$gain(\bar{z}) = gain(0)\exp(-\frac{\bar{z}}{\lambda}) \qquad (2.24)$$

The "parallel currents" term of equation 2.16 is described in section 3.4.2. Measurements on resolution and gain give the same results from anode and PMTs signals so electromagnetical noise (last term of equation 2.16) is probably "not important".

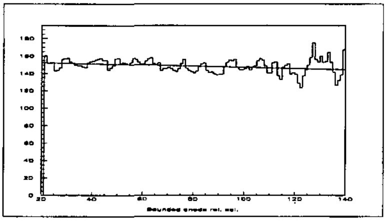

Figure 2.28: Determination of Z gain dependance with μ (i.e. measure of attenuation length). Minimum ionizing μ within 1 σ of energy in "anode units" per unit length $\Delta T_\mu \Delta x^{-1}$ are selected for calibrations, see figure 2.26. A stronger restriction on energy value would improve attenuation measure, but the number of μ accepted by the program is then reduced, so we need to "acquire" a larger number of μ with detector, which takes more time (here about 3000 μ were "acquired" corresponding to about 6 hours of acquisition time). The 3D absolute track coordinates have been determined for every μ in a "scaled" referential (see sections 2.2.2 and 2.3). Each bin of anode signal ("new" anode signal, with lower resolution, whose bins values are defined as the mean on 4 bins of anode signal, see figure 2.19) corresponding to a "fraction" of a μ can thus be associated to a Z coordinate which are represented on the horizontal axis of this figure. The value of each bin of anode signal "crossed" by a μ is proportional to the energy left by the μ "inside" that bin (which can be seen as a slice of the cylindrical TPC) by the mean of a constant multiplying the Z dependant local gain. Even if all minimum ionizing selected μ would have exactly the same energy loss per unit length, the energy left "inside" a bin "crossed" by a μ would change in function of μ "inclination". Vertical μ, i.e. perpendicular to Z axis, cross anode bins (only 1 bin is crossed for a perfectly vertical μ, on a distance equal to the length of the track) on a much larger distance than horizontal μ, i.e. parallel to Z axis (all bin are crossed for a perfectly horizontal μ, on a length equal to the wide of the slice). The energy left by a μ inside a "slice" corresponding to 1 bin is thus proportional to the track length contained in that "slice". This fraction of track length is equal to the total track length divided by the number of bins "crossed". The value of the energy left by a minimum ionizing μ (with a well defined energy loss per unit length) "inside" a bin divided by the fraction of the track length "contained" in that bin is thus the same for every μ (i.e. independent of their inclination) and corresponds to the energy loss per unit length. "Energy loss" per unit length of "crossed" bins is "summed" in corresponding bins for every μ, taking the value of the anode bin as "energy loss". The number of times each bin is "crossed" by a μ is counted. The mean of the "energy loss" per unit length is then computed (after having "processed" all μ) for every bin. The value of the mean "energy loss" per unit length "seen" by bins along Z is proportional to Z local gain value, which is, as expected, higher near anode than near cathode. The stronger fluctuations on cathode side corresponds probably to a low statistic due to a high radioactive noise on this side, reducing the number of μ fitted. The attenuation length measured here is of about 16 m, which is in agreement with 27^{+160}_{-12} found from Compton e^-. 16 m corresponds to an attenuation of about 10 % (= exp(−1.6/16)) on 1.6 m TPC length and "contributes" to a part of the same order than XY gain variations of the total resolution.

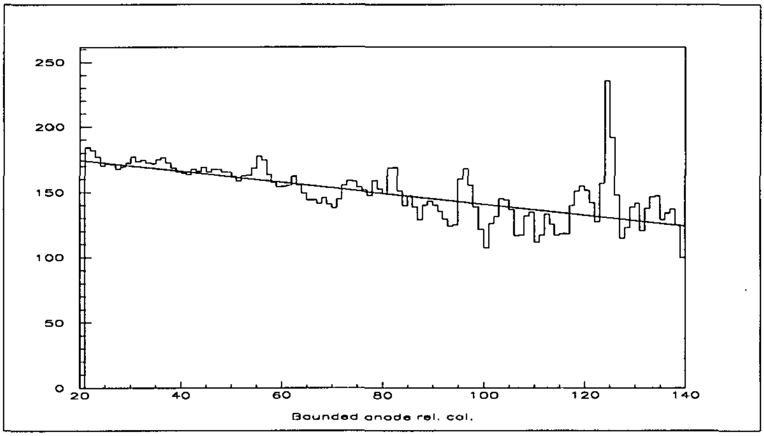

Figure 2.29: After having replaced the cathode, an infiltration of scintillator oil occurred in the TPC. It was due to the break of nylon crews on a tube for connecting the TPC and the CF_4 circulation system. The Scintillator oil contains pseudocumene, which is gaseous at ambient temperature. We observe here the very strong attenuation (corresponding to a short attenuation length) measured during that period. It is probably due to a high pseudocumene concentration inside of the gas. A strong gain was observed during the same period, also probably due to the presence of pseudocumene. This strong gain is probably the source of the break of an anode wire. All anode wires were then changed at Neuchâtel (the "new" anode plane was tested in a TPC, see Chapter 3). The TPC, the anti-Compton and the detection planes were cleaned with Hexane, and the "deficient" crews were replaced with metallic ones. The leak of oil has not reappeared since. The gain and the attenuation have "returned" to "normal" values.

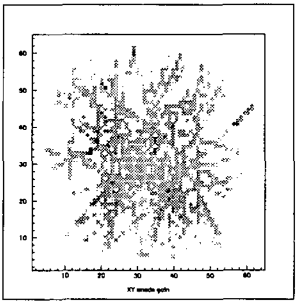

Figure 2.30: Measurement of the XY local gain ("mapping"), done in the same way than measurement of the Z local gain ("attenuation"), see figure 2.28. The value of the "energy loss" in anode units per unit length calculated in each "crossed slice" perpendicular to Z (as it was before; "too" vertical μ are eliminated) can be associated to the value of each XY "square" (4×4 XY "pixel", see figure 2.19) "touched" by the track in the "slice". The number of times each "square" is touched is counted. The mean of the energy loss is then computed for every XY "square" (after having "processed" all μ), giving thus an XY local gain "mapping". This is true only for a very large number of μ, i.e. when each XY "square" is touched a sufficient number of times (even when it is not the case we can do mapping with lower resolution, see figure 2.32, which means with larger "squares" containing "some" squares, affecting to each "large" square the value of the mean of included squares, omitting squares with 0 value) to reduce the uncertainty due to Z attenuation. On this figure the number of μ is very low, and we can distinguish the projection of the μ tracks on the XY plane.

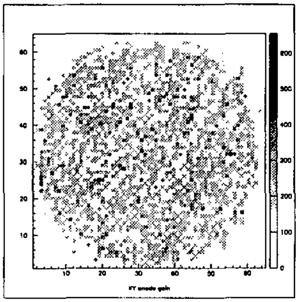

Figure 2.31: "Mapping" with a higher number of μ. The "circle" of 90 "cm" of diameter corresponds to the XY plane. The gain seems rather "homogeneous".

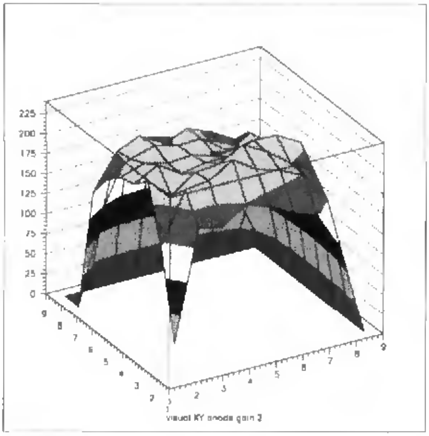

Figure 2.32: Mapping realized with μ, with a "low" resolution, see figure 2.30. This mapping seems "rather" in agreement with that of figure 2.33, realized with α. An "improvement" of XY mapping would need a still higher number of μ (and thus more μ "acquisition" time).

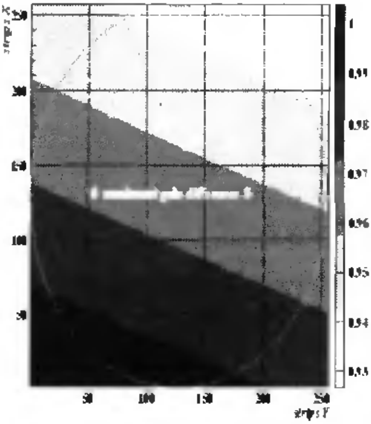

Figure 2.33: XY mapping realized with 5.31 MeV α emitted from ^{210}Po contaminating cathode, see section 2.1.2 and figures 2.14 and 2.16. This mapping is more accurate than the one realize with μ. The maximum gain variation is of about 5 to 7 % and corresponds to a "part" of about 1.5 % of the 8 % of the total resolution at 640 keV.

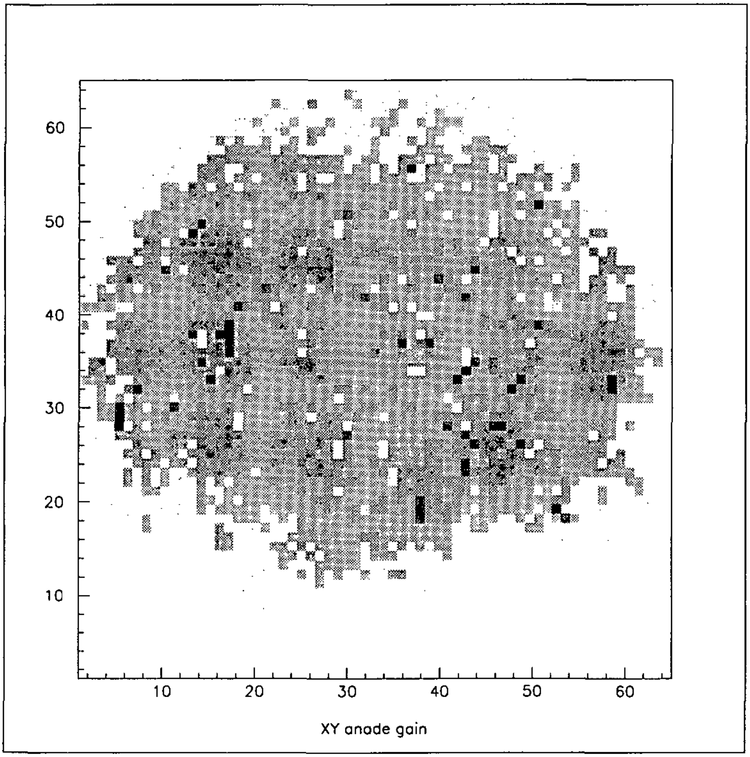

Figure 2.34: This XY mapping with μ has been realized just before the break of an anode wire (probably related to the presence of pseudocumene in CF_4, see figure 2.29). The detection planes were then removed to change all anode wires and a strong "mark" has been observed on the "old" XY plane (this "mark" was then cleaned with Hexane), probably due to the scintillator oil (the bottom of the TPC was "immersed" by scintillator oil after leakage). The position of the mark and its form and dimensions ("broken croissant" whose extremity reach almost the half of detection planed, and whose wide is equal to 12 cm at maximum) correspond to the zone with a very low gain.

2.3.3 Electric field configuration in the TPC

Some simulations of the electric field inside of the TPC that I have realized with Garfield [31] version 5.37 (continuation of A. Tadsen's work) are presented here. The electric field configuration is essential for events' observation and acts on various parameter, such as:

- amplification and proportionality
  (electric field acts on "global" gain; the field around anode wires must be high enough to get a sufficient gain, but not too high to avoid discharges or loss of proportionality corresponding to a dependance of the gain on the energy loss)
- energy resolution
  (electric field acts on "local" gain; a spatial inhomogeneity of the electric field configuration on the anode plane affects the energy resolution)
- angular resolution
  (the drift field "brings" the track to the detection planes; a constant drift field is necessary to avoid tracks' deformations and thus a loss of the angular resolution; the deformations can be well identify through the observation of "curvatures" on μ tracks, because the initial μ tracks correspond in general to "straight lines"; field shaping rings are required to maintain a constant drift field, i.e. "flat" equipotential, because the TPC "planes" are not infinite, see figure 2.37)
- e^- "focusing" on anode wires
  (the electric field defined by the detection planes' wires act like as set of lenses focusing the drifting e^- and avalanches e^- on the anode wires, see figure 2.35)
- strains on anode wires and discharges
  (the symmetry of the electric field around the anode wires is necessary to minimize the strengths on the latter, and thus sagging and strains which are strongly correlated to the occurrence of discharges and of anode wire break, see figure 2.36)

Some "rules" concerning the potentials applied to the different "elements" of the TPC are used to compute the potential settings at various pressures:

- reduced drift field $\frac{E}{P} \sim 75\ Vcm^{-1}bar^{-1}$
- rapport between anode wires and grid wires potentials $\frac{V_A}{V_G} \sim$ -1.75
- rapport between anode wires and potential wires potentials $\frac{V_A}{V_P} \sim 10$
- adjust grid wires and potential wires potentials to get a symmetric electric field configuration around the anode wires, see figure 2.36
- put the potential value of the field shaping ring 1 at the value, calculated in the infinite case, thus without field shaping rings, of the equipotential at the Z position corresponding to the field shaping ring 1, see figure 2.37

Figures 2.35 to 2.37 describe an "optimum" electric field configuration inside of the TPC, for 3 bar of CF_4 (corresponding to TPC settings since July 2001). The Z positions from the XY plane and the potentials of the different elements defining the electric field inside of the TPC are the followings ($\emptyset \equiv$ wires diameter, $\Delta d \equiv$ distance between 2 wires):

- XY plane $\Leftrightarrow$ Z_{XY} = 0 cm, V_{XY} = 0 V
- Cathode plane $\Leftrightarrow$ Z_C = 163.9 cm, V_C = -37 kV
- Anode wires $\Leftrightarrow$ $\emptyset_A$ = 20 μm, Δd_A = 4.95 mm, Z_A = 3.5 mm, V_A = 3540 V
- Potential wires $\Leftrightarrow$ $\emptyset_P$ = 100 μm, Δd_P = 4.95 mm, Z_P = 3.5 mm, V_P = 386 V
- Grid wires $\Leftrightarrow$ $\emptyset_G$ = 100 μm, Δd_G = 4.95 mm, Z_G = 12.0 mm, V_G = -2004 V
- Field shaping rings n, with n $\in$ [1,133], situated outside acrylic TPC $\Leftrightarrow$
  $\emptyset_n$ = 1 mm, Z_n = 52.8 mm + (n-1)12.0 mm, V_n = -2315 V - (n-1)262.4 V

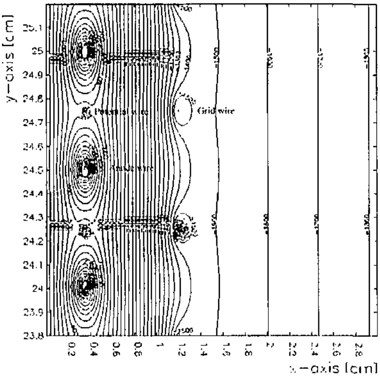

Figure 2.35: Potential configuration inside of the TPC. The lines of this figure represent equipotentials. The difference of potential between 2 consecutive lines is equal to 100 V. $E = \nabla V \Rightarrow$ perpendicularity between electric field and equipotentials. $F = qE \Rightarrow$ displacement of e^- in the direction opposite to electric field. The grid potential "imposes" a clear separation between the drift zone (on right; cathode not on figure) and the "amplification" zone (delimited on left by the XY plane). Curve equipotentials situated close to the grid in drift zone (the curvature is due to the partial transparency of the grid to the electric field) and around anode the anode wires act like lenses focusing e^- on the anode wires. The grid wires are perpendicular to the anode wires, but only parallel wires can be simulated with 2D Garfield. We can however "imagine" that equipotentials "going out" of the grid form a "pavement" of "square" lenses focusing e^- on the anode wires.

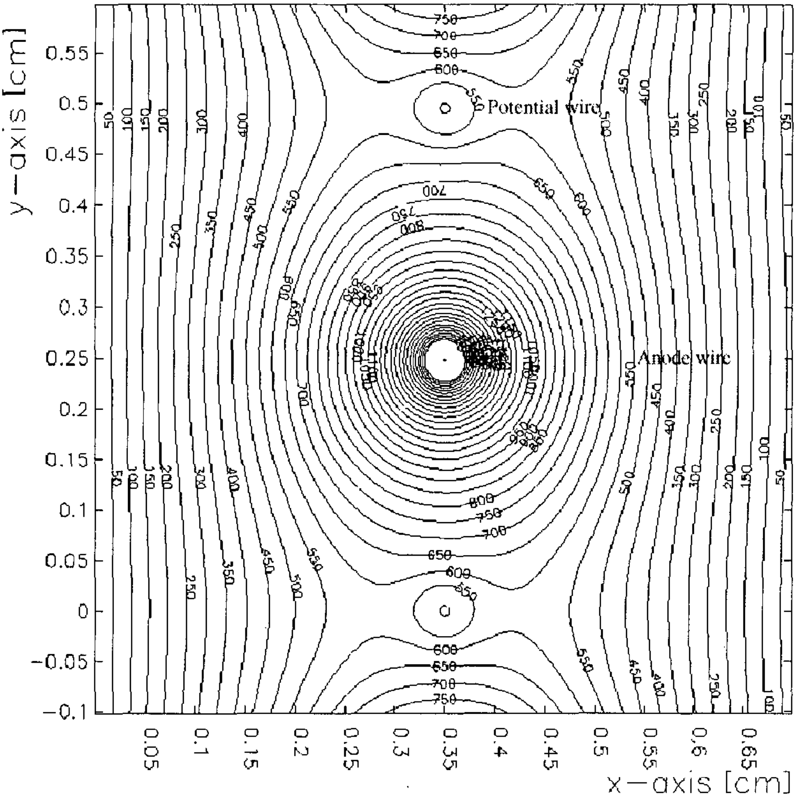

Figure 2.36: Symmetry of the potential configuration around the anode wires. The intensity of the electric field doesn't vary on the anode wire surface and its orientation is perpendicular to the latter, so no forces act on the anode wires (in unsymmetrical configurations strengths are presents and cause anode wires displacements which increase the probabilities of discharges and thus of anode break). The conservation of the electric field flux trough the surfaces enclosing the anode wires "explain" the "strong" electric field (corresponding to a "strong" potential variation and thus to "close" consecutive equipotential) near the "thin" anode wires.

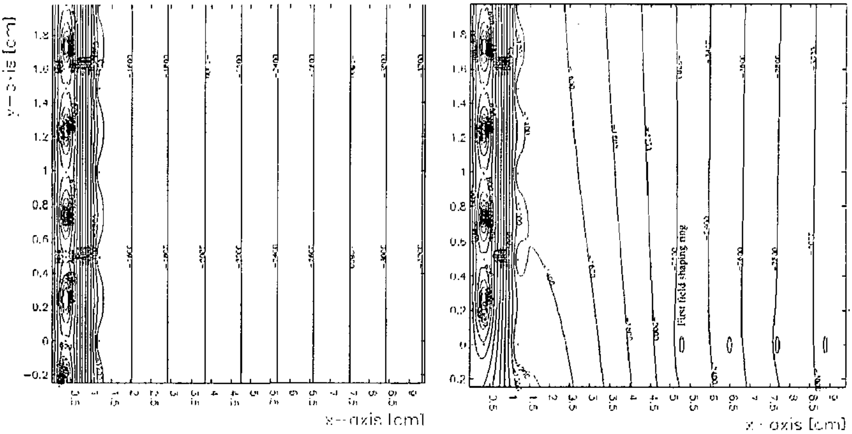

Figure 2.37: "Infinite" configuration without field shaping rings (figure on left; cathode, XY plane and wires planes are infinite) and finite configuration with field shaping rings (figure on right). In the finite case (i.e. in the TPC) equipotentials have to be "closed", which causes a deformation of the drift equipotentials in the edge of the TPC. Field shaping rings (equidistant and situated at the exterior of the TPC) whose potential is set the value of equipotential situated at their corresponding height in the infinite case (which is done by the mean of a variable resistance connecting field shaping ring 1 to "ground" and all field shaping rings together by resistances of 10 MΩ to the anode) are necessary to "sustain" the drift equipotentials. The acrylic of the TPC can be omitted in the simulations because the tangential component of E is continuous across interfaces (flat equipotentials ⇒ E tangent to acrylic). The values of the potential on the field shaping rings were obtain following this method and a modification of the value of the resistance connecting field shaping ring 1 to ground was necessary to set field shaping rings at these values. μ tracks "acquired" before modification are "curved" and μ tracks "acquired" after modification are "straight".

2.4 First results

2.4.1 Principle of μ_ν measure

The "principle" used to "calculate" μ_ν from the recoil e^- energy spectra "measured" (obtained by kinematic or non kinematic, see section 2.4.2, online background rejection corrected by the background asymmetry, see section 2.2.2, with or without kinematic "cut" and with eventual "hot" sources suppression by angular "cut") is briefly exposed below. It is based on the χ^2 minimization method and consists thus to find the most probable value of μ_ν giving a recoil e^- spectra "compatible" with the spectra measured. For a recoil e^- energy spectra of N "bins", with, for each bin, a "measured" count rate n_{mes}, an "expected" count rate in function of μ_ν value $n_{exp,\,\mu_\nu}$ and an error estimation σ on $n_{exp,\,\mu_\nu}$, we have:

$$\chi^2 = \sum_{i=1}^{N} \left(\frac{n_{exp,\,\mu_\nu}(i) - n_{mes}(i)}{\sigma(i)} \right)^2 \tag{2.25}$$

It is possible to show that to minimize χ^2 corresponds to minimize the following function:

$$\kappa^2(\alpha, \mu_\nu^2) = \tag{2.26}$$

$$-2\ln\left[\frac{1}{\sigma_\alpha(2\pi)^{\frac{1}{2}}}\exp\left(-\frac{(\alpha-1)^2}{2\sigma_\alpha^2}\right)\prod_{i=1}^{N}\frac{1}{\sigma(i)(2\pi)^{\frac{1}{2}}}\exp\left(-\frac{(\alpha(w(i)+\mu_\nu^2\varepsilon m(i)) - n_{mes}(i))^2}{2\sigma^2(i)}\right)\right]$$

$\alpha \equiv$ normalization factor between the expected total number of events, which depends on μ_ν value, and the measured total number of events

w $\equiv$ expected count rate corresponding to a pure weak interaction

m $\equiv$ expected count rate corresponding to an electromagnetic interaction, see section 1.1

2.4.2 Preliminary results and conclusion

Before replacing the cathode, the noise resulting from the contamination of the latter and gas by the radon emitted by OXYSORB was too "high" to give "competitive" results concerning μ_ν. Some "interesting" μ_ν limits (found using angular and energetic "restrictions", and applying kinematics) obtained in that period $\equiv$ period I are however given below. There was an OFF period some time after having replaced the cathode but just when the reactor was ON again, an anode wire break occurred, due to a leak of the scintillator oil. The detector was then opened to change the anode wires and was also fully cleaned. The "noise" conditions inside of the TPC have thus certainly been modified, so the OFF period following cathode change can't be "exploited" for the ON period following the change of the anode wires. Moreover, it is almost impossible to utilize the ON and OFF data of the period $\equiv$ period II following the change of cathode and preceding the change of the anode wires, because of the strong gain variations due to the leak of scintillator oil, even if "strong" reductions of the contamination of cathode (by changing the cathode) and of the contamination of the gas (by changing gas and replacing OXYSORB by a SAES filter) were obtained. We are thus expecting a new OFF "interval", which should occur in October 2001. We are "now" still in the ON "interval" of the period $\equiv$ period III following the change of the anode wires and we would be very happy if the detector would be working until the end of the next OFF "interval"! For the moment we can suppose that the background is homogeneous. Analysis performed with "automatic scanning" at Grenoble and with "manual scanning" at Neuchâtel are actually in curse. Some comments are given below, but it is too early to give "limits" concerning μ_ν for period III.

Period I recoil e^- energy spectra was obtained in the following way (other spectra have been obtained, without applying angular cut or without kinematic restriction concerning online background rejection, see below, but even if the total count rate measured was "compatible" with the expected count rate, the spectra has shown a "non coherence" of these results due to a too large acceptance to the background coming from the cathode or the gas, presenting for example an excess of events in the "wrong" direction, i.e. oriented from reactor to detector, at some energy value; such an an analysis wouldn't have been possible with an "integral" detector):

- energy "cut", keeping "only" e^- from 800 keV to 1800 keV
  (lowest energy limit for e^- acquisition = 300 keV)

- angular "cut", rejecting events coming from cathode
  (i.e. rejecting e^- whose initial angle belongs to the half sphere oriented from cathode to anode)

- kinematic online background rejection
  online background rejection without kinematic restriction is described in section 2.2.2. It corresponds to do the substraction at each energy of the count rate of "backward" $\bar{\nu}_e e^-$ "like" events from the count rate of "forward" $\bar{\nu}_e e^-$ "like" events. e^- initial angle is contained in the half sphere oriented from reactor to detector for "forward" events and in the half sphere oriented in the opposite direction for "backward" events. These half spheres can be considered as cones with an opening angle independent of the energy (opening angle $= \pi$). With the kinematic of $\bar{\nu}_e e^-$ scattering it is possible to do an energy dependant restriction on "forward" cone opening angles. We can then subtract, at "each" energy, the count rate of backward cone from the count rate of corresponding (i.e. with the same opening angle) forward cone, considering that background is symmetric around TPC Z axis (anode $\rightarrow$ cathode), to obtain the recoil e^- energy spectra. From the formula 1.1, obtained from $\bar{\nu}_e e^-$scattering kinematics, we see that the maximal recoil e^- scattering angle possible, corresponding thus to the half opening of the cone, in function of energy, is given by:

$$\theta_e = \cos^{-1}\left(\frac{T_e}{T_e + 2m_e}\right)^{\frac{1}{2}} \tag{2.27}$$

It is not possible to determine the background asymmetry in function of the recoil energy of the e^- from the OFF "interval" with both angular cut and kinematic restriction because the corresponding number of "accepted" event is too low. Moreover the incertitude concerning the calibration factor during the OFF "interval" is important (during that period calibrations has only been "occasional" because gain variations were still "underestimate" and there wasn't yet μ calibrations). An estimation of the daily total (i.e. not in function of the energy of the recoil e^-) count rate during the OFF period, with an angular cut to reject the events coming from the cathode, give -0.12 ± 4.75 count. This is compatible with an homogeneous distribution but the incertitude is "high".

The inefficiency on kinematic online rejection is associated to the limitations on the angular resolution. It seems however that the kinematic online rejection is the best way to obtain a recoil e^- energy spectra concerning $\bar{\nu}_e e^-$scattering, because of its efficiency for background rejection. Supposing the background homogeneous around TPC Z axis, which is not "demonstrated", the spectra obtained with kinematic online rejection is compatible with that of the standard model, but with an "important" statistical uncertainty. From this spectra we obtained, for 2 different confident levels, the following results concerning μ_ν :

$$\mu_\nu \leq 1.97\ 10^{-10}\ \mu_b\ (68\ \%\ \text{C.L.})$$

$$\mu_\nu \leq 2.66\ 10^{-10}\ \mu_b\ (90\ \%\ \text{C.L.})$$

Period III is actually still both on acquisition "phase" and on analysis "phase", and the OFF "interval" is expected, see above. Tests concerning automatic scanning, the choice of the cuts that have to be applied (like the "scirise" cut to reject the events coming from the anode, see for example figure 2.16), the way to apply them and their efficiencies are actually performed at Grenoble. A spectra of the energy distribution of the recoil e^- showing a "precise" structure hasn't been obtained yet. Applying successive cuts the following count rate values were observed above 300 keV (these values are not definitive):

cuts	rates
$T_e \geq 300$ keV	70 s^{-1}
no μ veto	0.35 s^{-1}
contained in the fiducial volume	0.15 s^{-1}
no anti-Compton veto	778 day^{-1}
forward cone of $\pi/4$ opening angle	97 day^{-1}

Manual tracking is performed at Neuchâtel above 700 keV, from events filtered with scirise cut at Grenoble, and rejecting events whose angular distribution corresponds to the half-sphere oriented from the anode to the cathode, because the background on the anode is higher than on the cathode since the "old" cathode has been replaced by a "new" one, and seems also to have increased a little since the change of the anode wires (or since the "last" change, because a few time after anode wires change an anode wire break occurred again, which was maybe due to an insufficient tension of the latter; the detector was opened and cleaned again while the wire was replaced in the local of the detector). In the "present" situation, about 3 $\bar{\nu}_e e^-$ scattering events are observed each day (see figure 2.38), using the online background rejection, which is more than the 1.5 events expected (supposing that the total background is homogeneous above 700 keV, which has to be verified with the observation of the next OFF "interval" background), but this result is far from being definitive. Holes are observed in angular distribution spectra, and correspond to events whose angular direction is distributed around the direction of the strips, i.e. to horizontal or vertical events (see figure 2.38). These holes seem correlated with the use of an new "tsci" cut (a 2D "topographic" cut is defined from scirise × tsci "plot", to reject events coming from anode with more efficiency). Thus more investigations are needed. We hope however that a "convincing" recoil e^- spectra concerning $\bar{\nu}_e e^-$ scattering will be realized from period III and will give interesting results concerning μ_ν .

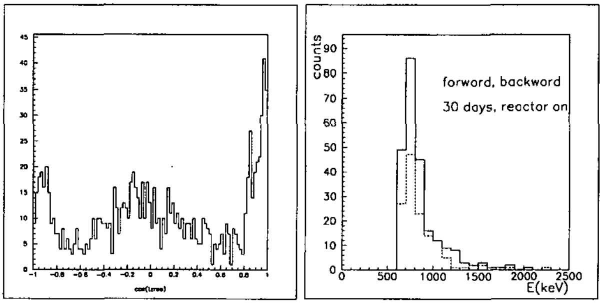

Figure 2.38: In the right figure we see the distribution above 700 keV of events not oriented "anode → cathode" in function of $\cos(\theta_{z,rea})$, see section 2.2.2; we can observe the "excess" of events oriented from combustible to detector, but also "anomalous" holes for horizontal and vertical directions. The difference between forward and backward events, both represented on the left figure, is 2 times stronger than expected.

The result of the reconstruction of the incident energy obtained from the 835 keV γ emitted by ^{54}Mn source shows that the spectroscopy of low energy ν is attainable. The ultimate goal is to use an upgraded underground MUNU detector (SUPERMUNU), where the background conditions are optimal, and to look for solar ν, but a lot of work remains to do. In particular, still larger TPCs are required, and thus larger detection planes adapted to ν detection, which is the subject of chapter III.

Chapter 3

Detection planes

3.1 New detection planes for new experiments

The first motivation for tests and developments on detection planes is the utilization of a TPC for future "low" energy ν (or $\bar{\nu}$) experiments. TPC presents various "interesting" features but such experiments "imply" also various constraints (see previous Chapters). The principal sources of "constraints" on TPCs "constitution" and "functioning", for "low" energy ν detection are:

- "low" scattering cross section of the reaction between ν and e^-
- "low" energy of ν

Low scattering cross section and low energy ν
(the most of the items below were already "presented" in section 2.1.1) ⇒

- "high" number of "targets"
  (otherwise the "low" scattering cross section imply a "too low" rate) ⇒
  - "high" volume of gas
  - "high" pressure (for a given temperature and volume)
  - "high" e^- density (for a given gas density)
- "low" radioactivity
  (many "concurrent" reactions can come from natural radioactivity because of the "low" energy of ν; the detector is very sensitive to these "concurrent" reactions because of the "low" rate due to the "low" scattering cross section) ⇒
  - "low" activity materials
  - as few matter as possible
  - cleanest conditions possible (for realization, transport and installation)

We need thus a large low activity detector containing an "appropriate" gas. CF_4 presents the quality required for ν detection (see section 2.1.1; ^{136}Xe can be used for the search on $0\nu\beta\beta$ decay). In MUNU the active volume is of 1 m^3 of CF_4 at 3 bars and about 10 ν are expected each day. The rate of events expected in solar ν detection (or in other type of experiments on ν like $0\nu\beta\beta$ decay in ^{136}Xe) for the same gas quantity is still lower (the "reactor" $\bar{\nu}$ flux in MUNU detector is higher than the "solar" ν flux on earth), so we have to increase the quantity of gas to get an acceptable sensitivity. About 2 solar ν including pp ν, whose energy is above about 200 keV (pp ν constitutes 92 % of the ν flux in the Solar Standard Model), are expected each day in SSM for 200 m^3 of CF_4 at 2 bars. Thus, if we want to go further in ν or astrophysics exploration with TPCs, we have to build larger TPCs than MUNU's one.

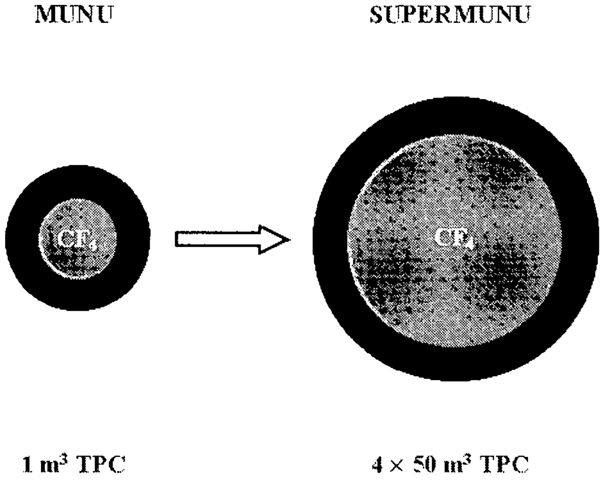

Figure 3.1: MUNU (on left) detects the $\bar{\nu}$ coming from a reactor, where the $\bar{\nu}$ flux is "high". 1 TPC of 1 m^3 is filled with CF_4 and is surrounded with an active shielding and a passive shielding. The expected rate of events is of about 10 events each day. superMUNU (on right) detects solar ν extending down to pp ν. 4 TPC of 50 m^3 are filled with CF_4 and are each surrounded with an active shielding and a passive shielding. Expected solar ν events rate is of about 2 events each day above 200 keV.

An experiment concerning solar ν detection such as superMUNU, with a larger detector and a lower rate than in MUNU experiment, can appear almost impossible to realize. We can however distinguish some "positive" aspects concerning experiments on solar ν detection with TPCs, such as:

- they would beneficiate of the experience of MUNU and other experiments and they would be the result of an international (European for MUNU) collaboration with higher financial and human resources than MUNU's ones.

- working "conditions" in a "simple" underground environment are less "difficult" than in a nuclear central environment (radioactive contaminations, access, electromagnetic noise, etc.)

- the position of the sun is moving and we can measure the scattering angles, so we dispose of a "permanent" OFF "interval" related to the directions perpendicular to the sun

- it is possible to improve the angular resolution (reduction of the electromagnetical noise, new techniques of track analysis, new detection planes, etc.) and thus to obtain a more performing kinematic online background rejection

- calibrations with sources and μ and "localization" of background sources should be easier in a "large" volume TPC than in a "small" volume TPC

In this work I did some "investigations" to find detection planes which would be adapted for the detection of ν in a larger TPC than MUNU's one. MUNU's detection planes are the largest existing "single" wires detection planes ($\emptyset$ = 90 cm), i.e. with "single" wires crossing all detection plane, and it seems very difficult to realize larger "single" wires detection planes functioning without "frequent" wire "break". Larger TPCs with wires detection planes exist at CERN, but the supports are made of solid "stars" to which wires are "weaved". Much efforts to reduce activity have to be done if we want to utilize such a configuration for future experiments. Another possibility is to replace wires detection planes by another type of detection planes adapted for ν detection with a TPC; this corresponds to the principal "objective" of this work. Detection of ν with a TPC "imposes" the following "features" on detection planes:

- they must be "large"
  (it must be possible to realize detection planes until about 3 m of diameter)

- they must present a low radioactivity
  (they should be made of a "little" quantity of "low" activity materials)

- they should operate in CF_4 or in other gases aimed for ν detection

- they must operate with a "low" drift field
  ("long" drift distance and limited difference of potential on drift zone)

- they have to be "reliable"
  (for example resistant to discharges)

A lot of work remains to build detection planes satisfying to all of this criteria and to realize all the developments needed to make an experiment on solar ν with a TPC possible, but I think it is worthwhile.

In this work "investigations" were done on 4 detection planes: the GEM, the LEM (similar to GEM but with higher dimensions), the Micromegas with "grid" (i.e. "classic" Micromegas) and the Micromegas with "cloth". These detection planes are all "amplification" planes and are used to detect the total charge collected (along time, but only the integration of the corresponding electronic signal, i.e. "energy", was considered). In all case amplification corresponds to an electronic avalanche due to an intense drift field resulting from detection plane configuration, as it was the case for wires planes, see section 2.1.1. I have realized and installed in a "new" local a "system" to do these tests (some parts of equipment used were previously installed in 2 "old" locals, in a different way). For this work I have beneficiated from the precious help of Jose Busto (also during all the rest of my work), Antoine Geiser, principally during his licence work with me and also sometimes after, and Giovanni Gervasio, in the beginning of that work (see also preface). Tests were performed with $ArCH_4$, because it is a current gas in which tests are easy to perform, and with CF_4, for pressures varying from 0.1 to 2.5 bars.

3.1.1 GEM and LEM presentation

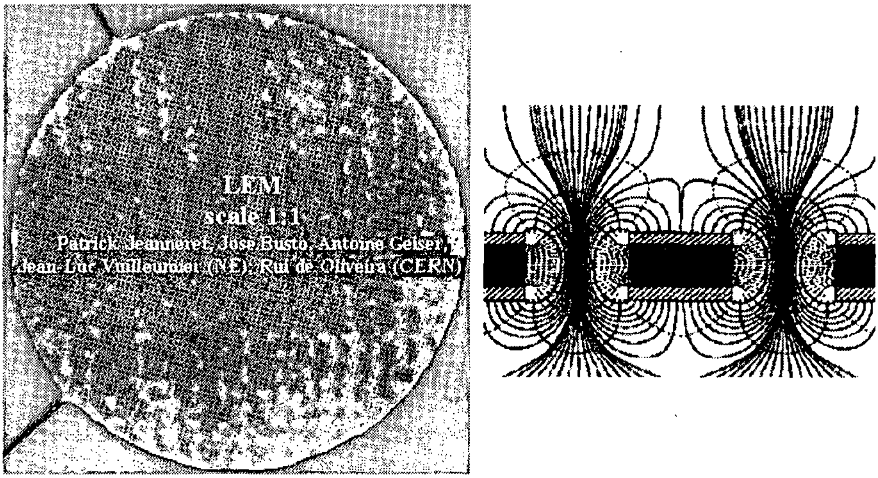

Figure 3.2: LEM = GEM X 10

The GEMs [32, 33, 34, 35, 36, 37] (Gaseous Electron Multiplier) tested are made of 50 μm Kapton (polyimide) foils covered with a thin copper disk of 9 cm of diameter on both sides. Holes of 50 μm of diameter are pierced on a square matrix, with a pitch of 100 μm. GEMs are done by etching techniques and have to be stretched on a rigid support. GEM's and LEM's functioning principle is identical. A difference of potential is applied between the two copper faces, which are separated by a dielectric, and, due to the conservation of the electrical field flux, the field is more intense inside of the holes than outside (Figure 3.2). This intense field accelerates sufficiently each drifting e^- to produce an avalanche. An "anode" situated at a few mm of GEM on the side opposite to drift is necessary to collect a "sufficient" fraction of the drifting avalanche e^-, unless the GEM can't work (too frequent discharges); this anode doesn't seem to be useful in the case of a LEM and was not used for tests. On GEM (or LEM) drift volume side we can read a positive signal. The latter is induced by the ions produced in avalanche and drifting slowly toward drift side surface and cathode. On the other GEM (or LEM) side we can read a negative signal. It is induced by the avalanche e^- drifting quickly and penetrating into the GEM (or the LEM) or into the anode and also by the drifting ions. Cathode and GEM (or LEM) delimit conversion gap, i.e. drift volume, and holes correspond to amplification gap.

The LEM (Large Electron Multiplier) "results" from a "discussion" between Rui de Oliveira (at CERN), José Busto and myself and was realized at CERN. The idea is that we do not need the very fine spatial resolution offered by the GEM for ν detection in a TPC. LEM structure is large enough to be made mechanically rather than by etching techniques. LEMs have been fabricated from a 0.5 mm thick common Printed Board Circuit material, on which a copper disk of 90 cm of diameter was left on both sides. Holes of 0.5 mm of diameter were drilled on a square matrix through this circular area, with a pitch of 1 mm (Figure 3.2). The latter is well adapted to the size of an ionization cloud resulting from the amplification of a "punctual" source belonging to the "initial" track in a TPC whose dimensions are of the order of MUNU's ones. LEM presents various interesting features:

- its realization is mechanical instead of being chemical
- it is rigid and "self supporting"
- it is extremely sturdy and "cannot" be destroyed by discharges
- very large LEMs should be easy to produce, with eventually strips engraved

The difference of potential needed for LEM's functioning is much smaller than we could expect at a first sight. For example, the difference of potential we must have in $ArCH_4$ at 1 bar is about 4 times that needed for a GEM. This is a small difference, if we compare with the volume of the holes, which is about 100 times bigger in the LEM than in the GEM. This can be explained by:

- the identical value, for LEM and GEM, of fraction between holes and copper surface
- the greater distance available in LEM for amplification

3.1.2 Micromegas "with grid" and "with cloth" presentation

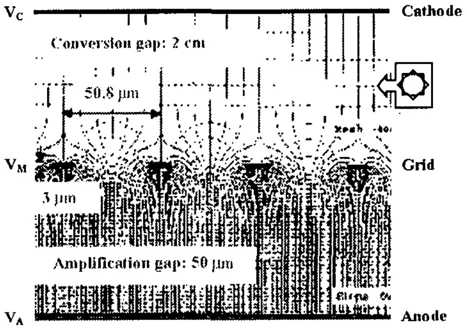

Figure 3.3: Conversion and amplification gap in a Micromegas.

The Micromegas [38, 39, 40] is another alternative to multiply the ionization charge. The only difference between the Micromegas with "grid" (i.e "classic" Micromegas) and the Micromegas with "cloth" is the replacement of the "grid" (Figure 3.3) by a "cloth" (Figure 3.4). We have obtained from Ioannis Giomataris at Saclay a Micromegas grid of 9 cm of diameter made of a nickel mesh of 50 μm pitch with 3 μm width "strips", stretched on a nickel ring. The grid is realized by etching techniques. The parallelism between the micromesh grid and an anode is maintained every 2 mm by spacers of 150 μm of diameter situated on anode. These spacers are printed on a thin epoxy substrate by conventional lithography of a photoresistive film. We have done tests with 50 μm height spacers on that foil, and also with 100 μm height spacers on another foil, which we have stretched on a copper ring. The "fixation" of the grid on "spacers" is realized in an "electrostatic" way by the difference of potential applied between grid and anode. To make the electrostatic "fixation" possible, the grid has to be "stretched" on the ring, but "not too much". When the fixation is not perfect, the grid is not flat and we see "rings" corresponding to an optical "interference" between the square mesh of grid and spacers. If the difference of potential is sufficient for fixation and if the grid is perfectly flat, rings disappear. In a Micromegas detector, the conversion gap is situated between a cathode and the grid, and amplification gap between the grid and the anode. The very intense field, due to the difference of potential applied on the very narrow distance between grid and anode, is producing an avalanche for each drifting e^-. (Figure 3.3). We can then read a positive signal on grid, induced by the ions drifting slowly toward cathode and a negative signal on anode, induced by the e^- penetrating into the latter and also by the drifting ions. The "perfect" equidistance between grid and anode, which is due to the electrostatic "fixation" and can be verified by the disappearance of "rings", corresponds to a "perfect" homogeneity of gain.

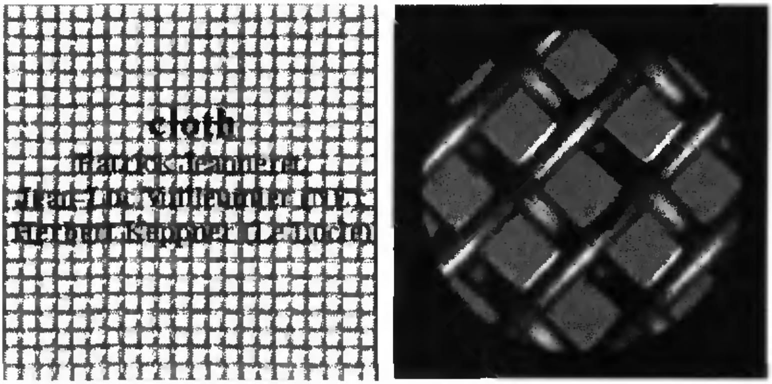

Figure 3.4: 2 views of a "cloth", made of stainless steel wires weaved in a "crossed" way.

The Micromegas "with grid" described above presents various interesting features for ν detection, as we will see in this Chapter. However, only "small" sheets (of the order of 50 × 50 cm) can be obtained, which implies to develop "pavements" with "connectors". The Micromegas has a "low" mechanical resistance, so it has to be manipulated with care. Searching for alternatives for detection planes, I have discussed with Herbert Keppner of the Engineer School at Le Locle, and he showed me a "cloth" made by weaving very thin metallic wires. I decided to try to replace the grid of the "Micromegas" by such a "cloth". I obtained from a factory in the eastern part of Switzerland a piece of cloth (custom uses for such cloths are filtration, screen matrix realization or electronics; this factory affirms to be the unique factory in the world producing so "thin" metallic cloth, and that it possible only since few time. The cloth is made of stainless steel wires of 20 μm of diameter weaved in a "crossed" way, see figure 3.4, with a pitch of 50 μm (same pitch as for a "grid"). The diameter of the cloth wires is identical to that of the anode wires, but the "weaving" makes cloth much more "sturdy" than anode wires. The utilization of such a cloth as an "anode plane" is not possible, at least for a potential value on the cloth of the same order than on the anode, because the high wires density of the grid corresponds to a "low" electric field around wires, for a given potential. The "cloth" seems to behave like a "grid" in the preliminary tests I have realized, see section 3.6.4, but more tests remain to be done for confirmation (or to "measure" behavior differences). Cloths with matrices engraved by lithography can be obtained from the factory, see figure 3.5, so it should be possible to obtain cloths with spacers ("normally" spacers are on the anode, so the "equidistance" should be "examined" in such a configuration). I have also realized preliminary tests with 2 successive cloths (i.e. replacing anode by a grid), which is interesting if we want to observe avalanche scintillation light. This configuration "works", however a bad resolution was obtained, which was probably corresponding to an inhomogeneity of gain due to the absence of spacers.

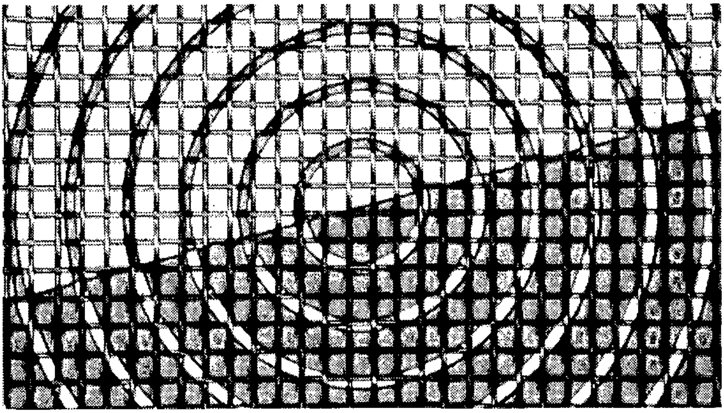

Figure 3.5: Cloth with a "matrix" engraved by lithography

The cloth presents various interesting features:

- its realization is mechanical instead of being chemical
- it is sturdy, easy to hand, and seems still more resistant than grid to discharges (wires "don't move" inside cloth, even if a hole is made in the latter)
- "rolls" of dimensions up to 3 × 40 m can be obtained
- "low" cost, about half price that of a Micromegas grid, for the same dimensions
- the "stretching" behavior seems identical to that of grid
  (i.e. the "perfect" equidistance between cloth and anode can be obtained by an electrostatic "fixation" and can be verify by the disappearance of "rings")

However, even if cloth material quantity is "low", grid material is still lower ($\emptyset = 20\ \mu$m for cloth wires and $\emptyset = 3\ \mu$m for grid strips), which is an advantage for grid concerning low activity.

3.2 Description of the "systems" used for tests

3 different "systems" can be used to test detection planes:

- the "plastic box"
  (the "plastic box" is a "simple" system for preliminary tests; it is used only to test detection planes in "$ArCH_4$", which is made of a mixture of 90 %Ar and 10 %CH_4, at a pressure of 1 bar)
- the "mini TPC"
  (the mini TPC is a cylindrical TPC of 15 cm of diameter and of 20 cm of height; it is used to test detection planes in $ArCH_4$ and CF_4, for pressures varying from 0.1 to 2.5 bars)
- the "TPC"
  (the TPC is a large "flat spherical" TPC of 1 m of diameter and of 40 cm of maximal height, it could also be used to test "new" detection planes, but until now it was used only to test MUNU's detection planes, so it doesn't concern this Chapter)

A gas system (with a "control panel") is common to mini TPC and TPC (in the "plastic box" there is only a simple gas injection, see section 3.2.3). Electronic (HV power supply, readout, etc.) is common to the 3 "systems", except for HV filters, HV "signal cut" capacitance and preamplifiers, which are "specific" to each system, and mini TPC has is own "3D" acquisition (also used for Gotthard experiment), see section 3.2.4. All systems can be used to realize spectra, to measure the gain, the current and the energy resolution, at various potentials and, for mini TPC and TPC, in various gases and pressures, see section 3.4.

3.2.1 "Plastic box", for preliminary tests

For the preliminary tests, I have realized a "plastic box", see figure 3.6, containing a "rudimentary" TPC and presenting some interesting features:

- it is easy to open and close
- there is no vacuum operations (the gas, i.e. $ArCH_4$, is injected inside plastic box and rejected by a "bubbler" until it can be considered as "cleaned")
- the different detection planes (GEM, LEM, Micromegas, etc.) can be easily changed and the configuration of the "TPC" is easily "modifiable"
- the "plastic" is very thin, so a source generating X-ray of a few keV can be put outside of the plastic box (at "these" energies, the tracks of "ejected" e^- inside gas are of a few mm length and are mostly contained in the drift volume; the source used is "switchable", so energy spectra with "some" peaks are easy to obtain)
- the system is "transparent", to "localize" discharges or other "problems"

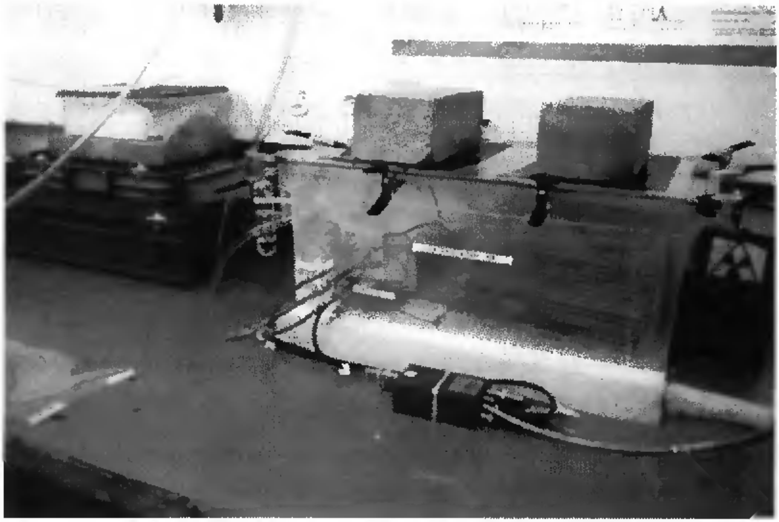

Figure 3.6: The "plastic box is supported by an anti-vibration material. Inside we "see" the HV filters and the HV signal cut capacitance, on left, and the Faraday cage containing the "TPC", on right. The preamplifier is situated in the front of the plastic box and the radioactive source "container" on the right.

The following "elements are contained inside plastic box:

- HV filters and HV signal cut capacitance
  (the HV filters for the cathode and the anode planes, and the HV "signal cut" capacitance with a filter for the detection planes, are all "fixed" on the same copper "plate", to be at the "same ground", see section 3.2.4)

- detector, anode and cathode, contained inside of a Faraday cage
  (the cathode and the anode are situated on each side of the "detector", i.e. GEM, LEM, or Micromegas with grid or with cloth, at the same distance of the latter, i.e. 2 to 3 cm, see section 3.3 and figure 3.13; anode is necessary for GEM only; the Faraday cage is used to prevent from electromagnetical noise and is also "put" at the same ground as the other electronic components, except the "readout" computer, see section 3.2.4)

The preamplifier is situated outside of the "plastic box", as close as possible of the latter, to avoid the collection of electromagnetical noise before amplification. The "system" is very sensitive to vibrations, so it has to be supported by an anti-vibration material.

3.2.2 "Mini TPC", for tests

The mini TPC, see figures 3.7, 3.10, 3.12 and 3.13, is used to test the detection planes in $ArCH_4$ and CF_4, for pressures varying from 0.1 to 2.5 bar. A non removable ^{55}Fe source is present on the top of the TPC, and the "switchable" source used for the plastic box can also be introduced in the mini TPC (see sections 3.3.1 to 3.3.3). The gas system is described in section 3.2.2, the electronic and the acquisition in section 3.2.4 and the internal configuration in section 3.3.

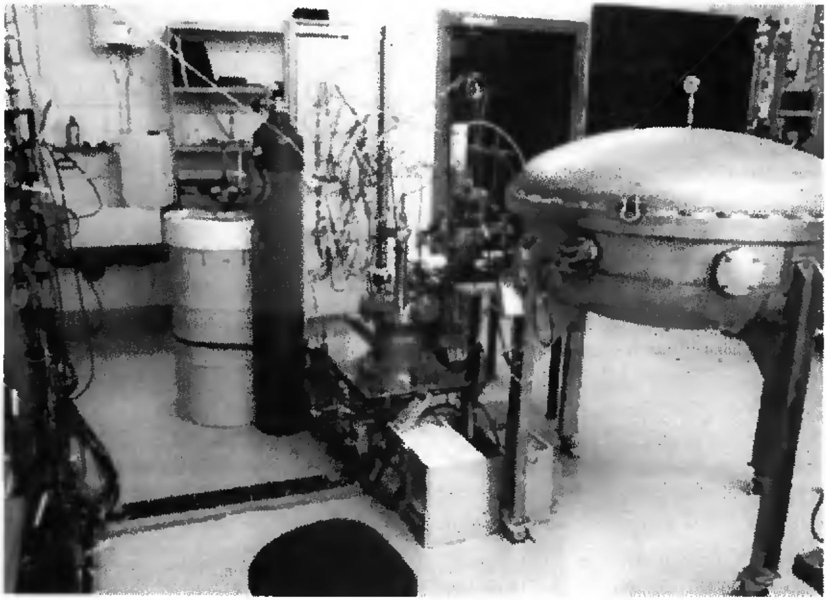

Figure 3.7: The mini TPC (vertical "cylinder") is situated in the center of the figure and the TPC (flat "sphere") on the right. We can see the gas system common to the mini TPC and to the TPC (i.e, from left to right, CF_4 recuperation vessel, CF_4 injection bottle, back of circulation control panel and Oxysorbs and cold trap for gas cleaning) behind the mini TPC. As for the plastic box, a copper plate is fixed on the mini TPC and another, with filter and "cut" capacitances, on the TPC. The role of the copper plate is to "put" the filters and the cut capacitance at the "same ground". The preamplifiers are also fixed on the mini TPC and on the TPC, as close as possible of the latter, to avoid noise collection before amplification. The XY preamplifiers of the mini TPC are situated in the front of the latter. We can see a part of the rest of "acquisition" on left.

3.2.3 Gas system

The "principle" of the gas system (gas injection, recuperation, circulation and gas cleaning) is identical to that of the MUNU experiment, see section 2.1.1. However, the "material" realization of the gas system is much simpler than in MUNU experiment (in MUNU the TPC is made of acrylic, surrounded by scintillator oil, and both gas and oil pressures have to be controlled with precision in a manual or in an automatic way, because a too high pressure difference would break the TPC; the mini TPC and the TPC presented here are "simple" steel TPCs, in which only gas pressure has to be "controlled", in a manual way). I tried to "design" the simplest circulation system possible and drew its "plan" on a control panel, see figures 3.8 and 3.9. I was strongly helped by José Busto for the installation of the gas system. $ArCH_4$ doesn't need to be cleaned for the tests (a "good" vacuum before gas injection is sufficient) and is only "circulated" during the tests. In reason of its "already" high electronegativity, which is related to its high attachment factor, CF_4 has to be cleaned to remove O_2 and H_2O, otherwise the drift is impossible (2 Oxysorbs, which can be a source of radon, see figure 2.14, are used on this system, but the presence of radon is not important for the tests described in this Chapter). To be cleaned, the gas "circulates" continuously in 2 successive Oxysorbs (the second one is "small" and transparent, and the color of its chemical components is modified when the latter "absorbs" O_2 or H_2O, so it is used as a "witness" of the efficiency of the first Oxysorb, which is "big" and "opaque"), in a cold trap (inside of a serpentine, whose temperature is of about -90 °C, to remove H_2O; the temperature of the serpentine is automatically controlled by the injection of nitrogen liquid in a recipient surrounding the serpentine, and by a "heating" situated on the serpentine; the temperature is measured by thermal resistances) and in mini TPC (or in TPC).

Figure 3.8: The cold trap and a part of the system used to control its temperature is situated on left, on the white table, the control panel with the 2 Oxysorbs in the "middle" and the CF_4 recuperation vessel on right.

The plan of the gas system for mini TPC and TPC is the following:

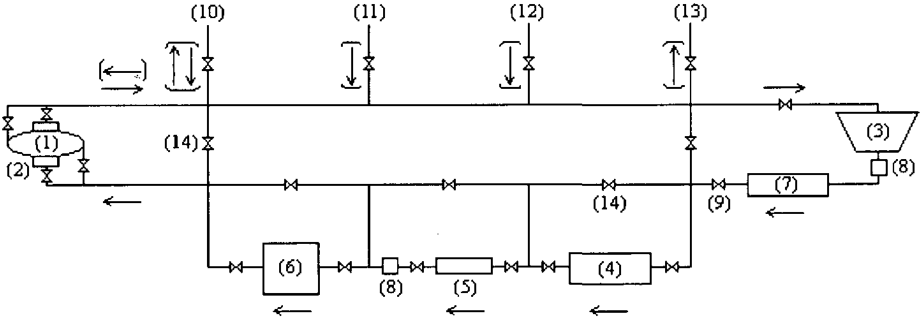

Figure 3.9: Gas system

(1) TPC

(2) mini TPC

(3) circulation pump

(4) "big" Oxysorb (opaque)

(5) "small" Oxysorb (transparent, i.e. "witness")

(6) cold trap

(7) flowmeter

(8) "mechanical" filter

(9) valve (this one is used to control the flow)

(10) CF_4 recuperation or entry (to or from "vessel")

(11) CF_4 entry (from "bottle")

(12) $ArCH_4$ or "other gas" entry

(13) vacuum valve (also one on the mini TPC and one on the TPC)

(14) bypass

3.2.4 Electronic and acquisition

An acquisition program to visualize and record 3D events (XZ and YZ projections, see section 2.1.4) and their energy has been written by Roland Luesher and myself for Gotthard experiment (to replace an old one, which "collapsed") and mini TPC. Roland Luesher has written the part concerning data recording ("packing") into files and data reading ("unpacking") from files and "time management" (for example possibility to stop "temporary" data acquistion), while I have written the CAMAC interface routines (whose principal functions are "memory boxes" control, for "strips signal" reading, "transient recorder" control, for "energy" reading from anode wires or other detection planes, and "trigger boxes" control, for "triggers" generating and "synchronization"), and the graphical routines. The transient recorder (1024 words coding on 8 bits, i.e like FADC, see section 2.1.4) records "directly" energy signal (after preamplification), while the memory boxes (1024 words coding on 8 bits) record strips X an Y signals from "2 levels discriminators" (after preamplification). Everything has been written in C-language and has been compiled with Borland C++. This program is used in the Gotthard experiment and is faster than the old one (at least by a factor 2). It "works" also for mini TPC, but wasn't much used because the tests that have been performed concern almost only "energy measurements" and not "spatial measurements" (i.e. using XY "strips" signals), and a simpler system has been used for "measurements" (concerning energy spectra, gain and current). I tried to do the simplest electronic system possible, which makes it easier to use and reduces the collection of electromagnetical noise, see figure 3.10

Figure 3.10: The electromagnetical noise reduction is very important for resolution and fundamental for measurements at "low energy". To avoid noise collection and radiation, all electronic and alimentation cables are put in the same "tubes" (from center to left on figure). "Masses" ("external" and "internal") of every devices are put at the same ground (except for the computer, which has been isolated by "opto-coupling" of the rest of the experiment, because the high frequencies of the latter influence strongly the "ground"), via common copper plates or mass braids, in a "star" configuration. An unique electrical alimentation is common to the whole system except computer.

Objectives and realization of "measurements" (concerning energy spectra, gain and current) are presented in section 3.4.3. The electronic configuration used for HV settings (related to amplification field, drift field, etc., see section 3.3) and "measurements" is the same in the plastic box, in the mini TPC and in the TPC and is described in the following figure:

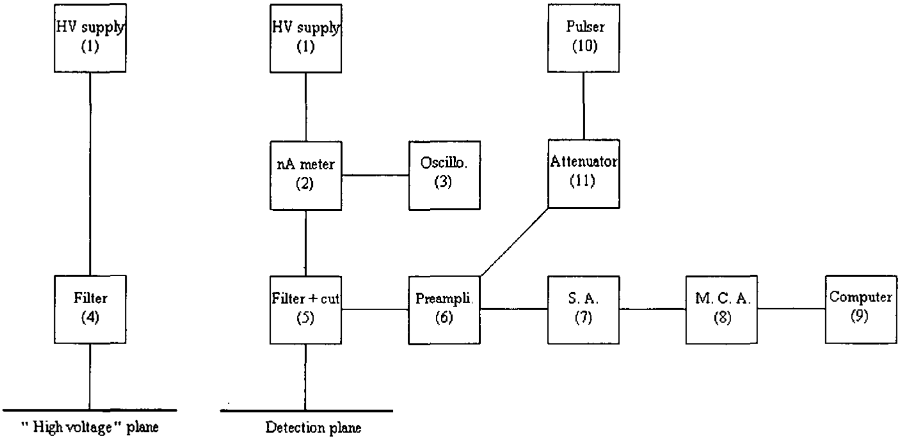

Figure 3.11: HV supplies and electronic system to measure gain, current and resolution

(1) HV power supplies, to put planes like cathode and detection planes on "high" voltage

(2) nano Amperemeter, to measure current on detection surface (lowest scale = 100 pA)

(3) oscilloscope, to read "mean" current from nano Amperemeter ("base time" = 2 s)

(4) HV filter, for filtering a part of the "noisy" frequencies

(5) HV filter and capacitance, to "cut" the signal induced by avalanches ions or e^-

(6) Ortec 142IH charge preamplifier (minimal rise time = 20 ns)

(7) Spectrosopy Amplifier, to amplify and "integrate" signals ("shaping" $\tau = 1\ \mu s$)

(8) Multi Channel Analyzer, to do spectra from the "integrated" signal of each event

(9) computer, in which all spectra are sent (for analysis with paw)

(10) pulser, to send pulses in the test entry of the preamplifier (section 3.4.3)

(11) logarithmic attenuator, to modify the height of the pulses

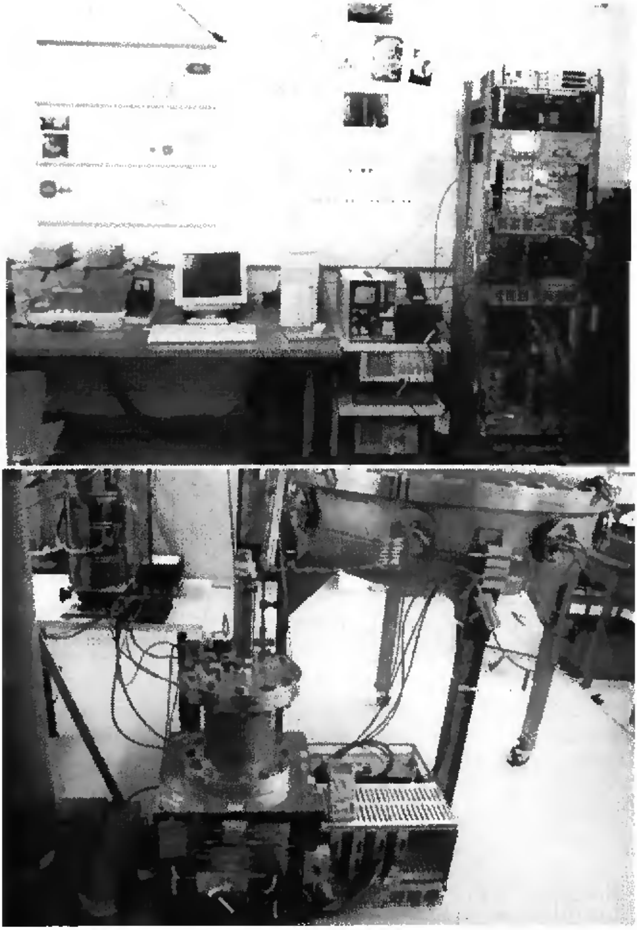

Figure 3.12: On the first figure, we see, from right to left, a crate with HV supplies, electronic devices for signals processing, Camac devices for 3D acquisition, etc., a support with readout devices, and the computer. On the second figure we see the mini TPC and the TPC with, both, a grounded copper plate supporting HV filters and a cut capacitance, and an ORTEC 1421H preamplifier (removed on TPC) to amplify detection planes "energy" signals; we see also a crate with TRA 1000 preamplifiers to amplify X and Y strips signals (for mini TPC) and, on the mini TPC, a potentiometer connecting to ground the field shaping rings resistances chain supplied by the cathode (for mini TPC and TPC; potential value on field shaping ring 1, i.e. first one "since" detection plane, can be read on the multimeter).

3.3 Configuration during tests

In high energy physics, the detection planes have to work with an intense (corresponding to a high events rate) high energy particles flux. Thus they must be resistant to radiation and "fast" [41, 42, 43], so "configurations" with a very high drift field are required to get a sufficient evacuation of ionization charge. These high drift fields (for example 10 $\mathrm{kVcm^{-1}bar^{-1}}$) are obtained with a thin drift zone (a few mm) and with a high difference of potential between the cathode and the detection plane. Detection planes should also have a high spatial resolution (shorter than 1 mm for vertices determination), which required to find configurations with a spatial resolution of the order of GEMs or Micromegas pitch [44].

In low energy ν physics (low energy events and low rate) the qualities required for detection planes are different of those required for high energy physics, so working "configurations" are different (see section 3.1). The drift zone is "large" (several cm to a few m), and thus the drift field is low, of the order of 100 $\mathrm{Vcm^{-1}bar^{-1}}$. Tests on GEMs and Micromegas have shown that such low drift fields are not adapted (for example energy resolution becomes very bad) to a drift zone distance of a few mm. This can be understood "intuitively", because in the case of a low drift field, the field deformation, due to the high field around the detection plane, is too important inside of the drift zone, for a distance of a few mm from detection plane. However, it seems that these drift field deformations are "already" small at a distance of a few cm from detection planes, see section 3.5.1. Due to their geometry, the 2D Garfield simulation program is not adapted for such detection planes. We should use a simulation program like 3D Maxwell to get a good understanding of these detectors. I have not realized such simulations in my work. I have however tried to get some "understanding" concerning functioning of detection planes by measuring both gain and current, see section 3.4.1. The "exigences" concerning the spatial resolution of the detection planes are a little lower in low energy ν physics than in high energy physics, because the resolution in low energy ν physics is "limited" by the large drift distance and by the e^- scattering. In this work I have only done measurements concerning the energy information, but not concerning the spatial information. Most configurations used to test the GEM, the LEM, and the Micromegas with grid and with cloth in the plastic box and in the mini TPC present the following features:

- drift field $\simeq$ 100 $\mathrm{Vcm^{-1}bar^{-1}}$.
- the drift distance is of 2 to 3 cm in the plastic box and of 20 cm in the mini TPC
- the drift zone is delimited by the cathode and the drift side surface of the detection plane; the potential is negative for both cathode and detection planes ("more negative" in case of the cathode); the measurement of the signal is done on the drift side surface of the detection plane
- the surfaces of the GEM and of the LEM opposite to the drift side and the anode of the Micromegas are "grounded"

3.3.1 Configuration inside of the plastic box

The plastic box is always filled with 1 bar $ArCH_4$ (90 % Ar, 10 % CH_4) and the drift field value used for measurements is of about 100 Vcm^{-1}bar^{-1}. The "current configurations" used for measurements inside of the plastic box are described in the following figures:

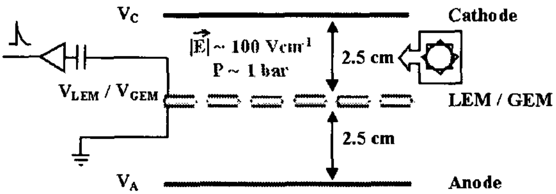

Figure 3.13: The "star" indicates the position of the "switchable" source. The anode seems useful (for e^- collection) only in the case of the GEM. The signals are read on the drift side surface via a cut capacitance and a preamplifier (the other detection surface is grounded). An example of potential settings for the GEM corresponding to "good working conditions" (i.e. good resolution and gain, without discharges) is V_{GEM} = -470 V, V_C = -775 V, V_A = -0 V and an example of potential settings for the LEM corresponding to good working conditions is V_{LEM} = -1700 V, V_C = -2025 V, (V_A = -0 V).

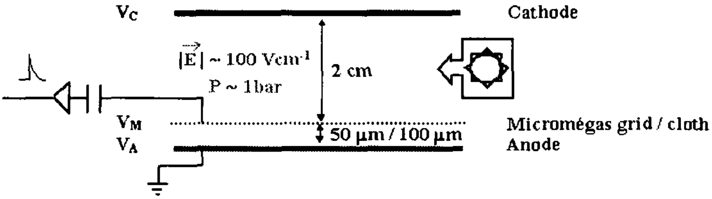

Figure 3.14: The Micromegas with grid was tested with amplification gaps (defined by anode spacers) of 50 μm and of 100 μm (in Ar with 5 % DME, simulations, verified by tests for these 2 gaps, of the gain at different potentials, in function of the amplification gap have shown that amplification gaps of this order correspond to "optimum" gains in good working conditions [39]). An example of the potential settings for the Micromegas, with a grid of 50 μm, corresponding to good working conditions, is V_M = -375 V, V_C = -635 V, V_A = -0 V. The Micromegas with cloth was only tested with an amplification gap of 100 μm.

3.3.2 Configuration inside of the mini TPC

The mini TPC is filled with $ArCH_4$ (90 % Ar, 10 % CH_4) or CF_4 at pressures varying from 0.1 to 2.5 bars and the value of the drift field is of about 100 $\mathrm{Vcm^{-1}bar^{-1}}$ (like for the plastic box). The "current configurations" of the mini TPC are described in the following figure:

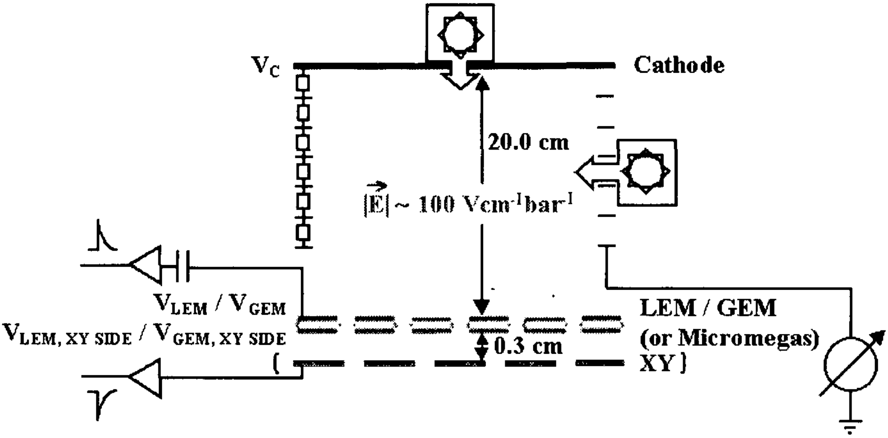

Figure 3.15: The "switchable" source, on right, can be removed and on the top of the mini TPC there is an unremovable ^{55}Fe source, see section 3.3.3. The horizontal "dashed" lines around the drift volume correspond to 9 field shaping rings. They are connected via 9 resistances of 10 MΩ from the cathode to a potentiometer connected to ground. The role of the field shaping rings is to define a constant drift field, see section 2.3.3. The LEM or the GEM can be replaced by a Micromegas (grid or cloth and anode with spacers). The amplification gaps between the Micromegas grid or the Micromegas cloth and the anode used for tests are of 50 μm and of 100 μm. The signals are read on the drift side surface via a cut capacitance and a preamplifier and the other surface of the GEM, of the LEM or of the anode of the Micromegas are grounded. The XY plane has not been used for tests.

3.3.3 Radioactive sources

The 2 sources used for the tests (^{55}Fe source and switchable source, see below) produce X-rays of "a few" keV, which irradiate the gas contained in the drift volume of the detector, or eventually a solid part of the latter (like Cu contained in the cathode and the GEM or the LEM surfaces). At these energy values the photoelectric effect (i.e. the ejection of a bound e^-) is more important than the Compton effect and e^- whose energy is equal to the energy of the initial X-ray minus the binding energy of the e^- in the atom of gas are thus produced. Inside of the gas these e^- "travel" "a few" mm (corresponding to an initial kinetic energy of a few keV; the mean distance "travelled" by X-ray before absorbtion by photoelectric effect is of "a few" cm) and the corresponding tracks are mostly contained in the drift volume. The hole resulting from the ejection of the e^- by photoelectric effect produces a rearrangement of e^- in atom, and "rearrangement X-rays" (X ray emitted by the source are also produced by rearrangement processes) are emitted and "eject" also e^- of other atoms. We have thus a "cascade" of rearrangements. When the tracks of the e^- ejected by the X-ray of the source and of every e^- ejected during the cascade are contained in the drift volume (which is possible only if every X-ray of the cascade is "absorbed" in the drift volume), the energy measured (after integration by "shaping", see section 3.4; this energy is equal to the sum of the kinetic energy left in all these e^- tracks because cascade "events" occurs "quickly") is equal to the energy of the X-ray of the source (this will then correspond to a peak, at this energy, in the spectra realized from a lot of events coming from source, see figure 3.16). "Rearrangement X-rays" are produced by e^- when corresponding e^- state (orbital) is "changing" from a given energy to a lower energy. X-ray energy is thus equal to the difference of energy between these 2 states. If one of these "rearrangement X-rays" "escapes" from the drift volume, its energy is "missing", i.e. the energy measured is equal to the energy of the X-ray emitted by the source minus the energy of the "rearrangement X-ray" (this correspond to an escape peak, see figure 3.16).

The ^{55}Fe source is an unremovable source present inside of the mini TPC and emitting mainly X-rays of 5.90 keV. In this source e^- "captures" occur, which correspond to a weak interaction between an e^- of the K shell and a proton ($p + e^- \rightarrow n + \nu$). Rearrangements of e^- occur and the X-rays of 5.90 keV are emitted during the e^- transitions $L \rightarrow K \equiv K_\alpha$ transitions, whose energy is equal to the difference between these 2 states. This energy is not equal to that (6.404 keV) of the X-ray emitted by Fe during the K_α transition due to fluorescence processes (see below), because the changing of the charge number of the nucleus $Z \rightarrow Z - 1$ has to be taken into account to compute the energy of the "final" e^- state L during the e^- "capture" processes. When measurements are done in $ArCH_4$, "rearrangement X-rays" corresponding principally to the 2.96 keV K_α transition in Argon can escape from the drift volume. Thus if the ^{55}Fe source observation is done with $ArCH_4$, 2 peaks are obtained. The energy of the first one (more intense) is of 5.90 keV and the energy of the second one, which corresponds to the escape peak, is of 2.94 keV (5.90 keV - 2.96 keV), see figure 3.16. No escape peak can be observed with CF_4.

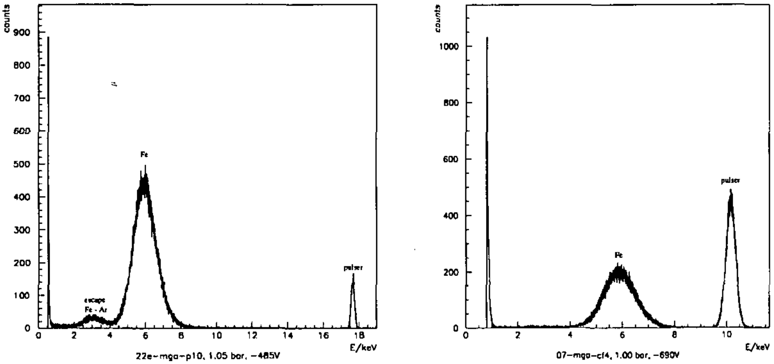

Figure 3.16: Observation of the ^{55}Fe X-rays, using a Micromegas with grid, in the mini TPC filled with 1 bar of $ArCH_4$ (on left) and with 1 bar of CF_4 (on right). The peak of right corresponds to a pulser (the background noise, on left, is cut). The 5.90 keV peak is present on both figures and the 2.96 keV escape peak only in the left one.

The switchable source is removable and is used to irradiate the plastic box and the mini TPC. Its hearth is an ^{241}Am source, producing principally α and 59.5 keV γ. These α and γ can irradiate different "switchable" metallic targets mounted on the source. One of the effects is to eject e^- of the target's K shells, and the e^- rearrangements following these ejections produce X-rays $\equiv$ fluorescence X rays of different energies, corresponding principally to K_α transitions (L $\rightarrow$ K), and K_β transitions (M $\rightarrow$ K), which are less frequent than K_α e^- transitions (and correspond thus to "smaller" peaks, which are more difficult to observe). In the tests 2 targets were used. The first one is an *Ag* target, emitting by fluorescence X-rays of energy $K_\alpha = 22.10$ keV and $K_\beta = 24.99$ keV, and the second one is a *Ba* target, emitting by fluorescence X-rays of energy $K_\alpha = 32.06$ keV and $K_\beta = 36.55$ keV. The fluorescence K_α and K_β X-rays may then interact with e^- of the gas, producing thus peaks in the spectra at corresponding energy (in both $ArCH_4$ and CF_4) and also escape peaks in $ArCH_4$. They may also interact with e^- of a solid part of the detector, producing for example an "escape peak" whose "missing energy" correspond to the energy K_α of the solid material. The 59.5 keV γ not interacting with the target can interact with gas (but the peak is less "clear" than for lower energies, because there are less contained events and more Compton interactions) or with a solid part of the detector, like Cu, producing fluorescence X-rays with K_α or K_β energies (for example 8.05 keV for K_α X-rays of Cu).

3.4 Tests description

Many ways have to be explored to find a detection plane presenting the qualities required for solar ν detection or other future ν experiments with a TPC, and this work corresponds only to a little part of the "exploration". Some tests have been done having in mind some of the qualities required for ν detection. First we have done some tests on GEM, which was chosen in reason for example of the high gains and resolution possible with the latter, of its simplicity in comparison of wires planes (composed of an anode plane with anode wires and potential wires, and of a grid), and because the latter can be utilized for both energy and spatial detection, by engraving strips on its 2 sides (X strips on one side and Y strips on the other side). As we did not succeed to make "work" the GEM in CF_4, and because it seems very difficult to make large GEMs, the LEM was realized (see section 3.1.1). Tests have shown that the LEM presents some interesting features, but it seems not possible to make function it in CF_4 at pressures larger than 1 bar. It was then decided to test the Micromegas. The latter seems very interesting for ν detection. For example it is functioning in CF_4 at 2 bars, it is more resistant to discharges than GEM, its energy resolution is "impressive" and it is made of few matter (but an XY plane, which could work as the Micromegas anode, is necessary). However, it seems not possible to obtain very large meshes, so pavements have to be developed. For this reason tests were done on a Micromegas where the grid was replaced by a cloth, which is very resistant mechanically and can be obtained in large dimensions (see section 3.1.2). In these very preliminary tests, functioning seems identical to that obtained with a grid, in particular in CF_4 at 2 bars. The replacement of the grid by a cloth is very interesting for the realization of large detectors. However the cloth is made of more material than the grid and improvements concerning its fabrication are certainly necessary to obtain very low activity meshes. Tests on GEM, LEM, Micromegas with grid and Micromegas with cloth were done in $ArCH_4$ and CF_4, at different pressures "steps", between 0.1 and 2.5 bars (temperature $\cong$ 20 °C, so pressure $\cong$ gas density), with $E_{drift} \sim 100\ Vcm^{-1}bar^{-1}$, in the following way:

- find potential working limits (V_{min}, V_{max}) $\Rightarrow$ determine working region (working region $\equiv$ potentials × pressures region were detection plane is "working"; "working" means that signals corresponding to source events can be well separated from noise, i.e. that the energy peak corresponding to the energy of events observed is "well above" noise, and that no, or "very few", discharges appear; discharges can be fatal for GEM and sometimes for Micromegas, but not for LEM, except for preamplifier if the latter is not protected, see sections 3.5.1 to 3.5.4; value of potential with some, or frequent, apparition of discharges has been taken as a limit for tests, even if measurements would still be possible above this value)

- "acquire" spectra for resolution and gain measurement, see sections 3.4.1 and 3.4.2. (proportionality is verified on spectra with at least 2 energy peaks, see section 3.4.2)

- measure current, see section 3.4.2.
  (low rate $\Rightarrow$ gain not necessary $\propto$ current, see section 3.4.2)

3.4.1 Energy resolution

The electrical signal induced by the drifting ions (and e^-) resulting from the avalanches is taken from the surface of the LEM, the GEM or the Micromegas, on drift volume side, see figures 3.11 and 3.13 to 3.15. A capacitance must be used to "cut" the signal (because the surface is set at a negative potential, i.e. different from zero), and the latter (positive) is amplified (and inverted; the inversion is not represented on figure 3.13 to 3.15) by a charge preamplifier ("protected" ORTEC 142IH with a minimal rise time of 20 ns; the "protection" is necessary against discharges occurring on the LEM in CF_4). A spectroscopy amplifier is used to integrate (and amplify) the signal, with a shaping constant set to 1 μs (1 μs is large enough to "integrate" the signal of 1 "cascade" of events, i.e. the events associated to 1 X-ray emitted by the source, and small enough to separate 2 different "cascades"), in order to obtain a signal proportional to the number of e^- after avalanches, i.e.proportional to the energy of the "incident" X-ray (i.e. emitted by the source and interacting in the gas) minus the eventual "escaping energy", see section 3.3.3. A "large" number of events, corresponding to the number of incident X-ray during 100 s (of "life time"), which is the "acquisition" time chosen for each measurement, is sent into a multichannel analyzer to realize the energy spectra (containing for example an "incident X-ray peak", an "escape peak", a "fluorescence Cu peak", see section 3.3.3. and a "pulser peak"). These spectra are then sent into the computer. The energy resolution is defined in the same way as in section 2.3.2. The peaks correspond generally to a "clear" gaussian and gaussian fits are used to fit the latter. Channel number $\equiv n_{ch}$ at the maximum and $\sigma(n_{ch})$ are determined with paw, and $\Delta \equiv$ FWHM is given by $\Delta(n_{ch}) = 2.35\sigma(n_{ch})$. When the e^- multiplication is proportional, which is verified on the spectra with at least 2 peaks corresponding to well-defined energies, E $\propto n_{ch}$. We have then:

$$R = \frac{\Delta(E)}{E} = \frac{\Delta(n_{ch})}{n_{ch}} \tag{3.1}$$

A pulser is used to send a square pulse of defined amplitude to the test entry of the preamplifier to determine the resolution "contribution" $R_{electromagnetic,\,out}$ (measured on the pulser peak) due to the electromagnetical noise "collected" by the detection system outside of the detector. We can suppose than the electromagnetical noise collected inside of the detector (mini TPC) is "not important" (HV filters are used and mini TPC is a good Faraday cage), i.e. $R_{electromagnetic,\,out} = R_{electromagnetic}$. The detector resolution is then mainly "due" to the statistical fluctuation of the mean number N of initial ionization e^- of the track, to the fluctuation of the gain, see section 2.3.2., and to eventual parallel currents, see section 3.4.2. i.e. $R^2_{detection} = R^2_{ionization} + R^2_{gain} + R^2_{parallel\ currents} \Rightarrow$

$$R_{detection} = (R^2 - R^2_{electromagnetic,\,out})^{\frac{1}{2}} \tag{3.2}$$

R is the energy resolution measured "directly" on the energy peak. "Results" (given in section 3.5) concerning the resolution correspond to $R_{detection}$. The latter gives information about the parallel currents, see section 3.4.2, or about the fluctuation of the gain, see section 2.3.2 (spatial term $\Leftrightarrow$ detection plane configuration, drift potential configuration, recombination during drift, etc.; multiplication term $\Leftrightarrow$ attachment, amplification, etc.).

3.4.2 Gain and current

To estimate the gain, a square signal of amplitude U (of 1 ms) is sent with a pulser (as for the measurement of $R_{electromagnetic,\,out}$, see section 3.4.1) into the test entry of the preamplifier to measure the mean number n_{final} of ions "collected" on drift side (after multiplication processes) for a mean number $n_{initial}$ of e^- resulting from ionization processes associated to an incident X-ray of energy E. Only a fraction of the charge is "seen" for ions going toward cathode, but the definition of the gain concerns detection, so "collected" $\equiv$ "seen", i.e. $n_{final} \equiv$ number of ions "seen" by the detection plane. A capacitance ($C = 10$ pF) is situated at the test entry of the preamplifier. $n = \frac{CU}{e}$ charges are thus "injected" inside of the capacitance by the signal. The integral of the signal after preamplification, i.e. the amplitude of the signal after "shaping", see figure 3.11, generated by these n charges is the same that the amplitude value of the signal after "shaping" generated by n_{final} ions. This is true only if the time taken to collect the charge is shorter than the time of shaping of the preamplifier (the shaping corresponds to an integration and also to a differentiation of the signal, which is useful to separate events close in time and doing "pile-up"; the time of charge collection is shorter for high than for low capacitance detectors, the latter "saturating" more quickly than high capacitance detectors; however the high capacitance detectors are more sensitive to the electromagnetic noise than the low capacitance detectors), which has been "admitted" for the estimation of the gain. Thus, if we find (by linear regression) the value of the amplitude U of a "pulsed" square signal generating a peak at the same position than an incident X-ray peak of energy E, we have $n = n_{final}$, and $n_{initial} = \frac{E}{w}$, where w is the energy of ionization in the gas ($w_{ArCH_4} = 26.2$ eV and $w_{CF_4} = 54$ eV), i.e. the energy lost by a ionizing particle to "obtain" 1 electron in a track. $Gain \equiv \frac{n_{final}}{n_{initial}} \Rightarrow$

$$Gain = \frac{Cw}{eE}U \tag{3.3}$$

To estimate the current on the drift side surface of the detection plane, a nano Amperemeter (scales from 100 pA to 10 nA), is used, see figure 3.11. The current is then read on an oscilloscope, with a slow base time (for example 2 s) to obtain an estimation of the mean value of the current. To get an "acceptable" stability of the current, I have used an empirical method (otherwise a diminution of the current value in time is observed; this diminution is maybe due to charging effects or "leakage currents", in relation with the capacitance of the detection planes or of the nano Amperemeter). The potential value on the detection plane is increased until "V_{max}", which corresponds to the limit value for the apparition of discharges. The latter are "signed" by the saturation of the current. The potential is then decreased until "V_{min}", i.e. the minimal potential where a clear source signal (and thus a clear X-ray incident peak) can be observed. The detection planes is left with the same potential settings during 30 min, without doing any measurements. The potential is then increased by steps and measurements are done at each step, waiting 5 min for the stabilization of the current. As the current is "low" (the intensity of ionization is lower than in high energy physics conditions), the measurement of the gain and the measurement of the current don't have the same "meaning", see below.

The measurement of the gain is done by estimating the mean number of ions that have to be "collected" on drift side to give amplitudes situated "around" the incident position of the X-ray peak. This mean number is "correlated" with events generated by the source and corresponds to the number of charges "seen" after the amplification processes (avalanches). The gain measured in this way is thus an "effective" gain. The presence of "parallel" currents, i.e. coming from processes not "directly" correlated with amplification processes, like surface currents or "microdischarges", modifies the number of ions "collected", and thus the amplitude of the signal observed (which can then be remote of the position of the peak). These parallel currents may thus contribute to a "loss" of the resolution (corresponding to $R_{parallel\ currents}$ term, see section 3.4.1) and also to the "limitation" of the working region (insufficient resolution, discharges occurring earlier, etc.). The current measured with the nano Amperemeter corresponds to the sum of the "source" currents, i.e. in relation with avalanches, and of the "parallel" currents. The parallel currents are probably negligible in the intense ionization conditions of high energy physics, and the measurements of the current can then be used to determine the "effective" gain. However, in the tests conditions presented here or in ν experiments, their contribution should be more important. The comparison between the measurements of the gain and the measurements of the current should then "inform" about the presence of parallel currents (a difference between the results obtained from these 2 "ways" should correspond to the presence of parallel currents).
I_{source} ≡ source current and ν ≡ events frequency (1 "cascade" ≡ 1 "event") in Bq ⇒

$$I_{source} = Gain \cdot n_{initial} \cdot e \cdot \nu \tag{3.4}$$

ν corresponds to the source frequency only if all events are contained in the drift volume. In the "opposite" case, i.e. when the attenuation length of the ionizing particles coming from the radioactive source is much larger than the drift dimensions, ν is proportional to the density of the gas (source frequency is "constant"), thus to the pressure for a constant temperature. The measurements of the current were done in the mini TPC, using the ^{55}Fe source emitting X-rays of 5.90 keV. The attenuation length of the X-rays in the gas can vary from a few mm to a few cm. It depends on the pressure and on the type of gas ($ArCH_4$ or CF_4). Moreover the source, which emits in all direction, was situated near the cathode during the measurements, so an important fraction, much dependant of the pressure, of the X-rays belonging to the half-sphere oriented detection plane → cathode, can be non contained. The frequency of the contained events could be measured, taking into account of the dead time (or could be estimated from Monte-Carlo simulations) but this remains to be done. Precise measurements of the ^{55}Fe activity (data are missing) should also be done. Simulations should be realized to estimate which fraction of the charge "seen" by the detection plane is "seen" by the preamplifier (in relation with the shaping constant and the time taken to collect the charge, so this fraction could depend on the density of the gas and on the potential settings), and which fraction of the charge "seen" by the detection plane contributes to the mean value of the current (without parallel currents). Work is thus still required to measure the parallel currents.

3.5 Results

Some results concerning the working conditions and the measurements obtained on the GEM, the LEM, the Micromegas with grid and with cloth are presented in this section. Measurements concerning the gain, the current and the resolution at different pressures, in $ArCH_4$ and in CF_4, were done only for the LEM and the Micromegas with cloth. Some "answers" concerning their adaptation for ν detection are given in section 3.6.

3.5.1 GEM, some results

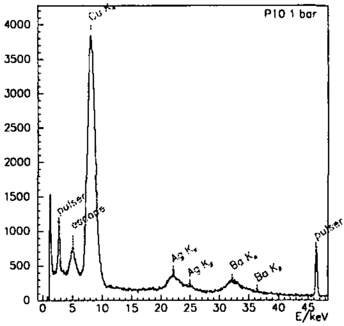

Figure 3.17: Gem tested in the plastic box, in 1 bar of $ArCH_4$ (90 % Ar, 10 % CH_4), for a drift field of 130 Vcm^{-1}bar^{-1}.

In $ArCH_4$, the tests on the GEM have been realized only for a pressure of 1 bar. The spectra of figure 3.17 corresponds to tests realized in the plastic box. Ag and Ba fluorescence X-rays of the switchable source, see section 3.3.3, have been used for the measurements. We can see Ag K_α (22.10 keV) and Ag K_β (24.99 keV), which shows that the resolution is "good", and Ba K_α (32.06 keV). The position of Ba K_β (36.55 keV) is indicated on the figure. Fluorescence X-ray Cu K_α (8.05 keV) (resulting probably from the irradiation of the Cu of the cathode and of the GEM on drift side by 59.5 keV γ of ^{241}Am constituting the "hearth" of the switchable source) is very intense. We see also the escape "Cu K_α - Ar" (the energy of Ar K_α is "missing" to the energy of Cu K_α). The resolution measured on Cu K_α is of about 15 %. From formula 2.20 (and utilizing values given in section 3.3.3 and 3.4.2), we find F $\cong$ 1.2. "Of course" F is in reality smaller than 1, and this result shows that there are "contributions" (like a not perfect configuration of the drift field) to the value of the resolution associated to the statistical fluctuation of the initial number of e^- resulting from ionization processes, but these contributions are not very important. We can also see 2 "pulsers", (on right and on left), showing that the the electromagnetical "contribution" to the resolution is almost negligible. The electromagnetic background, on left, is cut.

Figure 3.18: Recombination of e^- and ions corresponding to tracks crossing the "lenses" near to the detection surface.

We have thus obtained a good resolution with a low drift field. However, measurements done at CERN have shown that drift fields of "a few" kVcm^{-1} were necessary to obtain a good resolution, which is much higher than the drift field of about 100 Vcm^{-1} chosen for the tests in the plastic box (and in the mini TPC, in which almost identical results were obtained). There is a "probable" explanation (simulations would be necessary to confirm it). The distance between the cathode and the GEM is of 3 mm for the measurements done at CERN, while it is of 2.5 cm for plastic box (and of 20 cm for mini TPC). On the figure 3.18, (on which an e^- track has been "added") we see the electric field configuration for a groove [45, 46] (corresponding to a type of GEM on a solid support, whose longitudinal "grooves" distant of 200 μm, and also obtained by etching, "replace" the holes of the GEM; the figure 3.18 has been realized with 2D Garfield, which is adapted to such "longitudinal" configurations), which is "similar" to the electric field configuration of the GEM. The equipotential surfaces (perpendicular to the electric fields lines) act as lenses focusing the drifting e^- and "unfocusing" the drifting ions (these e^- and ions can be considered as drifting space charges; e^- and ions are not "following" perfectly the drift lines because of the scattering and of the repulsive or attractive charge effects). The difference of potential between the 2 surfaces of the groove is of 500 V, while the drift field is of 3 kVcm^{-1}. It would be of course better to do a simulation on a GEM, with a drift field of 100 Vcm^{-1}, and with also a difference of potential of 500 V between the 2 GEM's surfaces (corresponding to the potential settings of the GEM, see below). It is however possible to "imagine" that, in this last case, the drift lines must be more "confined" in the center of the hole, and the drift lines connecting the 2 surfaces must "rise" much higher (because the influence of the detection plane on the drift field must be much stronger for a low drift field). On the figure 3.18 we see what can then happen. When a track is going through one or more "lenses" (thus thus along the electric field lines connecting the 2 faces in 2 "points"), e^-, resulting from the ionization of the gas, and coming from the external part of the surface of a lens, can "meet" the ions (and thus recombine) coming from the internal part of the lens (from another part of the track or from avalanches). It is less probable in 3D than in this 2D representation, but these "meetings" must be "strengthened" by the attraction between the e^- of the track and the "space charge" of the ions created in the avalanche. The energy resolution (and also the spatial resolution, because the track appearance must be "destroyed" by the "lenses") is then "reduced" (its value is increased). It is not the case if the events are far enough from the surface of the GEM. It is thus "understandable" than, with a larger drift zone, the resolution is better than in CERN measurements, for a low drift field. If we compare the results of CERN and plastic box, it doesn't seem that the distance from which observation is "disrupted" must be larger than a few mm, which shouldn't be a problem for a large TPC. It is even possible to imagine, but this has of course to be demonstrated, that this "disruption" could act as a "signature" for events corresponding to the activity of the detection plane. Tests of GEMs in the plastic box (see figure 3.13) in $ArCH_4$ at 1 bar have shown that the gain was increasing exponentially (of about a factor 2 all 25 V steps) and was going from about 100 to 1000 when the potential on GEM drift surface was going from -400 V to -500 V (potential on the other GEM surface was set to 0 V and to about 1000 V on the anode, to have a good e^- evacuation, which is necessary to avoid discharges). It was not possible to go further than -500 V, because of the apparition of discharges. Tests have shown that discharges are very dangerous for GEMs (GEMs were "often" "burned" and definitely "short-circuited" by discharges; the "burnings" have always occurred "around" the holes and were in general clearly "visible"). In the mini TPC filled with 1 bar of CF_4 it was not possible to observe signals corresponding to events of the source. GEMs seemed "opaque", and then they were suddenly burned by the "first" discharge, around -600 V. These discharges occur below the expected "corona value" (20 kVmm^{-1} for Kapton, i.e. polyimide film, corresponding to a difference of potential of about 1000 V between 2 GEMs surface for the 50 μm of Kapton). Burnings have also occurred around the holes in CF_4, i.e. not directly "through" material. There are different "possible" explanations concerning the non functioning of the GEMs in CF_4. It is "possible" that, due to the field configuration around the surface of the GEM, the low diffusion in CF_4 and the importance of attachment coefficient in this gas, the drifting e^- are "staying" too much time in the attenuation zone (i.e. with an energy corresponding to a high attachment probability), and that all e^- are then attached. This should correspond to a "null" gain (i.e close to 1) when computing the latter from the integration of the Townsend coefficient and of the attachment coefficient along the drift path, see section 2.3.1. 3D simulations of the GEM in CF_4 (for example with Maxwell) are necessary to verify if this explanation is correct. We could also think that the GEM could "theoretically" work in CF_4, but with "higher" (i.e. more negative) potential values on the drift side surface, and that the discharges occur "too early". These discharges could be due irregularities around Cu holes or to "parallel" currents on the dielectric material (Kapton), resulting from "impurities" on the latter. These discharges could also be "Pashen discharges", see figure 3.19, coming from "parallel" currents inside of the gas near to the surface of Kapton. The probability of the presence of parallel currents at a "low" difference of potential between the 2 GEM's Cu surface is strengthened by the modification of the composition of the gas, like an increasing of H_2O and O_2 due to the "out-gassing" of the dielectric material. The Kapton is "well-known" for "out-gassing". Further tests have thus to be realized after having "out-gassed" the Kapton (by heating it, which is possible, because the GEM should resist to temperature higher than 100 $°C$, in vacuum conditions).

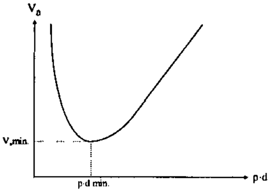

Figure 3.19: A difference of potential is applied between 2 surfaces (i.e. anode and cathode), separated by a distance d. A gas at a pressure p is present between these 2 surfaces. We can measure a current on the latter, resulting from different processes, like "initial" ionizations (due for example to X-rays or μ), avalanches or ionizations, related to the quenching value, of the gas by the UV emitted during the avalanches or the initial ionization processes. At "high" potential value there are additional currents corresponding to the liberation of e$^-$ at the cathode by the drifting ions (by heating of the surface and UV emission processes). These e$^-$ will, "in their turn", participate to avalanches processes. When the difference of potential is increased to V_a, a situation "out of equilibrium" is reached, corresponding to the apparition of "discharges". It is difficult to do the exact computation for a given gas of the current (in function of the difference of potential between the anode and the cathode) and V_a (both depending on product $p \cdot d$). Different parameters have to be taken into account, like the probability of e^- emission at the cathode for 1 drifting ion. These processes are much dependant of the type of gas and also of the concentration of elements such as O_2 and H_2O, and currents or discharges near to the "out-gassing" dielectric surface can then be described by the law of Pashen. This figure represents the appearance of a "possible" V_a curve in function of $p \cdot d$. The "region" situated above the curve is thus not accessible. If the non functioning of the GEM is only due to "Pashen effects", we can imagine that the GEM, which is not functioning at a pressure $p = 1$ bar of CF_4 ($d = 50$ μm) could work at a lower or at a higher pressure.

The non functioning of the GEM in CF_4 can also be caused "simultaneously" by discharges occurring "too early" in reason of "parallel currents" and by an amplification occurring "too late" in reason of the field configuration around the detection plane, which is maybe not adapted to the attachment coefficient properties of CF_4. Tests with lower CF_4 pressures remain to be done (and with pressures different of 1 bar for $ArCH_4$). Tests on the LEM, see section 3.5.2, have shown that the latter seems to function at pressure lower than 1 bar in CF_4 (however the LEM is functioning better in $ArCH_4$ than in CF_4). These tests "seem" to show, in both gas, the presence of "parallel" currents, which could cause discharges occurring "too early" in CF_4, i.e. before the amplification. "Phenomenological laws" are different at different scales and the LEM and the GEM present also some differences in their material configuration (the holes are "conical" in the GEM and "cylindrical" in the LEM, and the dielectric materials are different), so the functioning of the GEM and of the LEM should not be identical.

3.5.2 LEM results

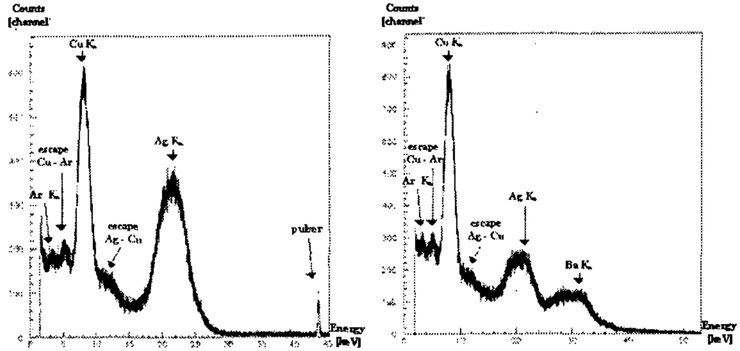

Figure 3.20: LEM tested in the plastic box, in 1 bar of $ArCH_4$, for a drift field of 100 Vcm^{-1}bar^{-1}, with a pulser peak, on left and a Ba peak, on right

The figure 3.20 corresponds to spectra obtained with the LEM in the plastic box, i.e. in 1 bar of $ArCH_4$. We can observe (see section 3.3.3), $Ag\ K_\alpha$, $Cu\ K_\alpha$ resulting probably from the irradiation of the cathode and of the LEM's drift side surface by γ of ^{241}Am, a little "peak" whose energy corresponds to the escape of $Ag\ K_\alpha$ in Cu (energy of $Cu\ K_\alpha$ "missing" to energy of $Ag\ K_\alpha$), the escape CuK_α - Ar, and also a little peak at about 3 keV, which should correspond to $Ar\ K_\alpha$ (2.96 keV) fluorescence peak, resulting from the irradiation of the Ar contained in the gas by γ of ^{241}Am. This peak has not been observed with other detectors (a pulser at this energy on figure 3.17 is maybe hiding this peak for GEM spectra). On right, the source was switched from Ag to Ba during the acquisition, so we see also $Ba\ K_\alpha$. A pulser is present on left, showing that $R_{electromagnetical,\,out}$, see section 3.4.1, is negligible. The resolution measured in the plastic box is equal to 25 % at 8.05 keV (the resolution "contribution" associated to statistical fluctuations is equal to 13 % for F = 1). This resolution is a little better than the resolution measured at 1 bar of $ArCH_4$ in the mini TPC, which can be explained by a better field configuration in the plastic box than in the mini TPC, see remarks concerning figure 3.23. The maximal gain reached in the plastic box was of about 15000, with some discharges, and less than 2000 in the mini TPC, but without discharges, see figure 3.23). Anode doesn't seem useful for the LEM, probably in reason of a sufficient e$^-$ evacuation in the "grounded" LEM surface opposite to the drift side. The working potential (without discharges) on the drift side of the LEM in 1 bar of $ArCH_4$ was comprised between V_{min} = -1600 V and V_{max} = -1900 V, i.e. "only" about 4 times the working difference of potential of the GEM, see section 3.1.1. Discharges are not destructive for the LEM, but all discharges occurring in CF_4 at pressures higher than about 0.5 bar were destructive for the preamplifiers before using the "protected" preamplifier ORTEC 142IH.

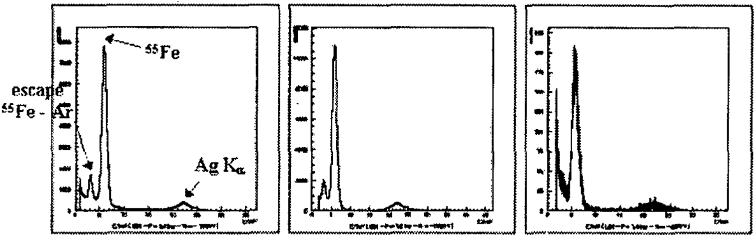

Figure 3.21: LEM tested in the mini TPC filled with $ArCH_4$ with pressures of 0.5 bar (left), 1.0 bar (middle) and 1.4 bar (right). On the 3 spectra of this figure we can see Ag K_α and X-ray incident ^{55}Fe, with a "good" resolution. It is not possible to observe escape ^{55}Fe incident X-ray - Ar at 1.4 bar, because the discharge threshold corresponds to a too low gain (peak below background), see figure 3.23. The escape peak can be obtained at lower pressures (present on the spectra of left and of the middle).

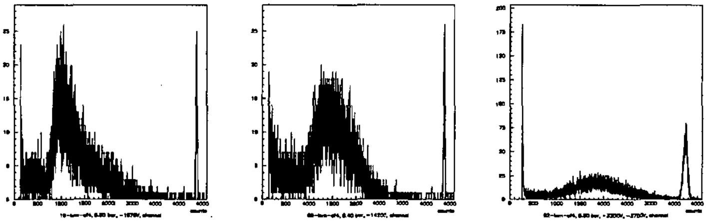

Figure 3.22: LEM tested in the mini TPC filled with CF_4 at pressures of 0.2 bar (left), 0.4 bar (middle) and 0.8 bar (right). On the 3 spectra of this figure we can see ^{55}Fe incident X-ray and a pulser. There is no Ag K_α because the switchable source was not present during these tests and there is also no escape peaks because the tests are done in CF_4, so the proportionality hasn't been "checked" in this gas. The gain is high, see figure 3.23, but the resolution is very poor (and the peaks are "misshapen"). This bad resolution is explained, at least partially, by the bad electric field configuration during the tests, see the remarks concerning the figure 3.23. A possible strong attenuation during the drift and also parallel currents, like Paschen discharges near the dielectric material present between the 2 Cu surfaces, could also "contribute" in part to the bad resolution. The count rate is very low. This could be explained by the important dead time associated to the long duration of the high amplitude signal corresponding to a high gain, but a tail, associated to "pile-up", should be present on the left side of the peak, and this seems not to be the case because the peak is symmetric when the electric field configuration is "good". This low count rate could also be due to a strong attenuation (all e^- could be "attached" during the drift for many events) or to a an important dead time associated to the parallel currents. Further investigations concerning count-rate are required, see section 3.4.2.

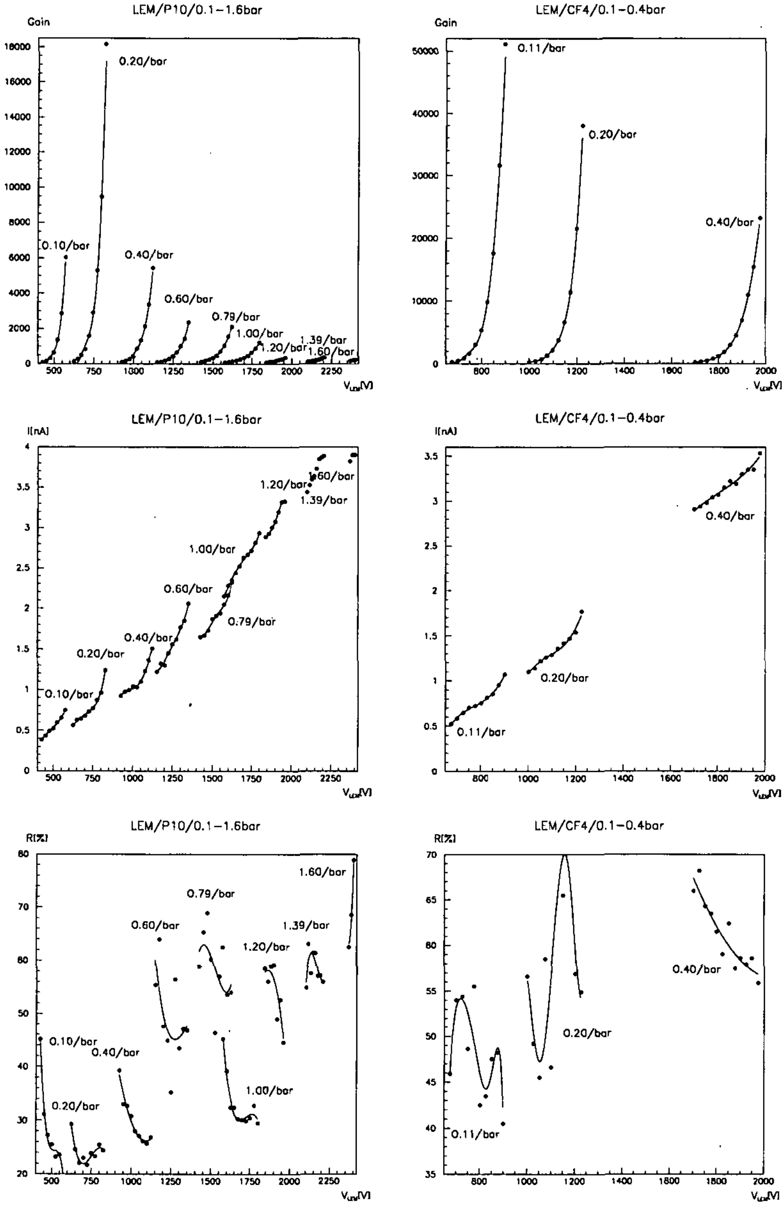

Figure 3.23: Gain, current and resolution measurements in the mini TPC with $ArCH_4$ (left), for pressures comprised between 0.1 and 1.6 bar, and with CF_4 (right), for pressures comprised between 0.1 and 0.4 bar, in function of the difference of potential between the 2 surfaces of a LEM, with a drift field of about 100 $\mathrm{Vcm^{-1}bar^{-1}}$.

The figure 3.23 corresponds to measurements of the gain, of the current and of the resolution, at pressures comprised between 0.1 to 1.6 bar for $ArCH_4$ and between 0.1 to 0.4 bar for CF_4 (the functioning is possible until 1.0 bar, but field configuration is too bad, see below), in function of the difference of potential between the 2 surfaces of the LEM. The potential has not been "reduced" (i.e. potential $\rightarrow \frac{potential}{pressure}$), see section 2.3.1, otherwise the curves would be "superposed".

At each pressure the potential values corresponds to working potential values (comprised between V_{min}, where the energy peak is "clearly" above background, and V_{max}, where the discharges are too frequent for the measurements; determination of the working potential at each pressure $\Leftrightarrow$ determination of the working region). V_{min} corresponds to a gain of about 100 in $ArCH_4$ and of about 250 in CF_4 , independent of the pressure. At "low" pressures there is no discharges at each working potential and the limit of V_{max} is very "clear". At "high" pressures, there are some discharges at each working potential, but their frequency is increasing when potential value "is reaching" V_{max}. Discharges frequency, and thus V_{max}, depends strongly on the cleanliness of the gas and on the characteristic of the surface of the LEM (like dust presence), so V_{max} can vary for "different" measurements done with the "same" conditions.

As V_{min} value corresponds to about the same value of gain at each pressure (gain $\sim$ 100 in $ArCH_4$ and gain $\sim$ 250 in CF_4), it can be used to look at the increasing of the current in function of the pressure for a "given" gain (it would also be possible to look at the increasing of the current in function of the pressure for another given value of the gain). The value of the current at V_{min} is increasing with the pressure. In $ArCH_4$ the increasing of the current at V_{min} is "smaller" than the increasing of the pressure (i.e. the values of the fraction of different currents at V_{min} at different pressures are "smaller" than the value of the fractions of the corresponding pressures), thus it is not possible to "conclude" about the existence of parallel currents, see section 3.4.2. In CF_4 however the increasing of the current at V_{min} is slightly higher than the increasing of the pressure, which seems to indicate the presence of parallel currents. The determination of the count rate (for example with simulations) at each pressure is however necessary to normalize the current. The increasing of the normalized current in function of the pressure for a given gain should correspond to the presence of parallel currents. The presence of parallel currents, like Pashen currents near to the surface of the dielectric, could explain the limitation of the gain (high discharges frequencies at low values of the gain) at "high" pressures (in condition that working region is situated "on the left" of the Pashen curve, see figure 3.19).

A bad field configuration associated to a spatial variation of the local gain (sections 2.3.2, 2.3.3), and to the observed asymmetry of the peak, explains the miss of coherence of the results concerning the resolution. The potential on the field shaping ring 1 is settled by a potentiometer (sections 3.2.4, 3.3.1) of resistance R_{tot} ($\frac{R_{field\ shaping\ rings}}{R_{tot}} = \frac{\Delta V_{cathode \rightarrow ring\ 1}}{\Delta V_{ring\ 1 \rightarrow ground}}$) on which ring 1 potential can be read. Ring 1 potential value read corresponds to ring 1 potential value only for a limited "region" of potential. R_{tot} has been calculated for a region situated around -1700 V on LEM drift side surface (for a drift field of 100 $Vcm^{-1}bar^{-1}$). An additional potentiometer is required for further measurements.

3.5.3 Micromegas with grid, results

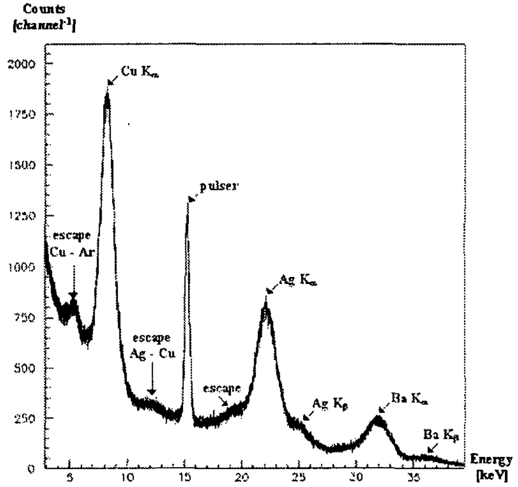

Figure 3.24: Micromegas with a grid distant of 50 μm from anode tested in the plastic box, in 1 bar of $ArCH_4$, for a drift field of about 100 Vcm^{-1}bar^{-1}

The figure 3.24 corresponds to a spectra obtained for a Micromegas with grid distant of 50 μm from anode in the plastic box, i.e. in 1 bar of $ArCH_4$ (the results concerning the gain, the current and the resolution, measured inside of the mini TPC, were however obtained with a Micromegas whose grid was distant of 100 μm from anode). We can observe (see section 3.3.3), from right to left, $Ba\ K_\beta$("not present" on the spectra obtained for the GEM and the LEM), $Ba\ K_\alpha$, $Ag\ K_\beta$, $Ag\ K_\alpha$, escape $Ag\ K_\alpha$ - Ar (energy of Ar K_α"missing" to energy of $Ag\ K_\alpha$), pulser, escape $Ag\ K_\alpha$- Cu (energy of $Cu\ K_\alpha$, resulting probably from the irradiation of the cathode by γ of ^{241}Am, "missing" to energy of $Ag\ K_\alpha$), $Cu\ K_\alpha$, escape CuK_α- Ar (energy of $Ar\ K_\alpha$"missing" to energy of $Ag\ K_\alpha$). The resolution measured in the plastic box is equal to 28 % at 8.05 keV (the resolution "contribution" associated to the statistical fluctuations is equal to 13 % for F = 1) and to 9 % at 22.10 keV (the resolution "contribution" associated to the statistical fluctuations is also equal to 9 % for F = 1; F is smaller than 1 in gas, but the resolution obtained is not far from the theoretical resolution). The resolution obtained there is thus "very interesting". Discharges are "in general" not destructive for the Micromegas, so the latter seems much more reliable than the GEM (but less than the LEM, which seems "indestructible"). In the case of "destructive" discharges, corresponding to a "material" electrical connection between the anode and the grid resulting from burning, it is possible to "recuperate" the Micromegas by putting a teflon tape between the anode and the grid at the location of the burn (it seems not possible, or very difficult, to "recuperate" burned GEMs).

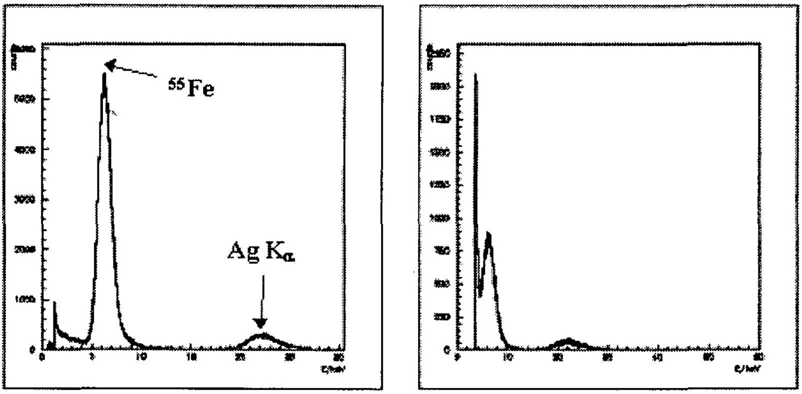

Figure 3.25: Micromegas with grid distant of 100 μm from anode tested in the mini TPC, in 1.0 bar (left) and 2.0 bar (right) of CF_4, for a drift field of 100 Vcm^{-1}bar^{-1}. In both figures we can observe ^{55}Fe incident X-ray (5.90 keV) and Ag K_{α}(22.10 keV). Micromegas with grid is thus "functioning" at 2.0 bar of CF_4, which was one of the criteria "required" for the detection of ν. The working "zone" of potential is less extended at 2.0 bar than at 1.0 bar, see figure 3.27, but the Micromegas is working without discharges, and with a "good" resolution.

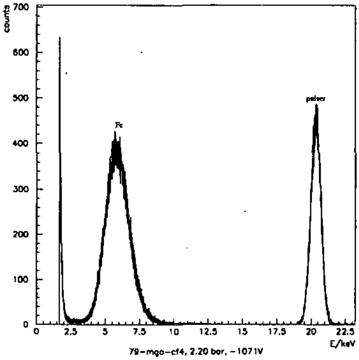

Figure 3.26: Micromegas with grid distant of 100 μm from anode tested in the mini TPC filled with 2.2 bar of CF_4. We can see a pulser on right and ^{55}Fe incident X-ray on left. The resolution (at 5.90 keV) is of about 35 %, see figure 3.27. The switchable source was not present during this test.

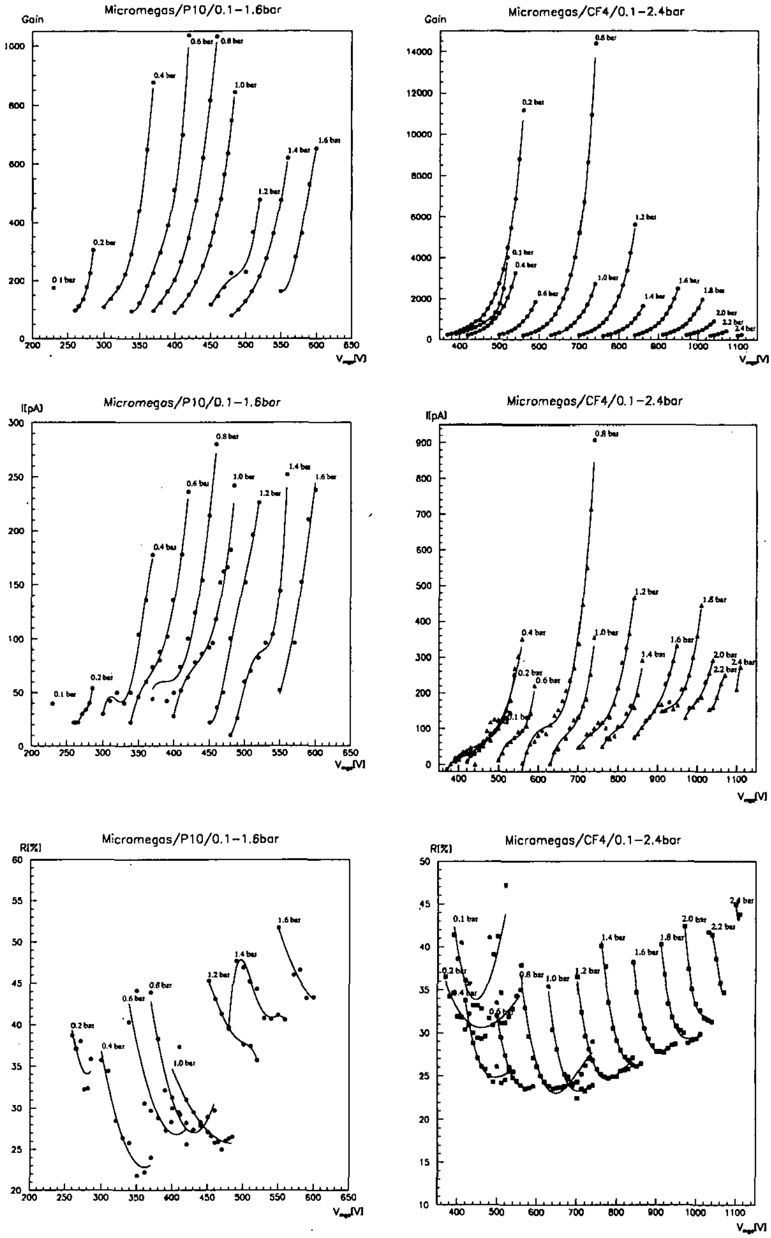

Figure 3.27: Gain, current and resolution measurements in the mini TPC with $ArCH_4$ (left), for pressures comprised between 0.1 and 1.6 bar, and with CF_4 (right), for pressures comprised between 0.1 and 2.4 bar, in function of the difference of potential between the grid and the anode of the Micromegas, with a drift field of about 100 $\mathrm{Vcm^{-1}bar^{-1}}$.

Figure 3.27 corresponds to measurements in the mini TPC of the gain, of the current and of the resolution of a Micromegas with grid whose distance from anode is of 100 μm, at pressures comprised between 0.1 to 1.6 bar for $ArCH_4$ and between 0.1 to 2.4 bar for CF_4 , in function of the difference of potential between the grid and the anode.

The working region can be read from figure 3.27 (as for figure 3.23). The "possible" gain values (without "too much" discharges during the measurement) are higher with CF_4 than with $ArCH_4$ for the same pressures. It would however be possible to do measurements at higher pressures in $ArCH_4$. The frequency of the discharges, and thus V$_{max}$, depends on the cleanliness of the gas and on the characteristics of the surface of the LEM, (like the presence of dusts), so V$_{max}$ can vary for "different" measurements done in the "same" conditions.

As for figure 3.23, V$_{min}$ corresponds to about the same value of gain (gain $\sim$ 100 in $ArCH_4$ and gain $\sim$ 230 in CF_4) at each pressure, thus V$_{min}$ can be used to look at the increasing of the current in function of the pressure for a "given" gain. We don't see an increasing of the current at V$_{min}$ when the pressure is increasing in $ArCH_4$, see left part of figure 3.27, so no parallel currents can be "observed", see section 3.4.2 (but some higher pressures of the working region were not tested). In CF_4 however, the increasing of the current at V$_{min}$ seems higher than the increasing of the pressure (i.e. the values of the fractions of different currents at V$_{min}$ at different pressures are "smaller" than the values of the fractions of the corresponding pressures), which could be due to parallel currents. However, as already mentioned in the remarks concerning the figure 3.23, the determination of the count rate (for example with simulations) at each pressure is necessary to "normalize" the current. The increasing of the normalized current in function of the pressure for a given gain should then correspond to the presence of parallel currents. The presence of parallel currents, like Pashen currents between the thin amplification zone defined by the grid and the anode, could explain the limitation of the gain (high frequencies of discharges at low values of the gain) at "high" pressures in CF_4 (in condition that the working region is situated "on the left" of the Pashen curve, see figure 3.19). The better functioning of the Micromegas than of the LEM in CF_4 could be due to the smaller currents, at a given gain, for the Micromegas with grid (current scale corresponds to pA) than for the LEM (current scale corresponds to nA, see figure 3.23). The difference of the value of the current at a given value of the gain between both detectors could be explained by the larger detection surfaces (which could correspond to a "larger" charge collection) of the LEM than of the Micromegas and by possible Pashen currents between the LEM's detection surfaces related to the presence of the dielectric.

The results concerning the resolution (measured at 5.90 keV) are more "coherent" for the measurements in CF_4 than for the measurements in $ArCH_4$, which could be explained in part by the presence of the escape (incident ^{55}Fe - Ar, at 2.94 keV) "near" to ^{55}Fe incident X-ray (5.90 keV) for $ArCH_4$, and by the lower value of the gain (at identical pressures) for $ArCH_4$ than for CF_4. The variation of the results about the resolution in function of the pressure could have various origins such as the configuration of the drift field, see remarks concerning figure 3.23, the attachment properties or the presence of parallel currents. Further investigations are thus required.

3.5.4 Micromegas with cloth, preliminary results

The cloth is described in the section 3.1.2. It is sturdy and can be obtained in very large dimensions, so it could eventually replace the grid of a Micromegas for a large TPC. The Micromegas with cloth seems maybe more resistant to discharges than the Micromegas with grid. Its electrostatic stretching properties, see section 3.1.2, seem identical to that of a grid (a "perfect" equidistance between the grid and the anode can be obtained by electrostatic stretching and corresponds to an homogeneous gain, and thus to a good resolution). However the cloth is made of a larger quantity of material than the grid ($\emptyset = 3$ μm for grid and $\emptyset = 20$ μm for cloth), which is a disadvantage concerning the radioactivity, even if the quantity of material is still "low" (if we compare for example the latter with the cathode). Only preliminary tests were done (many tests remain to be done) with a Micromegas whose grid was replaced by a cloth, but the functioning of a Micromegas with cloth seems almost identical to that of a Micromegas with grid.

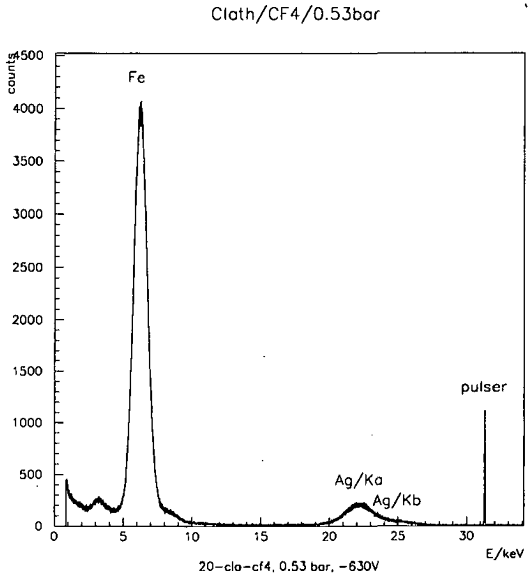

Figure 3.28: Micromegas with cloth tested in the mini TPC filled with 0.5 bar of CF_4, for a drift field of about 100 Vcm^{-1}bar^{-1}. The distance between cloth and anode is of 100 μm. We see a pulser, Ag K_α (22.10 keV) and ^{55}Fe incident X-ray (5.90 keV). The small peak on left is not explained. Ag K_β position (24.99 keV) is indicated. The resolution is of about 20 % at 5.90 keV.

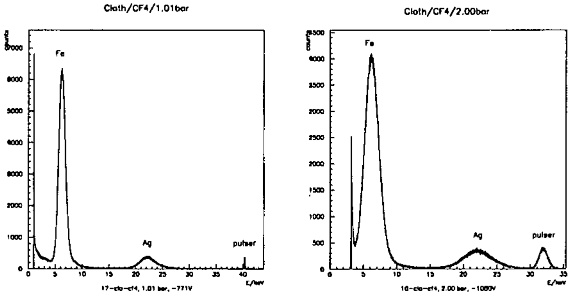

Figure 3.29: Micromegas with cloth tested in mini TPC filled with 1.0 bar (left) and 2.0 bar (right) of CF_4, for a drift field of about 100 Vcm^{-1}bar^{-1}. We can see a pulser, Ag K_α and ^{55}Fe incident X-ray. The spectra seems almost identical to that of figure 3.25, obtained in the same conditions. The Micromegas with cloth is thus also "functioning" in 2 bar of CF_4. The working potentials of the cloth (anode is grounded; the potentials of the cloth are indicated on this figure and also on figure 3.28) correspond almost (identical at "high" pressure and a little "higher" for the cloth than for the grid at "low" pressure) to the working potentials of the grid at the same pressures, see figure 3.27.

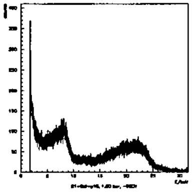

Figure 3.30: 2 clothes (1 cloth "replaces" the anode), with $\emptyset = 9$ cm, "mechanically" stretched and separated by a mylar ring of 150 μm, are tested in the plastic box filled with $ArCH_4$ at 1 bar. As cloth is "transparent", such a configuration could be used to see the UV coming from the avalanches, for example with optical fibers coupled to diodes or with a camera. We see Ba K_α on right and Ag K_α on left. The resolution is poor, but this is probably due to the "mechanical" stretching (clothes were stretched mechanically because of the absence of "spacers"; the "equidistance" can't be obtained with a "mechanical" stretching). A cloth with engraved spacers is thus necessary for a configuration with 2 cloths. Rui de Oliveira is now realizing such an engraving, on a cloth I gave to him, with a ring realized in the same material than the spacers, so no more gluing neither stretching are necessary. He thinks that the working of such a cloth (1 cloth with spacers and ring both realized by photolithography and 1 anode) would be very promising, because it would help solving a lot of problems relative to the fragility of the Micromegas grids (like handling, stretching, resistance to discharges or cleaning).

3.6 Conclusion

The principal objective of the "investigations" was to find detection planes adapted for the detection of ν in a "large" TPC, and thus to "answer" to the "questions" corresponding to the qualities required for these detection planes. Some important qualities required, see section 3.1, and "answers" obtained during the tests are the following:

- they must be "large" (detection planes until about 3 m of diameter)

GEM	LEM	Micromegas with grid	Micromegas with cloth
~	+	~	+

mechanical realization more favorable that etching realization to obtain large detection planes; grids of large dimensions already exist

- they must present a low radioactivity ("little" quantity of "low" activity materials)

GEM	LEM	Micromegas with grid	Micromegas with cloth
-	-	+	~

presence of dielectric "not favorable" for low activity; activity still not tested

- they should operate in CF_4 or in other gases aimed for ν detection

GEM	LEM	Micromegas with grid	Micromegas with cloth
-	-	+	+

presence of dielectric seems not favorable for functioning in CF_4

- they must operate with a "low" drift field

GEM	LEM	Micromegas with grid	Micromegas with cloth
+	+	+	+

cathode at a "few" mm of detection plane ⇒ homogeneous drift field

- they have to be "reliable" (for example resistant to discharges)

GEM	LEM	Micromegas with grid	Micromegas with cloth
~	+	+	+

GEM seem "too sensible" to discharges to be used in large TPCs

We see that the LEM and the GEM seem clearly not adapted for ν detection. "Pavements" must be realized for the grid while the cloth activity must certainly be reduced. Wires could present "positive" answers to all "questions" (for example working with 3 bar of CF_4 in MUNU), so configuration such as wire planes weaved on a star support must be considered.

Conclusions

Experiments about the properties of the ν (like the mass or the magnetic moment) such as low energy ν experiments (like reactor experiments, future solar experiments concerning the unexplored low energy part of the solar spectra or $0\nu\beta\beta$ decay observation), are fundamental in a lot of areas in physics, such as superstrings or astrophysics. The principal subject of this work was concerning the detection of low energy ν with a TPC. The experiments on low energy ν with a TPC are difficult to realize, principally in reason of the high efficiency required to avoid the background or to reject the latter. However the TPCs present also "unique" tracking features, which make for example possible to "identify" various events through their topology, to localize the sources of background or to do reconstructive spectroscopy. I think that MUNU experiment on $\bar{\nu}_e e^-$ scattering, and also Gotthard [22, 23, 24, 25] experiment on 0ν and 2ν $\beta\beta$ decay, have shown the difficulties that can be encountered in low energy ν detection with a TPC, but also the strong resources offered by TPCs, in particular when both electronic and light signals are exploited. MUNU is still running and new results concerning μ_ν are expected, which we hope will be more interesting than the previous ones. Projects concerning the utilization of a TPC for future experiments on the properties of ν exist already, such as the detection of solar ν down to pp energies [26] in a TPC filled with He at high pressure [47, 48], or the detection of very small ν masses in $\beta\beta$ decay using laser tagging in a TPC filled with ^{136}Xe [27, 28]. The chapter 3 was concerning more specifically future projects on ν detection using CF_4 (like superMUNU), which, in reason of its high e^- density, could be used at lower pressure than He. But the high size increasing (in relation with MUNU size) needed implies still stronger constraints concerning the background and, even considering the "experience" acquired during MUNU experiment, a "simple" size increasing of MUNU experiment is not sufficient to perform solar ν spectroscopy. A still more performing TPC (concerning for example its angular resolution and the activity of the material used to build the latter) is required. A "sure" identification of the events coming from the detection plane, but also from the cathode, must be found. It would be still more useful to find a way to determine, for each events, the "time of occurrence" (for example with a more transparent TPC and a still more efficient light detection system to see the emission of the primary light), and thus the absolute Z coordinates of the track. The high spatial resolution of the Micromegas could also make possible the determination of the absolute Z coordinates, by measuring the lateral extension of the track during the drift, which is proportional to the drift distance (Z). We have seen that the Micromegas with grid, or with cloth, could eventually be used to realize larger detection planes adapted for the detection of ν. Other tests and developments have shown that the Micromegas (with grid) could be used (with gas like He, Xe, Ne, Ar, Xe) to realize experiments on the properties of ν or to perform the detection of other particle like solar axions or WIMPS [49]. An experiment on "very low" energy ν (15 keV) using a very intense (about 100 Mci) source of tritium could measure μ_ν down to 10^{-12} μ_B [50]. The wires are also "still" interesting for the detection of ν, but Micromegas are maybe more interesting, in reason for example of their "simplicity", of their high resolution (certainly useful even in case of a large TPC presenting already a loss of resolution due to drift) or of the high gains that can be obtained with the latter. We could also use a Micromegas in a different way, for example by realizing an XY readout using the light for the detection and the acquisition (for example by utilizing single optical fibers coupled to photodiodes to detect the light coming from avalanches at an XY "point" and to transmit the signal), because the light is non sensitive to the electromagnetical noise and is certainly the best way to transmit information.

The LEM (GEM × 10 whose holes are realized mechanically) and the cloth (Micromegas "grid" made of wires weaved in a "crossed" way) "found" during this work could also have other applications than the detection of ν or the eventual replacement of the grid by a cloth in other detectors. LEM could be used to build for example low cost radioactivity detectors with 3D tracking performances and to localize radioactive sources in very difficult conditions. GEM is already used as a photocathode, using a chemical layer which emits an e^- when an X-ray is hiding the latter. Such photocathodes are very efficient and can be used for example to do radiographies with very low "doses" or to perform biological or medical investigations using radioactive isotopes. Micromegas are also used as photocathode, using a CsI layer sensitive to UV [51] (the CsI must cover only the surface on drift side, because UV resulting from avalanches could also eject e^- of CsI; layer deposition must be realized under vacuum conditions and contact with O_2 must be avoid). Investigations are done to realize Micromegas with a layer sensitive to X-rays. We could eventually use the cloth in a similar way (i.e. with a chemical layer on 1 side of the latter). The "high" surface of the cloth ($\emptyset = 20$ μm for the wires of the cloth and $\emptyset = 3$ μm for the strips of the grid) is maybe interesting for such an application. We could also realize a "large" detector (contained in a thin transparent "flat" box filled for example with Xe), made of 2 successive cloths, one of them with spacers (and ring) engraved and the other with a chemical layer sensitive to the X-rays. A digital camera sensible to the UV emitted during the avalanches and situated at the exterior of the "box" could then replace the XY electronic readout sensible to the charges resulting from the amplification. Such a detector could be used for example to realize low cost and low dose radiographies. One could also imagine a detector made entirely of cloths, with 1 cloth constituted of weaved optical fibers for the detection of the scintillation light coming from the avalanches.
Maybe all of this is dream, but it is only by dreaming that one can approach "reality".

Bibliography

[1] coll. GALLEX (P. Anselmann et al.) *Nucl. Phys. B (Proc. Suppl.)* **38**, p. 68, 1995.

[2] coll. SAGE (V.N. et al.) *Nucl. Phys. B (Proc. Suppl.)* **91**, pp. 36–43, 2001.

[3] coll. Super-Kamiokande (Y. Susuki et al.) *Nucl. Phys. B (Proc. Suppl.)* **91**, pp. 29–35, 2001.

[4] coll. SNO (A.B. McDonald et al.) *Nucl. Phys. B (Proc. Suppl.)* **91**, pp. 21–28, 2001.

[5] coll. SNO (Q.R. Ahmad et al.), "Measurement of charged current interactions produced by ^{8}b solar neutrinos at the sudbury neutrino observatory," 2001. to be published.

[6] C. B. et al.), "A gas detector to measure the $\bar{\nu}_e$ magnetic moment at a nuclear reactor," *Nucl. Instr. Meth. A* **311**, pp. 319-326, 1992.

[7] coll. MUNU (C. Amsler et al.), "The munu experiment, general description," *Nucl. Instr. Meth. A* **396**, pp. 115–129, 1997.

[8] coll. MUNU (M. Avenier et al.), "Sub mev particles detection and identification in munu detector," *Nucl. Instr. Meth. A* . to be published.

[9] coll. MUNU (C. Broggini et al.), "Recent results and status of the munu experiment," *Nucl. Phys. B (Proc. Suppl.)* **91**, pp. 105–109, 2001.

[10] C. Cerna, "Munu, étude de la diffusion neutrino électron," *Ph.D. Thesis Grenoble Univ.* , 2000.

[11] P. Vogel and J. Engel *Phys. Rev.* **D39**, p. 3378, 1989.

[12] G. Zacek *Phys. Rev.* **D34**, p. 2621, 1986.

[13] B. Achkar *Phys. Lett. B* **374**, p. 243, 1996.

[14] F. Reines *Phys. Rev. Lett.* **37**, p. 315, 1976.

[15] A. D. et al. *Phys. of Atomic Nuclei* **57**, p. 222, 1994.

[16] R. A. et al. *Phys. Rev. Lett.* **55**, p. 2401, 1985.

[17] R. A. et al. *Phys. Rev.* **D47**, p. 11, 1993.

[18] J. Beacom and P. Vogel 1999.

[19] J. Morgan *Phys. Lett.* **102B**, p. 247, 1981.

[20] R. Barbieri and R. Mohapatra *Phys. Rev. Lett.* **61**, p. 27, 1988.

[21] G. Raffelt *The Astrophysics Journal* **365**, p. 559, 1990.

[22] H. W. et al., "Event identification with a tpc in a double beta decay experiment on ^{136}xe," *Nucl. Instr. Meth. A* **329**, pp. 163–172, 1993.

[23] H. W. et al., "A search for double beta decay in ^{136}xe with a tpc," *Ph.D. Thesis Caltech* , 1991.

[24] J. Farine, "New low background techniques for neutrino experiment at low energy. first results.," *Ph.D. Thesis Neuchâtel, year = 1996* .

[25] R. Luesher, "Double beta decay in ^{136}xe: upgrade of the gotthard experiment, new results and low pressure investigations," *Ph.D. Thesis Neuchâtel* , 1999.

[26] J. Bahcall, "Neutrino astrophysics," *Cambridge University Press* , 1989.

[27] E. Fiorini, "Double beta decay: The future," *Nucl. Phys. B (Proc. Suppl.)* **91**, pp. 262–269, 2001.

[28] M. D. et al., "Detection of very small neutrino masses in double-beta decay using laser tagging," submitted.

[29] W. A. et al., "Electron attachment, effective ionization coefficient, and electron drift velocity for cf_4 gas mixtures," *Nucl. Instr. Meth. A* **323**, pp. 273–279, 1992.

[30] L. C. et al., "Fast gas mixtures for gas-filled particle detectors," *Nucl. Instr. Meth.* **163**, pp. 141–149, 1979.

[31] http://consult.cern.ch/writeups/garfield.

[32] F. Sauli *Nucl. Instr. Meth. A* **386**, p. 531, 1997.

[33] F. Sauli, "Gas detectors: Recent devlopments and future perspectives," *Nucl. Instr. Meth. A* **419**, pp. 189 201, 1998.

[34] A. B. et al., "High and low pressures operation of the gas electron multiplier," *Nucl. Instr. Meth. A* **419**, pp. 418–422, 1998.

[35] R. C. et al., "First results on the gem operated at low gas pressures," *Nucl. Instr. Meth. A* **419**, pp. 423 428, 1998.

[36] R. B. et al., "What is the real gain of a standard gem?," 1998. report, INFN-Pisa and University of Pisa, Italy.

[37] A. B. et al., "Two-dimensional readout of gem detectors," *CERN-EP / 98-164*, 1998.

[38] I. G. et al. *Nucl. Instr. Meth. A* **376**, p. 29, 1996.

[39] I. Giomataris *Nucl. Instr. Meth. A* **419**, pp. 239–250, 1998.

[40] I. Giomataris *Development of fast gaseous detector Micromegas* , 1998. Invited talk presented at the 8^{th} Vienna Wirechamber Conference.

[41] G. C. et al. *Nucl. Instr. Meth. A* **412**, p. 47, 1998.

[42] J. Perroud and F. Ronga 1999. report Lausanne University IPHE.

[43] F. J. et al. *Nucl. Instr. Meth. A* **450**, pp. 314–324, 2000.

[44] J. D. et al., "Experimental studies on the spatial resolution of micromegas detector," 2000. submitted to Elsevier preprint.

[45] R. B. et al., "The micro-groove detector," report.

[46] R. B. et al., "The well detector," report.

[47] E. C. et al., "High pressure solar neutrino tpc," 2001. Letter of Intent.

[48] P. G. et al. *Nucl. Instr. Meth. A* **433**, p. 554, 1999.

[49] J. Collar and I. Giomataris, "Low-background applications of micromegas detector technology," Presented at IMAGING 2000, Stockholm, June 2000.

[50] J. Bouchez and I. Giomataris, "Study of neutrino oscillations and electromagnetic properties using a strong tritium source," 2001. report.

[51] J. D. et al., "Fast signals and single electron detection with a micromegas photodetector," 1999. submitted to Elsevier preprint.